

ABSTRACT

Title of Dissertation: CONTROLLING AND ENHANCING ATMOSPHERIC
 OPTICAL/PLASMA FILAMENTS

Sanjay Ramesh Varma, Doctor of Philosophy, 2011

Dissertation directed by: Professor Howard M. Milchberg
 Institute for Research in Electronics and Applied Physics

As intense laser pulses propagate in atmosphere, they experience dramatic self-focusing, spectral broadening and phase modulation, and they ionize atmospheric molecules. The self-focusing and ionization-induced defocusing are competing effects that keep parts of the beam, called filaments, at high intensity over many Rayleigh lengths. Optical filaments and the plasma filaments that follow them are useful tools for remote sensing and ionization, atmospheric monitoring, terahertz generation, guiding of electrical discharges and optical pulse compression even to the few-cycle regime. Some of these applications may only be realized when the filamentation process is stabilized and plasma density is enhanced.

Our experiments have shown that the rotational response of atmospheric nitrogen and oxygen is large enough and fast enough to dominate Kerr-induced self-focusing for

optical pulses propagating with FWHM time duration > 40 fs. Moreover, our measurements have pointed to a way to greatly enhance the filament electron density by controlling the alignment of ambient N_2 and O_2 molecules and thereby controlling the optical nonlinearity of air. In addition, our group pointed out for the first time that quantum effects could dominate the propagation of intense femtosecond pulses in the atmosphere.

This effect was demonstrated in our experiment that showed the quantum beats from laser-excited rotational wavepackets were able to steer, enhance or destroy laser filaments, depending on laser pulse timing. Our more recent work demonstrates that these quantum effects can increase the length of the plasma filament by a factor of three and can also promote soliton-like behavior of the pulse, cleaning and compressing it temporally. We performed direct measurements of the plasma density left behind by the filamenting optical pulses to confirm enhancement and extension of the electron density and laser intensity. Compression was measured with SPIDER, a technique for measuring the complex envelope and phase of optical pulses with sub-5 fs features.

CONTROLLING AND ENHANCING ATMOSPHERIC OPTICAL/PLASMA
FILAMENTS

by

Sanjay Ramesh Varma

Dissertation submitted to the Faculty of the Graduate School of the
University of Maryland, College Park in partial fulfillment
of the requirements for the degree of
Doctor of Philosophy

2011

Advisory Committee:

Professor Howard M. Milchberg, Chair
Professor Thomas M. Antonsen
Professor Thomas E. Murphy
Professor John C. Rodgers
Professor John T. Fourkas, Dean's Representative

© Copyright by
Sanjay Ramesh Varma
2011

to my family
ramesh, susheela and vijay varma

Acknowledgements

First and foremost, I thank my advisor, Professor Howard Milchberg, for being a great advisor, mentor and colleague over the time I spent in his laboratory. These past years have been a time of profound intellectual and personal growth for me, and I am grateful for the part he played in making that possible. I have been challenged to think and work harder than I ever had before, and I couldn't be happier about the results.

I also must thank the professors, post-docs and graduate and undergraduate students who worked with me at the University of Maryland. I am lucky to have worked with Dr. Andrew York, who is one of my greatest friends. I am indebted to Yu-hsin Chen, who worked tirelessly with me on many of the experiments which appear in this dissertation. I thank Brian Layer for many years of collaborative work and friendship. I appreciate the work of my theorist colleagues Professor Thomas Antonsen and Dr. John Palastro. I thank Dr. Vinod Kumarappan for introducing me to the laboratory when I first arrived. I am amazed and inspired by the new graduate students Arman Fallahkhair and Eric Rosenthal. Working with them has been a lot of fun, and I hope that I have helped them out as much as they have helped me. Also deserving of heartfelt thanks are my terrific friends, colleagues and housemates Dr. Navik Agrawal and Zachary Wilkes.

I am grateful for the support of all of my friends, many who I consider family. Without them, my life would be a darker place. I finally thank my father Ramesh, my mother Susheela, and my brother Vijay for taking care of me, especially during the times that I need them the most.

Table of Contents

Acknowledgements.....	iii
Table of Contents.....	iv
List of Figures.....	vii
Chapter 1: Introduction and overview.....	1
1.1 Introduction to filamentation.....	1
1.2 Self-focusing and plasma generation in a filamenting optical pulse.....	3
1.2.1 Self-focusing.....	3
1.2.2 Ionization and plasma-induced defocusing.....	6
1.2.3 Self-phase modulation and spectral broadening.....	8
1.3 Controlling the stability and length of a filament.....	10
1.3.1 Multiple filamentation.....	10
1.3.2 Experimental attempts to stabilize and lengthen plasma filaments.....	12
1.4 Applications of filamentation.....	13
1.4.1 Remote sensing.....	13
1.4.2 Guiding of high-voltage discharges.....	14
1.4.3 Generation of few-cycle optical pulses.....	15
1.4.4 High-harmonic generation.....	16
1.4.5 Filaments as a source of terahertz radiation.....	16
1.4.6 Optical waveguides made from filament-induced damage in solids.....	17
1.4.7 Filaments as an underwater acoustic source.....	18
1.4.8 Microsurgery using ultrashort laser pulses.....	19
1.5 Chapter synopsis.....	19

Chapter 2: Measuring an ultrashort laser pulse.....	21
2.1 Introduction to ultrashort laser pulses.....	21
2.2 Autocorrelation.....	23
2.2.1 The intensity autocorrelation.....	23
2.2.2 Single-shot autocorrelator.....	26
2.3 FROG – Frequency-resolved optical gating.....	28
2.3.1 Polarization-gated FROG.....	28
2.3.2 GRENOUILLE.....	31
2.4 SPIDER – Spectral phase interferometry for direct electric field reconstruction.....	33
2.4.1 SPIDER algorithm.....	33
2.4.2 SPIDER apparatus.....	35
2.4.3 SPIDER for filamenting optical pulses.....	38
Chapter 3: The rotational response of atmospheric constituents.....	39
3.1 Instantaneous versus rotational response of linear molecules.....	39
3.2 The relationship of molecular alignment to the refractive index.....	41
3.3 Quantum mechanical rigid rotor model of molecular alignment.....	42
3.3.1 Early measurement and modeling of optically-driven molecular alignment.....	42
3.3.2 Measurement of quantum molecular alignment using spectral analysis..	45
3.4 Simulation of quantum molecular alignment of N ₂ and O ₂	46
3.5 Inter-molecular collisions.....	48

3.6 Direct space-and-time resolved measurement of delayed rotational response and quantum molecular alignment revivals.....	49
3.6.1 Measurement of molecular alignment using Coulomb explosion imaging.....	49
3.6.2 Spectral interferometry.....	49
3.6.3 SSSI.....	51
3.6.4 Xenon SSSI.....	52
3.6.5 Measurement of rotational wavepackets of N ₂ O, N ₂ and O ₂	53
3.7 Relevance of rotational response of N ₂ and O ₂ to atmospheric filamentation.	57
Chapter 4: Trapping, enhancement and destruction of an optical/plasma filament in a quantum molecular alignment wake.....	59
4.1 The critical power for self-focusing in air.....	59
4.1.1 Derivation of P_{cr}	59
4.1.2 Experimental measurement of P_{cr}	60
4.2 Filament enhancement experimental concept.....	62
4.3 Experimental setup.....	66
4.4 Results and discussion.....	69
4.4.1 Probe filament enhancement and destruction near $\tau \approx 0$	69
4.4.2 Probe filament trapping, enhancement and destruction near $\tau \approx 8.3$ ps..	72
4.4.3 Measurement of spectral broadening.....	79
4.5 Conclusions and future experiments.....	82
Chapter 5: Coherently excited quantum wake-induced pulse shaping and extension of femtosecond air filaments.....	85

5.1 Introduction.....	85
5.2 Interferometric optical plasma density measurement.....	86
5.3 SPIDER measurement of probe electric field.....	90
5.4 Discussion and analysis.....	99
5.5 Conclusion.....	107
References.....	109

List of Figures

Figure 1.1: Filamentation of ultrashort pulses in gas. P_{cr} is the critical optical power above which the beam will collapse on itself due to self-focusing.	2
Figure 1.2: Filamenting beam images with increasing power (P_{cr} occurs at 1.25 mJ for a 130 fs pulse).	5
Figure 1.3: spectrum of a 120 fs, 19 GW pulse before (solid line) and after (dashed line) it filaments 1 meter in atmosphere.	10
Figure 1.4: Multiply filamenting beam [21].	12
Figure 1.5: Femtosecond-induced breakdown spectrum of egg white [29].	14
Figure 1.6: Top—several meter-long electrical discharge with no filaments present. Bottom—guiding of the discharge by optically generated plasma filaments [32].	15
Figure 1.7: Self-compression of a 45 fs, 800 nm pulse after filamentation in a krypton gas cell. A) is the initial pulse, B) is the pulse before it exits the gas cell, and C) is the pulse after it passes through the gas cell exit window [34].	15
Figure 2.1: Scanning delay Michelson autocorrelator. M1 is a mirror on a scanning delay stage, M2 is a static mirror, BS is a 50/50 beamsplitter, and F is a filter that only passes second harmonic frequency light.	24
Figure 2.2: Single-shot autocorrelator. The delay rail at the top is not scanning; it is set so that both pulses are coincident on the BBO crystal.	26
Figure 2.3: Raw SSA image (left) and retrieved autocorrelation (right).	27
Figure 2.4: Frequency-resolved optical gating setup [55].	28
Figure 2.5: GRENOUILLE schematic [56].	31
Figure 2.6: GRENOUILLE trace (left) and retrieved $I(t)$ (right) for a 70 fs pulse.	32
Figure 2.7: SPIDER apparatus, followed by sample interferogram and retrieved $ E(t) $.	36
Figure 3.1: Calculated molecular alignment versus time for N_2 (top) and O_2 (bottom) gas due to a 100 fs pulse. The dashed line indicates the intensity of the optical excitation.	47

Figure 3.2: SSSI setup used to measure double-step ionization of helium gas [76].	51
Figure 3.3: Xenon SSSI. BS1: beamsplitter, XGC: xenon gas cell, MI: Michelson interferometer, P: 500 μm pinhole, SF4: 2.5-cm thick SF4 glass as dispersive material, HWP: half waveplate, M: zero degree Ti:Sapphire dielectric mirror, BS2: beamsplitter for combining pump and SC pulses.	53
Figure 3.4: Raw SSSI Interferogram showing the initial nonlinear response of N_2O to a 100 fs pulse.	54
Figure 3.5: a) axial alignment of N_2 measured by SSSI, b) SSSI space-resolved alignment, and c) theoretically computed molecular alignment for comparison with a).	55
Figure 3.6: a) axial alignment of O_2 measured by SSSI, b) SSSI space-resolved alignment, and c) theoretically computed molecular alignment for comparison with a).	56
Figure 3.7: Initial response of N_2 gas to a 100 fs pump pulse, as measured by SSSI (circles), intensity envelope of the pump pulse (dots), and calculated molecular alignment (line).	57
Figure 4.1: Experimental measurement of air refractive index change near $t=0$ (black line), synthesized from SSSI measurement of molecular alignment of N_2 and O_2 , compared with the pump pulse $I(t)$ (red dotted line).	61
Figure 4.2: Measured alignment of 1atm N_2 and O_2 at room temperature by a 110 fs, 800 nm, $4.1 \times 10^{13} \text{ W/cm}^2$ laser pulse. The effective alignment of air is synthesized from the N_2 and O_2 plots.	63
Figure 4.3: dual-polarization interferometer (DPI) and probe filament end mode imaging setup.	66
Figure 4.4: 2D WAKE simulation results showing plasma density (solid markers) and radius (hollow markers) of two 65 fs, 6 mJ pulses launched with $f_{\#} \sim 300$ and filamenting in atmosphere. Black-Gaussian transverse profile, blue-flat top profile.	68
Figure 4.5: 1-D slices of the probe filament image v. pump/probe delay near $\tau \approx 0$.	70
Figure 4.6: 1-D slices of the probe filament image v. pump/probe delay near $\tau \approx 0$ for 330 fs pump and probe pulses.	72

Figure 4.7: 1-D slices of the probe filament image v. pump/probe delay near $\tau \approx 8.3$ ps for 130 fs pump and probe pulses which are misaligned by 1mrad. Inset in the graph are the air alignment near the same delay, and 2-D images corresponding to selected delays. The dashed gray line indicates the position of the pump filament.	73
Figure 4.8: 1-D probe filament profiles v. delay for constant probe filament energy and increasing pump filament energy near $\tau \approx 8.3$ ps.	76
Figure 4.9: 1-D slices of the probe filament image v. pump/probe delay near $\tau \approx 8.3$ ps for 130 fs, collinear pump and probe pulses.	78
Figure 4.10: digital camera image of pump and probe filaments incident on an index card at three different delays near 8.3 ps. (i) at non-specific τ , where there is no alignment, (ii) is at $\tau \sim 8.35$ ps, where aligned N_2 steers the probe filament into the pump path, and (iii) is at $\tau \sim 8.5$ ps, where anti-aligned N_2 and O_2 deflect the probe from the pump path.	80
Figure 4.11: Probe filament spectrum as a function of delay (33 fs steps) through the air alignment revival near $\tau = 8.3$ ps.	81
Figure 5.1: Filamenting pulse diagnostic experiment. The plasma density is measured by an optical interferometry setup on a sled (shaded gray region). L indicates a lens and O is a microscope objective. The filamenting probe pulse is selected by an aperture A and TFP before being sent into SPIDER. Residual probe light is separated from the pump using a cube polarizer C and sent into a broadband fiber spectrometer.	86
Figure 5.2(a): Peak on-axis electron density of the plasma filament for pump/probe delays from 8.326 ps to 8.379 ps. Plasma density of pump and probe filaments alone are shown with dashed lines.	87
Figure 5.2(b): Peak on-axis electron density of the plasma filament for pump/probe delays from 8.379 ps to 8.419 ps. Plasma density of pump and probe filaments alone are shown with dashed lines.	88
Figure 5.3(a): Peak on-axis electron density of the plasma filament v. pump/probe delay 54 cm before vacuum focus for a range of probe pulse energies. The pump plasma present in absence of the probe is indicated in red.	89
Figure 5.3(b): Peak on-axis electron density of the plasma filament v. pump/probe delay 9 cm before vacuum focus for a range of probe pulse energies. The pump plasma present in absence of the probe is indicated in red.	90

Figure 5.4: Raw SPIDER interferograms (2D spectra in the right hand column) and corresponding retrieved $I(t)$ (left hand column) for a singly filamenting, 1.6mJ pulse passing through circular apertures of increasing diameter (inset).	91
Figure 5.5: First column: measured $I(t)$ and $\Phi(t)$ for a 2.5 mJ probe pulse for selected pump/probe delays. Second column: corresponding $I(\lambda)$ and $\varphi(\lambda)$, with the pre-filamentation spectrum in dashed red lines. Third column: corresponding Wigner plots, with the pre-filamentation Wigner plot inset at the top right.	92
Figure 5.6(a): Measured $I(t)$ and $\Phi(t)$ for a 2.5 mJ probe pulse finely spaced pump/probe delays within the air revival between 8.306 ps and 8.426 ps.	93
Figure 5.6(b): Measured $I(\lambda)$ and $\varphi(\lambda)$ for a 2.5 mJ probe pulse finely spaced pump/probe delays within the air revival between 8.306 ps and 8.426 ps.	94
Figure 5.6(c): Measured Wigner diagrams for a 2.5 mJ probe pulse finely spaced pump/probe delays within the air revival between 8.306 ps and 8.426 ps.	95
Figure 5.7: First column: measured $I(t)$ and $\Phi(t)$ for a 1.0 mJ probe pulse for selected pump/probe delays. Second column: corresponding $I(\lambda)$ and $\varphi(\lambda)$, with the pre-filamentation spectrum in dashed red lines. Third column: corresponding Wigner plots, with the pre-filamentation Wigner plot inset at the top right.	96
Figure 5.8: First column: measured $I(t)$ and $\Phi(t)$ for a 1.6 mJ probe pulse for selected pump/probe delays. Second column: corresponding $I(\lambda)$ and $\varphi(\lambda)$, with the pre-filamentation spectrum in dashed red lines. Third column: corresponding Wigner plots, with the pre-filamentation Wigner plot inset at the top right.	97
Figure 5.9(a): Measured $I(t)$ and $\Phi(t)$ for a 1.6 mJ probe pulse finely spaced pump/probe delays within the air revival between 8.306 ps and 8.426 ps.	97
Figure 5.9(b): Measured $I(\lambda)$ and $\varphi(\lambda)$ for a 1.6 mJ probe pulse finely spaced pump/probe delays within the air revival between 8.306 ps and 8.426 ps.	98
Figure 5.9(c): Measured Wigner diagrams for a 1.6 mJ probe pulse finely spaced pump/probe delays within the air revival between 8.306 ps and 8.426 ps.	99
Figure 5.10: Air molecular alignment (proportional to Δn) due to a pump pulse at $t=0$ and probe pulse at delay $\tau = 8.366$ ps for several probe pulse energies. The probe pulse envelope is shown with a dashed red line, and the alignment due to only the pump pulse is in green.	100

- Figure 5.11: (i-red) Air molecular alignment due to a sequence of two perpendicularly polarized pulses delayed by $\tau = 8.373$ ps, each with peak intensity 5×10^{13} W/cm². (ii-green) Air alignment due to two pulses synthesized from the sum of the individual response of one pulse at $\tau = 0$ and the other perpendicularly polarized pulse at $\tau = 8.373$ ps. 101
- Figure 5.12: Rotational (green), Kerr (dashed red) and plasma (blue) contributions to Δn in air due to a 1.5 mJ pump pulse at $t=0$ and 1.9mJ probe pulse at delay $\tau = 8.366$ ps for several probe pulse energies. 102
- Figure 5.13: Total Δn in air due to a 1.5 mJ pump pulse at $t=0$ and 1.9 mJ probe pulse at a sequence of pump/probe delays (inset). Δn is synthesized from simulations of the contribution from rotational alignment, instantaneous Kerr effect, and plasma generation. 103
- Figure 5.14: Energy in the probe pulse after filamentation as a function of pump/probe delay. Black line—total probe energy, pink line—probe energy inside 1 mm core, red line—probe energy outside 1 mm core. Dashed lines indicate probe energy in absence of the pump pulse. 107

Chapter 1: Introduction and overview

1. 1 Introduction to filamentation

The invention of high power lasers has made it possible to perform a variety of tasks with optical light that were never before thought realistic. We can now use lasers to machine solids, probe the atmosphere, and shoot down small aircraft. High power, short pulse lasers in particular are useful for surgery, accelerating particles, generation of coherent and incoherent radiation in previously unreachable parts of the electromagnetic spectrum, and probing events that take place on a femtosecond or even attosecond time scale.

Lasers also emit light with such high intensity that the magnitude of the fast oscillating electric field approaches that of the intra-atomic electric field, which is roughly $\frac{e}{(\text{Bohr radius})^2} \sim 2 * 10^7$ statVolts/cm [1]. In other words, the electric field significantly alters the potential of bound electrons, so perturbation theory is not a valid way to describe the electronic response. Therefore, the laser light propagation through solids, liquids, and gases may no longer be accurately described using a linear wave equation. The polarizability of the molecules in the propagating medium is nonlinearly field-dependent, giving rise to nonlinear optical effects.

This dissertation will describe experiments exploring the regime of atmospheric nonlinear optical propagation called *filamentation*. In this process, a laser pulse that has sufficient power will collapse to an intense focus (with tens of microns diameter) without the aid of a lens and propagate at high intensity over many Rayleigh lengths before eventually defocusing. Filamentary propagation of femtosecond pulses can happen in

gaseous or transparent condensed media, and occurs due to the dynamic balance between nonlinear self-focusing of an intense optical pulse and laser plasma-induced defocusing.

Figure 1.1 below shows a schematic of the filamentary process in gas.

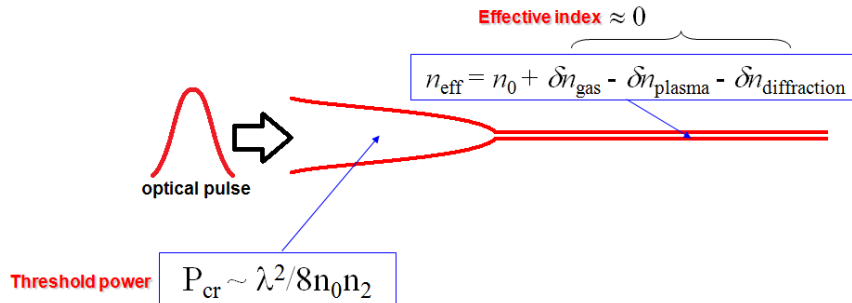


Figure 1.1: Filamentation of ultrashort pulses in gas. P_{cr} is the critical optical power above which the beam will collapse on itself due to self-focusing.

The filamentation effect can be maintained over distances from a few centimeters to hundreds of meters. Filamentation eventually arrests due to diffraction, plasma-induced refraction, energy loss due to ionization, and/or temporal dispersion and modulation of the short pulse. Co-propagating white light generation, conical continuum emission, and a trailing plasma tail accompany short and long-range filaments. In the literature, the term “filament” may refer to either the thin plasma left by the propagating optical pulse or to the localized high intensity region of the pulse itself.

Laser filamentation began to be observed in liquids [2] and solids [3] in the mid to late 1960s and early 1970s. Because the self-focusing nonlinearity (which will be discussed in the next section) is generally three orders of magnitude higher in condensed matter than in the atmosphere, the Q-switched picoseconds-duration laser pulses of that time were not sufficiently intense to filament in air.

The advent of chirped-pulse amplification [4] and ~ 100 fs pulsed Kerr-lens mode locked oscillator cavities [5] in the late 1980s and early 1990s led to the discovery of

atmospheric filamentation, which was first demonstrated at the University of Michigan by Braun et al. in 1995 [6]. In their experiment, Braun et al. used a laser pulse with center wavelength 775 nm, duration 200 fs, and energy as high as 50 mJ. This pulse was collimated to a diameter of 4 mm FWHM and allowed to propagate in atmosphere over a distance 20 m. They found that pulses with energy greater than 2 mJ would slightly focus over that distance, and that pulses with energy greater than 5 mJ would collapse into single or multiple high-intensity filaments after 10 m of propagation and then continue propagating at a filamentary diameter near ~100 microns over the next 10 m. The experiment generated great interest, and in the years since then, many groups have studied the science and applications of ultrafast atmospheric filamentation [7].

1.2 Self-focusing and plasma generation in a filamenting optical pulse

1.2.1 Self-focusing

Self-focusing of an intense laser pulse is due to intensity-dependent refractive index of the medium in which the pulse propagates, which is given by [1]:

$$n = n_0 + n_2 I . \quad (1.1)$$

Here, n_0 is the linear index of refraction, n_2 is the (typically positive) nonlinear index of refraction, and I is the time-averaged intensity of the laser pulse:

$$I = \frac{n_0 c}{2\pi} |E(\omega)|^2 . \quad (1.2)$$

The intensity-dependent refractive index is a result of the nonlinear polarization of molecules in the propagating medium due to a high electric field. The complex

polarization $\tilde{P}(t)$ of a medium as a function of the electric field $\tilde{E}(t) = E(\omega)e^{i\omega t} + E(\omega)^*e^{-i\omega t}$ can be expressed as a power series:

$$\tilde{P}(t) = \bar{\chi}^{(1)}\tilde{E}(t) + \bar{\chi}^{(2)}\tilde{E}(t)^2 + \bar{\chi}^{(3)}\tilde{E}(t)^3 + \dots \quad (1.3)$$

Here, the first coefficient $\bar{\chi}^{(1)}$ is the linear susceptibility tensor, and the later coefficients represent higher order susceptibilities. Equation 1.3 implies that the nonlinearity is instantaneous.

The third order nonlinear susceptibility tensor $\bar{\chi}^{(3)}$ is the term from which self-focusing arises. The nonlinearity is known as the Kerr nonlinearity. For time-averaged fields in isotropic media, we can express the polarization in the frequency domain as the sum of linear and nonlinear components:

$$P(\omega) = \chi^{(1)}E(\omega) + 3\chi^{(3)}(\omega = \omega - \omega + \omega)|E(\omega)|^2E(\omega) = \chi_{\text{eff}}E(\omega). \quad (1.4)$$

The refractive index can be expressed as $n^2 = 1 + 4\pi\chi_{\text{eff}}$. Using this relation and equation 1.1, and ignoring the terms dependent on I^2 we write:

$$n^2 \sim n_0^2 + 2n_0n_2I = 1 + 4\pi\chi^{(1)} + 12\pi\chi^{(3)}|E(\omega)|^2. \quad (1.5)$$

Given that the linear refractive index is $n_0^2 = 1 + 4\pi\chi^{(1)}$, we use equations 1.2 and 1.5 to express the nonlinear refractive index as a function of the third-order susceptibility:

$$n_2 = \frac{12\pi^2\chi^{(3)}}{n_0^2c}. \quad (1.6)$$

A laser pulse will naturally have a gradient in its transverse intensity distribution with the highest intensity generally found at its center. Therefore, the center of the beam will experience the largest index of refraction and the largest phase shift. Over some propagation distance, the effect of the transversely non-uniform phase shift on the laser pulse is the same as that of a focusing lens.

There is a power threshold, called the critical power (P_{cr}) over which the self-focusing of an intense laser pulse will defeat diffraction and eventually cause the pulse collapse to a focus. For a pulse with a transversely Gaussian profile, P_{cr} is given by [7, 8]:

$$P_{cr} = \frac{3.77\lambda_0^2}{8\pi n_0 n_2}. \quad (1.7)$$

The measurement of n_2 using a 300 ps FWHM pulsed laser [9] predicts $P_{cr} = 1.3$ GW, but for pulses of light of wavelength 800 nm and temporal duration ~ 100 fs FWHM, most researchers have measured $P_{cr} \sim 10$ GW. This discrepancy will be discussed in detail in Chapter 4.

Figure 1.2 below shows digital camera images of several 800nm, 130fs FWHM pulses with increasing power, incident on an index card after 6 meters of atmospheric propagation, 1-2 m of which is filamentary propagation. The photos clearly show emergence of a bright hot spot in the center of the beam that appears over the P_{cr} threshold. At higher powers, the on-axis intensity of the pulse is high enough to saturate the CCD.

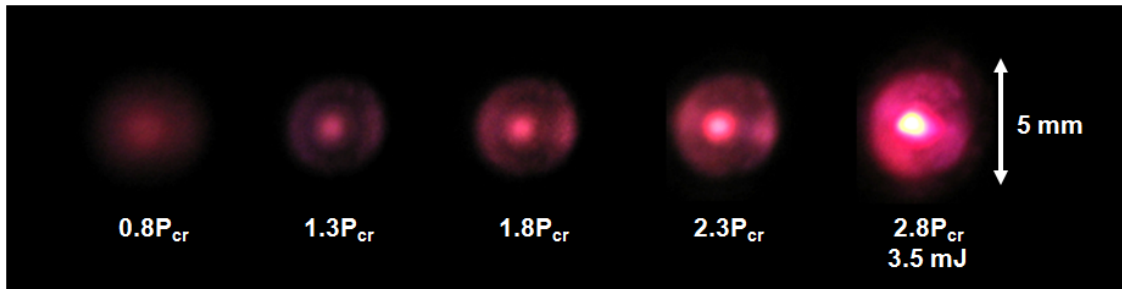


Figure 1.2: Filamenting beam images with increasing power (P_{cr} occurs at 1.25 mJ for a 130 fs pulse).

The work described in this dissertation and reference [10] show that while the instantaneous Kerr nonlinearity is an important part of self-focusing of ultrafast pulses

with $\sim < 40$ fs duration, the self focusing for filamentation of longer pulses in atmosphere is mainly due to a delayed refractive index increase from laser-aligned N_2 and O_2 . Our results, which will be discussed in detail in this dissertation, helped bring this important distinction to light in the scientific community.

1.2.2 Ionization and plasma-induced defocusing

Self-focusing cannot by itself lead to a self-sustaining, high intensity focus over many Rayleigh lengths. In absence of any other nonlinear effect, self-focusing will cause the pulse to collapse and then immediately diffract. What is needed is a refractive effect that competes with self-focusing once the pulse has reached a high enough intensity but has not fully collapsed. This requirement is why ionization is the key to filamentation. Plasma on the optical propagating axis gives a lensing effect opposite to that of the nonlinear index of refraction. For electromagnetic fields with $\omega \gg \omega_p$, the characteristic plasma frequency is:

$$\omega_p^2 = \frac{4\pi N_e e^2}{m_e}. \quad (1.8)$$

The plasma dielectric function is:

$$\epsilon(\omega) = \epsilon(\omega)_{\text{bound electr.}} - \frac{\omega_p^2}{\omega(\omega + i\nu)}, \quad (1.9)$$

where ν is the plasma collision frequency. In atmosphere, $\nu \ll \omega$ (discussed in Section 3.5) and $\epsilon(\omega)_{\text{bound electr.}} \sim 1$, so Equation 1.9 can be simplified, giving the refractive index of a collisionless plasma [11]:

$$n = \sqrt{1 - \frac{\omega_p^2}{\omega^2}}. \quad (1.10)$$

Here, N_e is the number density of electrons, and e and m_e are the electron charge and mass, respectively. As long as the optical frequency $\omega > \omega_p$, the plasma refractive index is always < 1 , giving a negative lensing effect that saturates the self-focusing beam collapse.

Once a laser pulse propagating in atmosphere with $P > P_{cr}$ nearly collapses, it begins to ionize N_2 and O_2 via multi-photon ionization (MPI—the bound electron absorbs enough photons to be ionized) and tunneling ionization (TI—the electric field lowers the Coulomb potential and electrons dominantly escape by tunneling through the lowered potential barrier).

The Keldysh parameter γ_K [12] is proportional the square root of the ratio of the ionization time of a molecule to the laser oscillation period, and given by:

$$\gamma_K = \sqrt{\frac{U_i}{2U_p}}. \quad (1.11)$$

Here, U_i is the ionization potential of the molecule and U_p is the ponderomotive potential of the laser's electric field. If $\gamma_K \gg 1$, MPI is dominant, and if $\gamma_K < 1$, TI is dominant. $\gamma_K \ll 1$ is called the strong-field limit. In this case, the ionization regime is over-the-barrier ionization, where the coulomb potential is completely suppressed and electrons escape without having to tunnel. For the purpose of computationally simulating filamentation, Couairon et al. [13] calculated $\gamma_K \gg 1$ for optical radiation with wavelength 810 nm and intensity $< 10^{14}$ W/cm², and postulated that MPI is the dominant ionization mechanism in filamentation.

After the axial plasma defocuses the filamenting pulse, the third-order nonlinearity eventually causes sufficient nonlinear phase to accumulate, and then self-

focusing and plasma-induced refraction repeat. In this way, both the laser intensity and the plasma density are limited to maximum values—the laser intensity in air is clamped at $\sim 5 \times 10^{13} \text{ W/cm}^2$ [7], which is approximately the ionization threshold of air. The plasma density is also clamped; atmospheric plasma filaments with length $> \sim 1$ meter have a peak density limited to $\sim 10^{16} \text{ cm}^{-3}$ [14, 15], which means that approximately one out of every 1000 atmospheric molecules is singly ionized. These measurements have been confirmed by simulations [16]. Over the course of many meters of propagation, the plasma filament can retain a diameter of tens of microns [17, 14].

An important feature of filamentation is that energy losses due to ionization are counteracted by light outside the central core of the filament gaining nonlinear phase and collapsing into the center of the beam. This phenomenon has the effect of maintaining a high axial intensity and extending the ionized region. Moloney et al. theoretically predicted this effect in 1998 [18]. Eventually, however, diffraction, losses due to ionization, and temporal dispersion arrest the filamentation process.

1.2.3 Self-phase modulation and spectral broadening

During the process of filamentation, the Kerr nonlinearity, molecular rotational excitation and plasma generation all result in the refractive index profile changing quickly in time. These processes impart self-focusing and defocusing effects on the pulse, but they also dramatically change the temporal structure—and therefore spectral content—of the filamenting pulse. Self-phase modulation (SPM) is a catch-all term to describe these effects.

In the case of the Kerr nonlinearity, which is instantaneous, the refractive index profile follows the pulse temporal profile, and generates a time dependent frequency shift according to this expression [7]:

$$\Delta\omega_{\text{Kerr}} = -\frac{\partial\varphi}{\partial t} \sim \frac{\omega_0}{c} z \frac{n_2 \partial I(r, t)}{\partial t}. \quad (1.12)$$

The above equation predicts spectral broadening in both the higher (blue) and lower (red) frequency directions. At the beginning of the pulse, when the refractive index is rising, the beginning of the pulse has a higher phase velocity than the middle, resulting in a red frequency shift at those times. When the intensity-dependent refractive index finally falls, the back end of the pulse has a higher phase velocity than the middle, so there is a blue shift near the back. SPM due to delayed molecular rotational alignment is similarly described, and will be discussed later in the dissertation.

SPM due to plasma generation causes spectral broadening of the filamenting pulse in the blue direction. This effect arises because as the front of the pulse generates plasma, it sees a temporally decreasing refractive index that causes the middle of the pulse to experience a higher phase velocity than the front. The instantaneous frequency shift due to plasma density $N_e(r, t)$ is [7]:

$$\Delta\omega_{\text{plasma}} = -\frac{\partial\varphi}{\partial t} \sim \frac{\omega_0}{c} z \left(\frac{1}{n_0 N_{\text{cr}}} \frac{\partial N_e(r, t)}{\partial t} \right), \quad (1.13)$$

where $N_{\text{cr}} = \frac{\omega^2 m_e}{4\pi e^2}$, the critical plasma density at which the plasma frequency ω_p equals the optical frequency ω .

Spectral broadening in long-range filaments due to SPM from the Kerr nonlinearity, molecular alignment, and plasma generation is dramatic, owing to the long propagation length at high intensity. Figure 1.3 shows the spectrum of a 120 fs, 800 nm

center wavelength, 19 GW peak power pulse before and after it filaments 1 meter in atmosphere with the aid of $f_{\#} = 505$ focusing geometry.

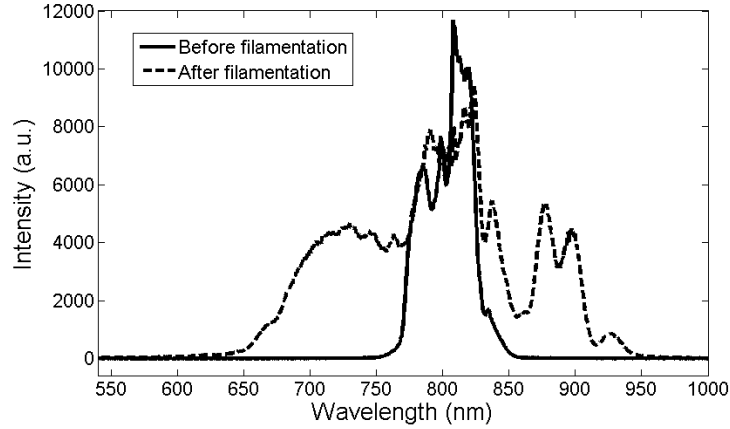


Figure 1.3: spectrum of a 120 fs, 19 GW pulse before (solid line) and after (dashed line) it filaments 1 meter in atmosphere.

The extremely broadband spectrum above has components well within the visible range. White light generation is an easily identified characteristic of ultrafast filamentary propagation.

1.3 Controlling the stability and length of a filament

1.3.1 Multiple filamentation

In experiments, laser pulses with power well above P_{cr} will not collapse into a single, large plasma filament. Instead, nonlinear self-focusing causes smaller transverse beamlets to grow out of non-uniformities in the beam profile. Each of these beamlets continues to self focus and they all eventually collapse into a cluster of filaments. This effect is often called multiple filamentation. Multiple filamentation is a modulational instability whose waves grow as the beam propagates in z like $e^{\gamma_i k_{\perp} z}$ with growth rate γ_i

a function of the transverse spatial frequency ($k_{\perp}^2 = k_x^2 + k_y^2$), maximum intensity I_0 and critical power for a Gaussian beam (Eq. 1.7) [7]:

$$\gamma_i = \frac{k_{\perp}}{2k_0} \sqrt{\frac{8\pi I_0}{P_{cr}} - k_{\perp}^2}. \quad (1.14)$$

Campillo et al. studied multiple filamentation in liquid CS₂ [19] and noted that γ_i was

maximized for an optimal k_{\perp} , given by $k_{\perp}^{\text{opt}} = 2\sqrt{\frac{\pi I_0}{P_{cr}}}$. Once a beam with k_{\perp}^{opt} spatial

modulation collapses into multiple filaments, the distance between filaments is $d_{\text{fil}} = \frac{2\pi}{k_{\perp}^{\text{opt}}}$

[7]. Under conditions of maximal instability, a 1 cm diameter laser pulse with power $100P_{cr}$, when launched into atmosphere, will collapse into filaments 3 mm apart.

Multiple filamentation in atmosphere was studied theoretically and experimentally by Fibich et al. in 2005 [20]. In simulations, they found that due to modulation instability, 10% noise in the input beam profile of a long pulse laser will cause a very high power pulse (hundreds of P_{cr}) to begin filamentation much earlier than a pulse with moderate power (tens of P_{cr}). They found that the self focusing distance in the very high power case scales as $1/P$, while that of the moderate power case scales as $1/P^{1/2}$. Their experiments using a 45 fs, 800 nm pulse corroborated their simulations.

Figure 1.4 below shows a camera image of a multiply-filamenting beam taken by Rodriguez et al. in 2004 [21]. This image strikingly contrasts with the single, stable filament images in Figure 1.2.

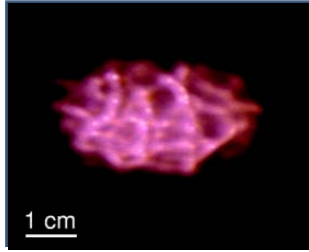


Figure 1.4: Multiply filamenting beam profile [21].

Multiple filamentation makes it impractical to do detailed studies on filamentation, since the position and location of the filaments will vary significantly on a shot-to-shot basis. Additionally, multiple filamentation limits the ability to make consistent, long, high-density plasma channels for the applications that will be discussed in the next section.

1.3.2 Experimental attempts to stabilize and lengthen plasma filaments

To date, many groups have published their attempts to stabilize and enhance the filamentation process. Often, a laser pulse will be sent through a hard circular aperture before it filaments. The aperture causes a radially symmetric diffraction pattern in the far field with a hot spot at the center, and in this way encourages single filaments to appear in the center of the beam. In 2004, Fibich et al. were able to control a multiply filamenting pulse by angling their 2 m focusing lens by 20° [22]. This setup gave them a single, transversely stable filament instead of 1-3 filaments with five times the variance in filament position. Other groups passed a pulse through a phase mask to better organize or suppress multiple filaments [23] and to stabilize a single filament [24].

Theory [25] and experiment [26] have shown that giving a filamenting optical pulse an initial negative chirp can change the collapse distance and lengthen the filament. This effect occurs because air is a weakly dispersive medium in which a negatively

chirped pulse will propagate some distance before it re-compresses and attains a high enough power to self-focus and cause filamentation. The group velocity dispersion (GVD or β_2) of air for an 800 nm optical pulse is $2.2 \cdot 10^{-31} \text{ s}^2/\text{cm}$ [16]. The duration Δt of an initially transform-limited 800nm pulse with initial time duration Δt_0 that has propagated a distance z is given by this expression [27]:

$$\Delta t = \Delta t_0 \sqrt{1 + z \frac{\text{GVD}}{\Delta t_0^2}}. \quad (1.15)$$

Using Eq. 1.15, an 800 nm pulse that has been negatively chirped from 100 fs to 200 fs duration will re-compress after propagating 136 meters.

Recently, we showed that rotationally aligned N_2 and O_2 by a filamenting optical pulse can be used to steer and enhance the on-axis filament intensity [10]. This dissertation will present those results and new measurements on similarly enhanced filaments showing higher plasma density, including tripling of the length of the plasma.

1.4 Applications of filamentation

The three major products of filamentation—the long region of high-intensity laser light, the long plasma tail, and the co-propagating broadband white light—are useful for a variety of applications.

1.4.1 Remote sensing

Remote sensing, the detection of chemicals from a standoff distance, is one application of filamentation. Filaments can ionize molecules from a far distance in order to probe the composition of the atmosphere [27, 28] and to obtain characteristic spectra

of biological materials. Figure 1.5 below shows remote femtosecond-induced breakdown spectroscopy (FIBS) performed with an 800 nm filamenting pulse by Xu et al. in 2006 on egg white [29].

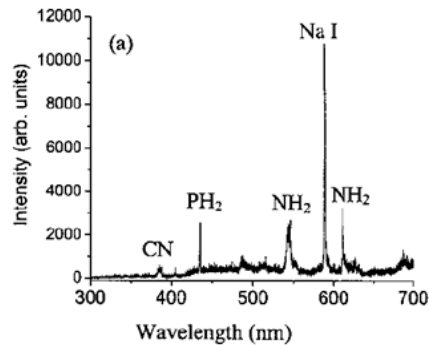


Figure 1.5: Femtosecond-induced breakdown spectrum of egg white [29].

Rairoux et al. [27] sent a 2.2 TW filamenting optical pulse hundreds of meters vertically in the atmosphere and collected the broadband backscattered supercontinuum light into a gated spectrometer. The gated spectrometer helped them to measure time-resolved spectra in the visible-near IR range, which allowed them to collect spectra from different atmospheric heights with a range resolution of 100 m. The measured absorption lines due to the characteristic roto-vibrational transitions of O₂ and water vapor correlated well with tabulated spectroscopic data.

1.4.2 Guiding of high-voltage discharges

The plasma left by a filamenting pulse has also been used to guide high-voltage electric discharges [30, 31] by providing an ohmic channel along which current can travel. This effect may one day be useful for steering lightning away from buildings. Rodriguez et al.'s use of optically-generated plasma filaments to guide an electric breakdown over several meters is pictured below in figure 1.6 [32].



Figure 1.6: Top—several meter-long electrical discharge with no filaments present. Bottom—guiding of the discharge by optically generated plasma filaments [32].

1.4.3 Generation of few-cycle optical pulses

The coherent, broadband white light generated through filamentary propagation can also be used to create pulses of light much shorter than the initially filamenting pulse. In a 2004 experiment, Hauri et. al. [33] sent an initially 43 fs FWHM pulse into an argon gas-filled cell. Upon filamentation, defocusing and exiting the cell, the broadened spectrum was re-compressed by chirped mirrors to 5.7 fs [33]. The chirped mirrors were necessary to compensate for pulse temporal dispersion during filamentation and in the exit window of the gas cell. Since then, Stibenz et al. have generated similarly shortened pulses without the use of chirped mirrors by carefully varying the gas species, pressure, and input pulse energy [34]. Some of the results of that experiment are shown below in Figure 1.7.

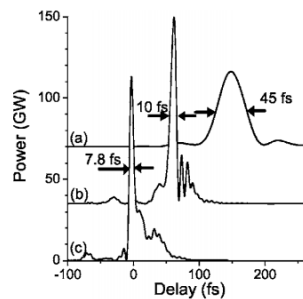


Figure 1.7: Self-compression of a 45 fs, 800 nm pulse after filamentation in a krypton gas cell. A) is the initial pulse, B) is the pulse before it exits the gas cell, and C) is the pulse after it passes through the gas cell exit window [34].

1.4.4 High harmonic generation

The filamentation of ~ 100 fs pulses in gaseous xenon [35] and neon [36] has been used to efficiently generate high harmonics. In the case of the xenon experiment, Lange et al. generated a 70 cm long filament using a 3 mJ, 130 fs pulse focused with $f_{\#}=140$ geometry. The tail end of the filament entered the xenon gas cell through a 0.1 mm thick silica plate and over a propagating distance of 3.5 mm generated harmonics up to the 15th order (22 eV).

1.4.5 Filaments as a source of terahertz radiation

Atmospheric filaments are also a promising source of terahertz (THz) frequency radiation. THz radiation is useful for chemical detection because, it can propagate through thin barriers and is non-ionizing, and because many chemicals have characteristic spectral absorption lines in that range. For example, THz radiation has been used to identify the explosive 1,3,5-trinitro-1,3,5-triazacyclohexane (RDX) [37] and HCl and ammonia in vapor phase [38].

However, this part of the electromagnetic spectrum is not easily accessible; broadband THz is difficult to generate and detect. Practically, many groups that perform THz spectroscopy generate the necessary broadband THz signal through the use of an ultrashort (~ 100 fs) pulse incident on either a GaAs photoconductive antenna biased at high voltage or a ZnTe crystal that allows phase-matched optical rectification. Recently however, broadband, high-intensity THz radiation has been produced from a laser-induced spark in air [39]. This and similar experiments employ the use of a two-color

~100 fs pulse (fundamental and second harmonic) tightly focused in air. The asymmetrical ionization dynamics of the plasma result in a conversion efficiency of ~0.02% [40] and produces tens of μJ of THz radiation—much higher than the maximally ~1 μJ radiation that the earlier mentioned techniques produce.

THz radiation has also been measured emitting from a filament left by a single 800 nm pulse [41, 42]. The interesting aspect of using an atmospheric filament to produce THz is the promise of a remotely generated THz source and the simplicity of the setup; only a femtosecond laser pulse is necessary. Unfortunately, the THz signal strength from long-range filamenting optical pulses is so low that it is impossible to measure using electro-optic sampling in ZnTe or GaP—a standard technique employed by THz spectroscopy. The experiments referred to above [41, 42] used sensitive 2 GHz bandwidth heterodyne detectors and measured radiation near 100 GHz, the detectors' upper frequency limit. Later, they used a helium-cooled bolometer with filters to ascertain that most of the radiation was indeed between 0.5 and 3 THz [43].

1.4.6 Optical waveguides made from filament-induced damage in solids

Filamentation in solids and liquids requires a lower intensity laser pulse than in atmosphere, and it also has several important applications. Filamentary propagation often leads to visible but quite transparent damage streaks in solids. Davis et al. [44] found that focused 810 nm, 120 fs pulses in silica glass samples left cylindrical damage streaks with ~0.035 higher refractive index in the center of the bulk media without cracking it. They scanned the filamenting region through the glass sample to create a

planar region that they surmised would be able to act as an optical waveguide. In ref [45], the same group used the technique to write single mode waveguides with 1 GW 800 nm, 120 fs pulses. Schaffer et al. [46] were able to write 0.5 micron diameter, single mode waveguides with a <1.5 MW beam, where 1.5 MW is P_{cr} for the Corning 2011 glass medium they used.

Davis et al. suggested [44] that the damage mechanism that explains the densification of the glass exposed to the filamenting pulse may be either the localized heating, melting and cooling of the glass, or generation of trapped excitons, which could locally weaken bonds and lead to a relaxed molecular configuration [47].

1.4.7 Filaments as an underwater acoustic source

Filamentation of liquids has several interesting applications, one of which is that an ionization event in water can be used as an underwater acoustic source for sonar applications. Vogel et al. [48] studied the shock wave emission and cavitation bubble expansion due to optical breakdown of water due to focused 6 ns (10 mJ) and 30 ps (1 mJ) pulses with 1064 nm wavelength. They found that 40-70% of the optical energy coupled to mechanical energy in the shock wave and cavitation bubble.

Hornstein et al. at the Naval Research Laboratory [49] generated acoustic signals 8 meters below the surface of water using a filamenting 400 nm pulse with $P > P_{cr}$. They used $P_{cr} = 1.1$ MW, which was calculated in our laboratory [50] using Single-shot Supercontinuum Spectral Interferometry (SSSI), a method to sensitively measure time-resolved nonlinear refractive response of an optical medium to an ultrafast pulse. SSSI

will be discussed in detail in Chapter 3. The limited depth of optical filamentation in water is due to large GVD and optical absorption.

1.4.8 Microsurgery using ultrashort pulses

Microsurgery is another useful application of femtosecond filamentation in liquid and solid media. Vogel et al.'s water breakdown mentioned above [48] was intentionally done with laser parameters similar to those used in intra-ocular surgery. Juhasz et al. [51] found that nonlinear self-focusing and ionization in corneal tissue enabled a femtosecond-scale pulse to generate smaller shock waves and cavitation bubbles than those generated by picoseconds or nanosecond-scale pulses, resulting in a damage area confined to a smaller, more precise location. Vogel and Venugopalan [52] also note that focused femtosecond pulses are able to generate ionization events in biological tissues without significantly heating the region, resulting in ablation or dissection processes which are very precisely localized and do not unnecessarily kill surrounding cells and structures.

1.5 Chapter synopsis

This dissertation will primarily deal with our discovery that the rotational response of N_2 and O_2 is the dominant nonlinearity in the filamentation of >40 fs pulses in air. Prior to that discussion, Chapter 2 will describe our lab's several optical pulse diagnostics, which are crucial to any experiments using ultrafast pulses and especially vital to our filament diagnostics.

Chapter 3 describes the quantum mechanical nature of the rotation and alignment of laser-irradiated linear molecules. Single-shot, time-resolved measurements of molecular alignment are presented and compared to theoretical calculations.

The exploitation of molecular alignment in order to enhance on-axis intensity and spectral shape of a filamenting probe pulse will be chronicled in Chapter 4. Chapter 5 describes a novel, interferometric, time-resolved method to directly measure the axial plasma density profile in a filament and presents measurements showing enhancement of the maximum plasma density and plasma length due to pre-aligned air molecules. Chapter 5 also shows measurements of the electric field envelope of enhanced filamenting pulses and discusses the role of molecular alignment in both spatially confining and temporally shaping those pulses.

Chapter 2: Measuring an ultrashort laser pulse

2.1 Introduction to ultrashort laser pulses

In our experiments, we use pulses of light that can be as short as 40 fs FWHM, and as energetic as 80 mJ. We are able to generate such short pulses through the use of a Kerr-lens mode-locked (KLM) laser oscillator, and we amplify those pulses using the chirped pulse amplification (CPA) technique. Both these techniques are popularly based on the use of titanium-doped sapphire (Ti:sapphire) crystals as a laser gain medium. CPA is also done with neodymium-doped glass as the amplification medium for systems with repetition rate 10 Hz and lower.

Sapphire—an Al_2O_3 crystal—when doped with titanium atoms, becomes a broadband gain medium. Ti:sapphire absorption peaks near 500 nm. When the crystal is appropriately pumped, it supports laser gain at wavelengths ~650-1100 nm. This feature makes it an attractive gain medium for broadly tunable continuous-wave (CW) lasers, and also for broadband, short pulse lasers.

If broadband, coherent light is phased properly, the spectral components constructively interfere and result in a train of single, short pulses whose duration is inversely proportional to their spectral bandwidth. In the case of a pulse of light with a Gaussian spectral intensity profile with FWHM $\Delta\nu$, the Fourier transform-limited FWHM time duration is given by:

$$\Delta t = \frac{0.44}{\Delta\nu}. \quad (2.1)$$

0.44 is the minimum time-bandwidth product for an electromagnetic pulse, which is a fundamental property of the Fourier transform of classical electromagnetic fields. The

Ti:sapphire CPA system used for filamentation experiments in this dissertation typically outputs pulses with FWHM bandwidth $\Delta\lambda = 25$ nm, centered at $\lambda_0 = 800$ nm. This corresponds to transform-limited pulse duration of 38 fs.

A laser cavity built around Ti:sapphire will not naturally lase in broadband, short-pulse mode. KLM has been used since around 1990 [5], in concert with intra-cavity dispersion compensation, to passively mode-lock Ti:sapphire lasers so that they output pulse trains of nanoJoule-scale pulses with sub-100 fs time duration. Further amplifying these pulses is difficult because, while they are being amplified, their peak power becomes high enough that they can destroy the gain medium and surrounding optics. The previous chapter's discussion of self-focusing, filamentation and damage mechanisms in solids explains the limitations of propagating (and amplifying) high-power pulses in solid media; P_{cr} in solids is ~ 1 MW.

CPA was developed by Strickland and Mourou in 1985 [4] to sidestep this limitation. In CPA, a broadband pulse emitted from an oscillator is chirped to hundreds of picoseconds by a grating stretcher and amplified by a Ti:sapphire-based regenerative amplifier and/or multi-pass power amplifier, then expanded by a telescope and compressed down to near the transform limit by a grating compressor. Ultrafast laser systems based on KLM and CPA are now ubiquitous and can be purchased off-the-shelf.

Ultrashort pulses are by common definition a few picoseconds ($1 \text{ ps} = 10^{-12} \text{ s}$) or shorter in duration, but the fastest electronic response time is in the $>\sim 10$ ps scale. This means, for example, that no photodiode or CCD element can by itself measure the temporal profile of an ultrashort pulse. However, in experiments using such pulses, knowing the pulse temporal profile $I(t)$ is extremely important.

However, $I(t)$ does not uniquely describe the electric field $E(t) = \text{Re}(\tilde{E}(t))$.

Ultrashort pulses are broadband and often intense enough that material dispersion and nonlinear processes will significantly alter their temporal profile and time-dependent spectral content. Full knowledge of $E(t)$ is crucial in many experiments done using such pulses. $E(t)$ is fully specified in the frequency domain by:

$$\tilde{E}(\omega) = |\tilde{E}(\omega)|e^{-i(\omega_0 t + \varphi(\omega))} \quad (2.2)$$

Here, $|\tilde{E}(\omega)|$ is the magnitude of the spectrum of the electric field, ω_0 is the center frequency, and $\varphi(\omega)$ is the spectral phase of the pulse. $|\tilde{E}(\omega)|$ is easily measured with a spectrometer, and the more sophisticated ultrashort pulse diagnostics discussed later in this chapter can measure $\varphi(\omega)$.

2.2 Autocorrelation

2.2.1 The intensity autocorrelation

One simple way to measure an ultrashort pulse is to split gate it with its own copy. This method is called intensity autocorrelation, and can most simply be performed by sending the two copies of the pulse onto a detection system with intensity-squared-dependent response while scanning the delay (τ) of one of the pulses in small steps. Two examples of detection systems that provide the appropriate response are a two-photon photodiode and a Beta barium borate (BBO) crystal with a linear photodetector. The photocurrent output of a two-photon photodiode is proportional to I^2 . In BBO, the second harmonic generated (SHG) electric field $|\tilde{E}(2\omega)| \propto I(\omega)$, so $I(2\omega)$ is also $\propto I(\omega)^2$. Monopotassium phosphate (KDP) is another crystal that behaves similarly to BBO. BBO

has higher SHG efficiency than KDP but roughly twice the group velocity mismatch between ω and 2ω [53]. Figure 2.1 (below) shows the design of an interferometric intensity autocorrelator based on a Michelson interferometer.

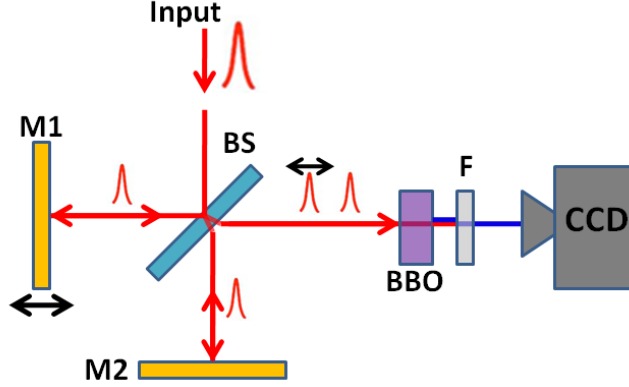


Figure 2.1: Scanning delay Michelson autocorrelator. M1 is a mirror on a scanning delay stage, M2 is a static mirror, BS is a 50/50 beamsplitter, and F is a filter that only passes second harmonic frequency light.

If the delay range allows both pulses to scan through each other in small enough steps, the interferometric autocorrelation signal $S(\tau)$ is:

$$S(\tau) = \int_{-\infty}^{\infty} |[E(t) + E(t - \tau)]|^2 dt. \quad (2.3)$$

If we define $E(t)$ as the real part of the complex valued function $\varepsilon(t)e^{i\omega_0 t + i\varphi(t)}$, where ω_0 is the center frequency of the pulse, and $\varepsilon(t)$ is the slowly varying envelope, and then expand the integrand of Eq. 2.3, we get [54]:

$$S(\tau) = A_0(\tau) + \text{Re}[A_1(\tau)e^{-i\omega_0\tau}] + \text{Re}[A_2(\tau)e^{-2i\omega_0\tau}], \quad (2.4)$$

where

$$A_0(\tau) = \int_{-\infty}^{\infty} [\varepsilon^4(t) + \varepsilon^4(t - \tau) + 4\varepsilon^2(t)\varepsilon^2(t - \tau)] dt \quad (2.5)$$

$$A_1(\tau) = 4 \int_{-\infty}^{\infty} \varepsilon(t - \tau)\varepsilon(t)[\varepsilon^2(t - \tau) + \varepsilon^2(t)]e^{i(\varphi(t-\tau)-\varphi(t))} dt \quad (2.6)$$

$$A_2(\tau) = 2 \int_{-\infty}^{\infty} \varepsilon^2(t - \tau) \varepsilon^2(t) e^{2i(\varphi(t-\tau) - \varphi(t))} dt \quad (2.7)$$

$A_1(\tau)$ and $A_2(\tau)$ are fast oscillating terms from interference fringes which may or may not be visible, depending on the alignment and stability of the interferometer and the chirp of the pulse. The phase of the interference pattern is $\varphi(t - \tau) - \varphi(t)$. This phase information does not allow full recovery of $\varphi(t)$, but will give the chirp of the pulse.

The first and second terms in the integrand of Eq. 2.5 are DC terms in the view of any detector. However, using $E^2(t) = \varepsilon^2(t) \propto I(t)$, the third term is proportional to the intensity autocorrelation $A(\tau)$ of a signal $I(t)$:

$$A(\tau) = \int_{-\infty}^{\infty} I(t) I(t - \tau) dt. \quad (2.8)$$

From this equation, it is clear that $A(\tau)$ must be symmetric in τ , regardless of the symmetry of $I(t)$. This means that, though an interferometric intensity autocorrelation gives us some idea of the temporal structure of the input pulse, it cannot tell us the true direction of time. For a given $A(\tau)$, there is no unique $I(t)$. Even when the interference fringes are resolved, they cannot give us $I(t)$ or $E(t)$, since $\varphi(\omega)$ cannot be recovered but for a linear chirp parameter.

Intensity autocorrelation is not the ideal method for characterization of a complicated pulse, but it is generally sufficient for a simple pulse. If a shape of the input pulse is assumed, the temporal width of the measured intensity autocorrelation is proportional to the temporal width of $I(t)$ by a constant factor. In the case of a Gaussian intensity profile, $\Delta t_{I(t)} = \frac{1}{\sqrt{2}} \Delta \tau_{A(\tau)}$.

2.2.2 Single-shot autocorrelator

An intensity autocorrelator is a very useful tool to have in an ultrafast laser lab, but the retrieved autocorrelation will only give average properties if the input pulse has large shot-to-shot fluctuations in energy or temporal profile.

The solution to this is to build a single-shot autocorrelator (SSA). This device will faithfully recover $A(\tau)$ in a single shot of the input laser. A schematic of a SSA we built and used in several of our experiments is below:

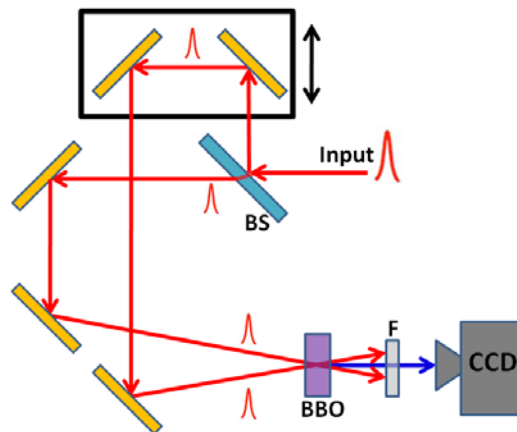


Figure 2.2: Single-shot autocorrelator. The delay rail at the top is not scanning; it is set so that both pulses are coincident on the BBO crystal.

In an SSA, the input pulse is split into identical copies that are then coincident on the nonlinear crystal with a crossing angle φ . While each pulse will generate blue second harmonic light in the same direction as their own propagation, if they are spatially *and* temporally coincident on the crystal, they will also generate blue sum frequency (SFG) light in the forward direction—the direction along the sum of the two incident k -vectors.

The geometry of the setup determines that the width of the SFG beam directly corresponds to the amount of time the two pulses spent overlapped in the crystal. The sum frequency light beam can be spatially filtered from the incident and SHG beams and imaged onto a CCD camera. In this manner, the horizontal line-out of the CCD image is

the autocorrelation of the input pulse. The simple equation mapping CCD image width Δx to autocorrelation width $\Delta \tau$ is linear for small incidence angle φ :

$$\Delta \tau = \frac{\Delta x}{c} \sin\left(\frac{\theta}{2}\right) \approx \frac{\Delta x \theta}{2c}. \quad (2.9)$$

The above relation will hold true as long as each of the two incoming pulses has a beam profile that is spatially uniform in the axis that is in the plane of incidence and perpendicular to the propagation direction, and a temporal profile that is constant over the same direction.

The calibration of the SSA is simple. In fact, the constant $\frac{\theta}{2c}$ does not need to be calculated by measuring φ ; it can easily be experimentally measured by manually scanning the delay of one of the two input pulses by small steps, each time recording the autocorrelation. The autocorrelation will likewise move in steps across the CCD screen, and the distance between each retrieved peak will correspond to the applied delay. A linear fit gives delay as a function of screen pixel.

The output of our SSA is pictured below in Figure 2.3. The left image is a raw CCD image, and the right image is the autocorrelation, given by the horizontal line-out of the CCD image. Our delay resolution is typically ~ 4 fs/pixel.

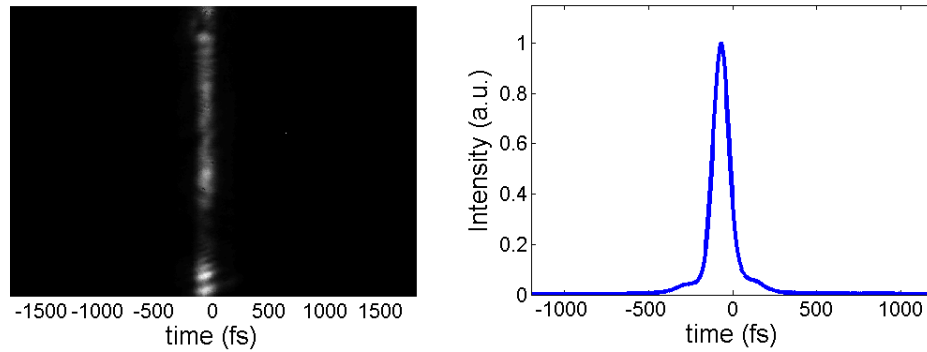


Figure 2.3: Raw SSA image (left) and retrieved autocorrelation (right).

2.3 FROG – Frequency-resolved Optical Gating

2.3.1 Polarization-gated FROG

As mentioned before, multi- and single-shot intensity autocorrelators are useful devices because of their simplicity, but in the arena of ultrashort pulse measurement, they fail in three respects: the intensity autocorrelation does not give the true pulse shape, does not tell us the direction of time, and does not retrieve the pulse spectral phase $\varphi(\omega)$.

In 1993, Kane and Trebino introduced Frequency-resolved Optical Gating (FROG) [55] as a single-shot device capable of fully characterizing an ultrashort pulse.

Figure 2.4 below shows an image of the a FROG setup [55].

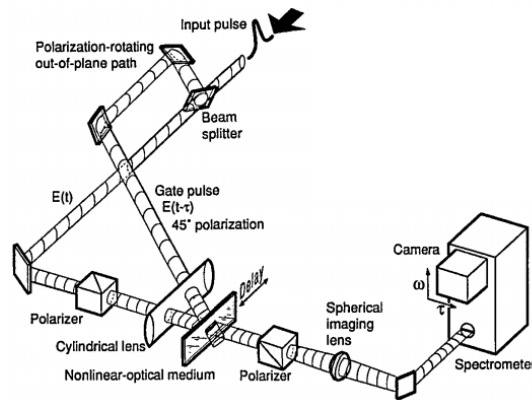


Figure 2.4: Frequency-resolved optical gating setup [55]

In FROG, as in an autocorrelation, an ultrashort pulse is split into two: the gating pulse and the main pulse. The main pulse is focused with a cylindrical lens into a thin sample of any nonlinear optical medium with only instantaneous response (an optical glass like fused silica works well). The gating pulse has its polarization rotated by 45° and then is sent into the cylindrical lens at an angle with respect to the main pulse. The

two pulses cross in the medium in a similar fashion to the SSA. The main pulse then enters a polarizing beam splitter cube designed to completely divert all of its light.

However, some of the main pulse passes through the polarizer. This light has been polarization rotated by the gating pulse through Kerr-induced birefringence, an effect which falls under a group of nonlinear optical effects called cross-phase modulation (XPM). As in the simple Kerr effect described in the previous chapter, the gating pulse causes the index of refraction to instantaneously increase as it scans through the nonlinear medium. However, in the case of cross-coupling, where a strong gating pulse gates a weak main pulse, the birefringence of the Kerr effect contributes to the gating.

In the case where the gating pulse $E(\omega)$ and main pulse $E(\omega')$ have the same polarization direction and are combined in a nonlinear, centro-symmetric medium, the polarization experienced by the main pulse is [1]:

$$P_{\parallel}(\omega') = \chi^{(1)}E(\omega') + 6\chi^{(3)}(\omega' = \omega' + \omega - \omega)|E(\omega)|^2E(\omega'). \quad (2.10)$$

In the case of perpendicularly polarized pulses, the main pulse polarization is:

$$P_{\perp}(\omega') = \chi^{(1)}E(\omega') + 2\chi^{(3)}(\omega' = \omega' + \omega - \omega)|E(\omega)|^2E(\omega'). \quad (2.11)$$

The difference in degeneracy factors means that there is a birefringent component in the increase in nonlinear refractive index experienced by the main pulse. If, as in the case of FROG, the gating pulse is neither parallel nor perpendicularly polarized with respect to the main pulse, it will impart a polarization rotation to the main pulse.

As the gating pulse scans over the main pulse from left to right in the nonlinear medium, it introduces a orthogonal polarization component to the temporal fraction of the main pulse that it overlaps. Each vertical slice of the beam that passes through the

polarizer is a temporally gated fraction of the original pulse, with the earlier gated fractions of the pulse on the left of the beam and the later gated fractions on the right. A spherical lens then brings the polarizer output to a line focus on the slit of an imaging spectrometer. The CCD chip inside the imaging spectrometer collects a two-dimensional spectrum. The vertical axis, perpendicular to the slit, is the spectral axis. The horizontal axis, due to the gate and main pulse interaction geometry, is a delay axis. The 2-D pattern is called a *FROG trace*.

One way to intuitively interpret the FROG trace is to imagine that it shows the spectrum of the main pulse at any given time, so the entire image would show the evolution of spectral components of the main pulse over its duration. This explanation is clearly not accurate, because the gating pulse has finite, but nonzero time duration. However, a very accurate $E(t)$ of the pulse can be extracted by applying an iterative computational algorithm on the FROG trace. The algorithm involves alternately applying a fast Fourier transform to the spectral and temporal axes of the image [55].

The FROG technique is accurate and can be single-shot, but it is inconvenient for two reasons. For one, the iterative algorithm required to extract $E(t)$ is time-consuming enough that real-time pulse measurement is difficult. Second, it requires a uniform input beam profile—as in the case of the SSA, the input pulse must be spatially and temporally uniform over the horizontal axis. Third, the apparatus is large and complex, as is clear from the diagram in Figure 2.4. Trebino and his colleagues solved the last issue by inventing a much simpler version of FROG called GRENOUILLE [56]. This long acronym stands for “GRating-Eliminated No-nonsense Observation of Ultrafast Incident Laser Light E-fields.”

2.3.2 GRENOUILLE

While former graduate students had built a FROG for our lab in the past, we found the GRENOUILLE design much simpler, and built one for the lab that was used for many years. Figure 2.5 below shows the GRENOUILLE schematic [56]:

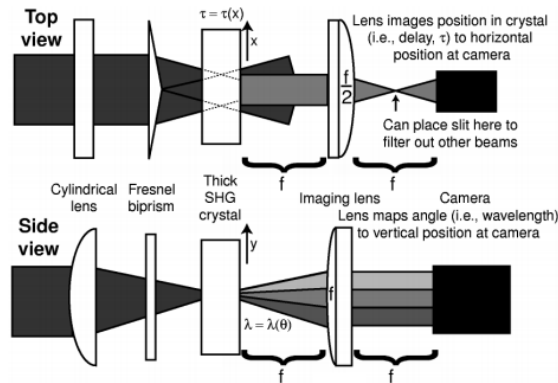


Figure 2.5: GRENOUILLE schematic [56].

The first difference between GRENOUILLE and FROG is that the beam-splitting is done after the cylindrical lens with a Fresnel bi-prism, rather than a beamsplitter. The bi-prism splits the beam into halves and sends them at equal but opposite angles into a few-mm thick BBO crystal, where they are both coincident and at horizontal line focus due to the cylindrical lens. If the BBO crystal had been thin, the blue light emitted in the forward direction would be in the shape of the simple intensity autocorrelation, where the delay axis is horizontal and space-to-delay mapping depends on Equation 2.9. However, the thickness of the BBO crystal severely limits its phase-matching bandwidth. The cylindrical lens allows the autocorrelation to be generated and propagate through the crystal at a range of vertically swept angles, each of which will only phase-match for a small fraction of the total bandwidth of the input pulse. As a result, the emanating,

divergent pattern of blue light is a spectrally resolved autocorrelation. Two cylindrical lenses after the crystal are then used to image this pattern onto a 2D CCD array.

The “spectrally resolved autocorrelation” generated by GRENOUILLE is very similar to the previously described FROG trace. As with the FROG trace, the GRENOUILLE trace has a horizontal time axis and a vertical spectral axis. However, the GRENOUILLE trace is always symmetrical. Therefore, a slightly different iterative algorithm must be applied to the trace to discover $E(t)$, and while the shape of $E(t)$ may be very accurate, the direction of time is unresolved. Figure 2.5 below shows real GRENOUILLE traces and retrieved $I(t)$ for a 70fs FWHM, 800nm pulse.

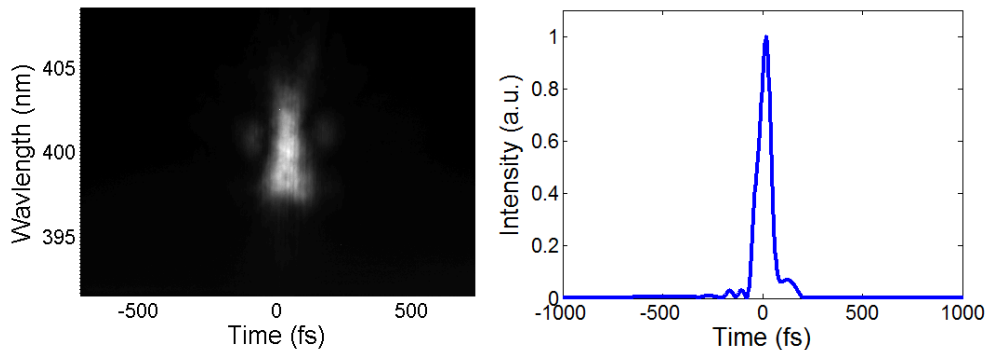


Figure 2.6: GRENOUILLE trace (left) and retrieved $I(t)$ (right) for a 70fs pulse.

GRENOUILLE is very simple to align. No polarization rotation is necessary, and the bi-prism makes careful angular alignment and delay line calibration unnecessary. Unfortunately, the optically thicker components of the GRENOUILLE significantly disperse laser pulses shorter than 50 fs FWHM. Also, the spatial uniformity of the input pulse must be even better than that of FROG. The beam must not only be horizontally uniform to get the correct autocorrelation, but must be vertically uniform to ensure an accurate spectrum. Even so, the simplicity of alignment and lack of a spectrometer make GRENOUILLE a useful and reliable tool to measure a wide range of ultrashort pulses.

2.4 SPIDER – Spectral Phase Interferometry for Direct Electric-field

Reconstruction

2.4.1 SPIDER algorithm

As mentioned in the first section of this chapter, the temporal shape of an electromagnetic field is uniquely determined by the magnitude of its spectrum and its spectral phase $\varphi(\omega)$ —the relative phase of all spectral components. FROG, mentioned in the previous section, does faithfully retrieve the spectral phase of an ultrashort pulse. Aside from space constraints, the only drawbacks of FROG are the time taken to extract $E(t)$ from the FROG trace and the requirement of a clean spatial profile. SPIDER, a different technique, stands for Spectral Phase Interferometry for Direct Electric-field Reconstruction, and was developed by Iaconis and Walmsley in 1998 [57]. Speed-wise, SPIDER is a better technique than FROG because it performs linear (non-iterative) retrieval of $\varphi(\omega)$. SPIDER is also an improvement over FROG because it does not involve the interference of spatially separated parts of the input beam, and therefore does not require transverse uniformity of the input beam's intensity and temporal profile.

SPIDER computes $\varphi(\omega)$ through interferometry, which is a means of sensitively measuring phase differences between two pulses of light. If two identical pulses are delayed by time $\Delta\tau$ and collinearly enter a spectrometer, the signal is:

$$\begin{aligned} S(\omega) &= |\tilde{E}_1(\omega) + \tilde{E}_2(\omega)|^2 = \left| |\tilde{E}(\omega)|e^{i\omega t} + |\tilde{E}(\omega)|e^{i\omega(t-\Delta\tau)} \right|^2 \\ &= 2|\tilde{E}(\omega)|^2 + |\tilde{E}(\omega)|^2 \cos(\omega\Delta\tau). \end{aligned} \quad (2.12)$$

The output spectrum will have the same slowly varying amplitude as that of a single pulse, but an interference pattern will appear overlaid on that signal, with a constant

oscillation frequency spacing $\Delta\omega = 2\pi/\Delta\tau$. From Equation 2.12, it is clear that if we simply split an unknown pulse in two, delay them and then combine them in a spectrometer, the signal will give us only the spectrum of the original pulse and the delay between the two pulses.

SPIDER is spectral interferometry of two pulses that have identical intensity profile, are delayed from one another by $\Delta\tau$, but have slightly different center wavelength. The pulses' spectra are *sheared* by amount Ω (angular frequency) with respect to one another. In this case, the spacing between fringes of their spectral interference pattern is no longer uniform. The signal $S(\omega)$ in the spectrometer is:

$$S(\omega) = |\tilde{E}(\omega)|^2 + |\tilde{E}(\omega + \Omega)|^2 + 2|\tilde{E}(\omega)\tilde{E}(\omega + \Omega)| \cos(\Phi(\omega)). \quad (2.13)$$

$\Phi(\omega)$, the phase of the oscillation in the interference pattern, is related to the fundamental spectral phase $\varphi(\omega)$:

$$\Phi(\omega) = \varphi(\omega + \Omega) - \varphi(\omega) + \omega\Delta\tau. \quad (2.14)$$

The retrieval of the spectral phase from this interference pattern is simple. First, we get $\Phi(\omega)$ using the technique described by Takeda et al. in 1982 [58]. The technique involves first taking fast Fourier transform (FFT) of the spectrometer signal. In the Fourier domain, we filter out any signal that is not the spectral frequency of the interference pattern, which means cutting off the DC spectrum and any high frequency noise. Then we perform an inverse FFT and subtract from the signal the linear phase $\omega\Delta\tau$.

This procedure leaves us with $\varphi(\omega + \Omega) - \varphi(\omega)$, from which $\varphi(\omega)$ is extracted by integration, as long as $2\pi/\Omega$ is longer than the time duration of the pulse (this is the Whitaker-Shannon sampling theorem). It is important to remember that the shear Ω must

not be too large—certainly nowhere near as large as the bandwidth of the entire pulse spectrum—or the sheared spectra will not interfere at all in the spectrometer. An additional constraint on SPIDER retrieval of $\varphi(\omega)$ is that the spectrum must vary slowly with respect to the interference pattern oscillation frequency which is $\sim\Delta\omega$.

The full electric field $\tilde{E}(\omega)$ is calculated by using Eq. 2.2 to apply $\varphi(\omega)$ to the electric field spectrum $|\tilde{E}(\omega)|$ (the square root of the intensity spectrum $I(\omega)$). Then we get $I(t)$ from the inverse Fourier transform:

$$I(t) \propto |\tilde{E}(t)|^2 = \left| \frac{1}{2\pi} \int_{-\infty}^{\infty} \tilde{E}(\omega) e^{i\omega t} d\omega \right|^2. \quad (2.15)$$

2.4.2 SPIDER apparatus

The SPIDER algorithm described above retrieves $E(t)$ directly, meaning it does so in non-iterative fashion. This gives it a great speed advantage over FROG. The problem remains, though, that generating identical pulses with sheared spectra is non-trivial. Figure 2.6 below shows a schematic of our lab’s SPIDER device, based on reference [57].

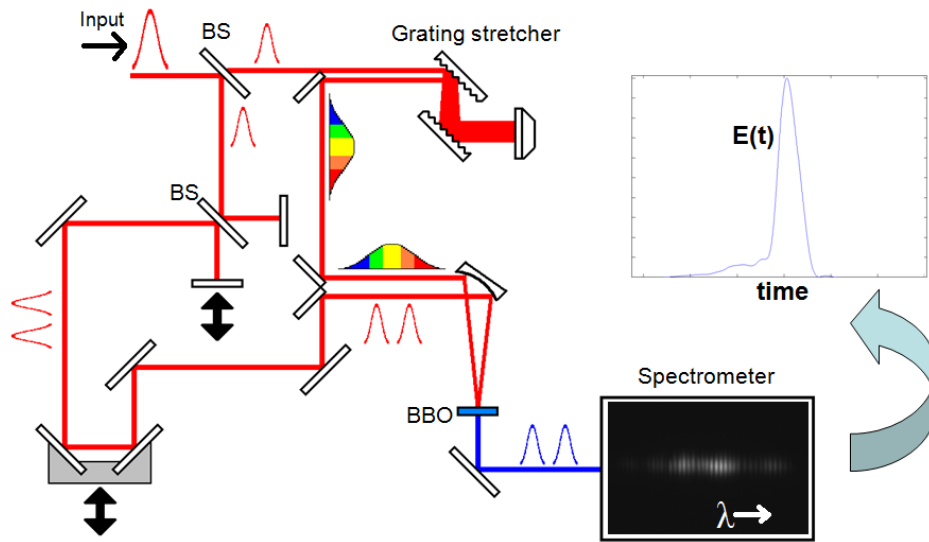


Figure 2.7: SPIDER apparatus, followed by sample interferogram and retrieved $|E(t)|$.

In the SPIDER setup above, the input pulse is initially split into two pulses. The first pulse is chirped about 200 times its initial length by a grating stretcher and has its polarization rotated by 90° . The other pulse is again split by a Michelson interferometer into two collinear, identical pulses, delayed by $\Delta\tau \approx 1$ ps. The Michelson pulses are combined with the chirped pulse with small angle in a 200 micron thick type-II phase matching BBO crystal. The pulse pair and the chirped pulse each make their own SHG signal, but a sum-frequency generated signal (SFG) also emanates from the BBO crystal in the direction of the sum of the input k-vectors. The SFG signal is the SPIDER signal that is sent to the spectrometer. The thickness of the crystal is chosen to provide maximum SFG production while minimizing dispersion of the Michelson pulses and walk-off due to the group velocity mismatch between the fundamental and SFG signal.

The SPIDER signal is created by SFG between each of the identical short pulses and the long, chirped pulse. The chirped pulse is long enough so that over the time duration of each short pulse, it can be considered quasi-monochromatic. The portion of

the chirped pulse that interacts with the first short pulse is quasi-monochromatic with frequency ω_1 and the portion that interacts with the second short pulse has frequency ω_2 . If the center frequency of the short pulses is ω_0 , the center frequency of each of the SFG pulses is $(\omega_0 + \omega_1)$ and $(\omega_0 + \omega_2)$. For the purpose of the SPIDER algorithm, $\omega_2 - \omega_1 = \Omega$, causing the center frequency of each pulse to be ω' and $\omega' + \Omega$.

Though the sheared pulses are different from the input pulse due to the large center frequency shift $\omega' = \omega_0 + \omega_1$, $\varphi(\omega)$ is still recoverable because it is preserved through SFG with a monochromatic signal, as is the shape of $|\tilde{E}(\omega)|$.

The sheared pulses then enter a spectrometer, and the SPIDER algorithm is performed on the spectrometer signal. The SPIDER apparatus and algorithm, as described above, only retrieve the spectral phase $\varphi(\omega)$ of the input pulse. The spectrum $|E(\omega)|$ must also be known. For small shear and smooth input spectrum, the spectrum is the square root of the DC term of the SPIDER spectrometer signal. Alternatively, the spectrum can be measured by a second spectrometer that operates synchronously with the SPIDER spectrometer. Figure 2.6 above shows a sample SPIDER spectrometer signal, as well as the final computed $\sqrt{I(t)}$.

Though the design of the SPIDER apparatus is complex, it operates in single-shot mode, does not require a large, smooth input transverse beam profile, and, with the appropriate data acquisition software, can display an accurately retrieved $I(t)$ in real time. In 1999, Iaconis and Walmsley's group demonstrated a SPIDER device that acquired and analyzed SPIDER traces at a repetition rate of 20 Hz [59]. We built our own SPIDER device that operates between 9 and 10 Hz. Our device sacrifices acquisition rate for the added functionality of synchronous triggering for multiple

devices—the SPIDER spectrometer, a second Ocean Optics fiber spectrometer which records the fundamental spectrum of the input pulse, and a digital oscilloscope that monitors the pulse energy incident on a photodiode. Since we simultaneously grab the fundamental spectrum of the input pulse along with the SPIDER trace, we increase the accuracy of retrieved $E(t)$, especially for pulses with spectra that are not very smoothly-varying. Synchronous measurement of the optical signal on the photodiode allows us to make energy-correlated measurements. Additionally, the spectrometer we use to acquire our SPIDER signal is an imaging spectrometer whose output is a CCD image (not array), increasing acquisition time but affording spatial resolution.

2.4.3 SPIDER for filamenting optical pulses

Femtosecond filamenting pulses are very broadband, have extremely complicated temporal structure, and, by their nature, do not have a smooth transverse beam profile. While our SSA and GRENOUILLE are sufficient for single-shot measurement of the direct ultrashort laser pulse output of our compressor, SPIDER is our only device that can measure $E(t)$ for the filamenting pulses we generate in our experiments. The SPIDER device that measures our filamenting pulses will be further discussed in Chapter Five.

Chapter 3: The Rotational Response of Atmospheric Constituents

3.1 Instantaneous versus rotational response of linear molecules

When an ultrashort pulse with sufficient intensity is incident on any molecule, the refractive index will nearly instantaneously change due to the nonlinear response of the very light, very fast bound electrons, according to Equation 1.1, reprinted here as a function of time, where $I(t)$ is the temporal intensity profile of the pulse:

$$n(t) = n_0 + n_2 I(t) \quad (3.1)$$

This simple equation does not take into account three major effects that may be pertinent to ultrafast laser-matter interactions: 1) anisotropy of the propagation medium, 2) ionization dynamics—any ionization will result in the presence of a plasma, which has its own refractive index, and 3) nuclear response—the optical radiation incident on the molecule can couple to molecular rotations and vibrations, each of which influences the refractive index of the medium in a time-dependent fashion.

Of the three processes mentioned above, 1) is clearly not pertinent to atmospheric propagation of single short pulses, and 2) is pertinent to filamentation, and has generally always been included in modeling of atmospheric filamentation. As far as 3) is concerned, vibrations excited in atmospheric constituents do not constitute a significant contribution to the nonlinear refractive index of atmospheric constituents. At room temperature T , the molecular vibrational states of O_2 and N_2 are in the ground state because $\Delta E_{vibrational} \gg k_B T$, where k_B is the Boltzmann constant. In general, if the incident laser's optical bandwidth is greater than the frequency spacing between Raman-active vibrational states, it will drive population between states. The increased bandwidth

of a filamenting pulse (caused by SPM and described in Chapter 1) is sufficient to noticeably excite some lower vibrational states, as Levis et al. showed in 2009 [60].

The rotational response of atmospheric components is, by contrast, a significant part of the total nonlinear response to high intensity optical excitation. A group of molecules, when aligned, will usually have a refractive index that is larger or smaller than that of the same group of molecules, randomly oriented. This is because the polarizability of any asymmetric molecule depends on its orientation. Typically, for a dumbbell-shaped molecule, if the molecule is aligned along the polarization direction of the incident light, its polarizability is slightly larger, so its refractive index is slightly higher. The opposite is true for such a molecule aligned perpendicularly to the incident polarization.

If the molecule is not aligned along or orthogonal to the incident polarization, the polarization anisotropy causes the induced dipole moment \mathbf{p} to point in a direction different than that of the electric field vector \mathbf{E} . Classically, the rotational potential energy $-\frac{1}{2}\mathbf{p} \cdot \mathbf{E}$ is minimized when the molecule is aligned, so the molecule will move to align in the applied field polarization direction, resulting in a time-varying rotational refractive index response. Any such rotational response can be described through the addition of a second term to Equation 3.1:

$$n(t) = n_0 + n_2 I(t) + \int_{-\infty}^{\infty} R(\tau) I(t - \tau) d\tau \quad (3.3)$$

The significance of the delayed refractive index contribution in the third term on the right hand side of Eq. 3.3 due to rotational response of N_2 and O_2 to an ultrashort pulse has been downplayed in the arena of filamentation as late as 2007 [7].

This chapter presents results showing that the rotational response of N₂ and O₂ in atmosphere is large enough and fast enough to not only significantly contribute to nonlinear self-focusing of ultrashort pulses, but that for pulses longer than ~40fs FWHM, it is the dominant physical process in the self-focusing of filamenting pulses.

3.2 The relationship of molecular alignment to the refractive index

The dielectric response to an electric field applied to a sample of gas molecules is:

$$\epsilon = n^2 = 1 + 4\pi N \langle \alpha \rangle_t. \quad (3.4)$$

Here, N is the number density (per cm³) and $\langle \alpha \rangle_t$ is the time-varying polarizability of the ensemble average of the molecules in the polarization direction of the incident electric field. We define the z axis is the axis of symmetry of a linear molecule, formed by the line that goes through all atoms in the molecule, and the x and y axes are perpendicular to each other and to z . We can now express the polarization anisotropy by specifying differing values of $\alpha_{||} = \alpha_{zz}$ and $\alpha_{\perp} = \alpha_{xx} = \alpha_{yy}$, the only nonzero components of the molecular polarizability tensor $\bar{\alpha}$. Typically, $\alpha_{||} > \alpha_{\perp}$. We now express the incident electric field as $\mathbf{E} = E \hat{\mathbf{e}} = E_x \hat{\mathbf{x}} + E_z \hat{\mathbf{z}}$, where $\hat{\mathbf{e}}$ is a unit vector in the direction of the electric field polarization and $\hat{\mathbf{y}}$ is the direction of propagation. We define $\langle \alpha \rangle_t$ with the aid of Einstein summation notation:

$$\langle \alpha \rangle_t = \langle \hat{\mathbf{e}} \cdot \bar{\alpha} \cdot \hat{\mathbf{e}} \rangle_t = \langle e_i \alpha_{ij} e_j \rangle_t = \langle e_x^2 \rangle_t \alpha_{xx} + \langle e_z^2 \rangle_t \alpha_{zz}. \quad (3.5)$$

Given θ as the angle between the molecular axis z and the polarization $\hat{\mathbf{e}}$ we write

$e_z = \hat{\mathbf{e}} \cdot \hat{\mathbf{z}} = \cos \theta$. Using that, and also $\Delta\alpha = \alpha_{||} - \alpha_{\perp}$, Equation 3.4 is re-written as

$$\epsilon = n^2 = 1 + 4\pi N (\Delta\alpha \langle \cos^2 \theta \rangle_t + \alpha_{\perp}), \quad (3.6)$$

where $\langle \cos^2 \theta \rangle_t$ expresses the degree of alignment of the molecule with reference to the electric field. In the absence of an aligning electric field, $\langle \cos^2 \theta \rangle_t = \frac{1}{3}$, which is equivalent to an average over the solid angle, so in the field-free case, $\epsilon = n_0^2$. From substituting into Equation 3.3, the third term describing the delayed response becomes:

$$\Delta n_{\text{rot}} = 2\pi N n_0^{-1} \Delta\alpha \left(\langle \cos^2 \theta \rangle_t - \frac{1}{3} \right). \quad (3.7)$$

The next section describes how optically-aligned $\langle \cos^2 \theta \rangle_t$ was measured initially, and how it can be calculated.

3.3 Quantum mechanical rigid rotor model of molecular alignment

3.3.1 Early measurement and modeling of optically-driven molecular alignment

In 1975, Lin et al. [61] found that a 5 ps long, 1.06 micron wavelength laser pulse rotationally aligned room-temperature CS₂ molecules in a vapor state. They measured the molecular alignment by probing the optically pumped vapor with a weak probe pulse polarized at 45° with respect to the pump pulse to sample the birefringence due to the alignment. They found that the time-dependent rotational behavior was not classical. The molecules quickly aligned with the pump laser pulse and de-aligned once the laser pulse was turned off, and then many picoseconds later, they spontaneously re-aligned. Lin et al. were able to explain this behavior when they theoretically computed the rotational response of linear molecules to short pulses of light [62], using the quantum mechanical rigid rotor model.

The time-dependent classical ensemble average alignment $\langle \cos^2 \theta \rangle_t$ in the presence of an electric field is calculated as

$$\langle \cos^2 \theta \rangle_t = \text{Tr}(\boldsymbol{\rho}(t) \otimes \cos^2 \theta) = \rho_{kl} \langle l | \cos^2 \theta | k \rangle, \quad (3.8)$$

where Tr is the trace operation, $\boldsymbol{\rho}(t)$ is the density matrix, \otimes denotes operator multiplication, and $\langle l |$ and $| k \rangle$ are bra and ket spherical harmonic eigenstates of the rotational field-free Hamiltonian. $| k \rangle = | j, m \rangle$ and $| l \rangle = | j', m' \rangle$, and the energy E_k is:

$$E_k = E_j = hcBj(j + 1). \quad (3.9)$$

j is the quantum number for total rotational angular momentum \mathbf{J} and m is the quantum number for the component of the angular momentum along the polarization direction of the electric field \mathbf{E} . B is the rotational constant of the molecule, which depends on its moment of inertia \mathbf{I} .

$$B = \frac{h}{8\pi^2 c \mathbf{I}}. \quad (3.10)$$

The density matrix is calculated to first-order in the optical perturbation $\boldsymbol{\rho}(t) = \boldsymbol{\rho}^{(0)} + \boldsymbol{\rho}^{(1)}(t)$, where $\boldsymbol{\rho}^{(1)}(t)$ is

$$[\boldsymbol{\rho}^{(1)}(t)]_{kl} = -\frac{i}{\hbar} \int_{-\infty}^t d\tau [\mathcal{H}(\tau), \boldsymbol{\rho}^{(0)}]_{kl} e^{(i\omega_{kl} + \gamma_{kl})(\tau - t)}, \quad (3.11)$$

the first order correction to the density matrix induced by the perturbation Hamiltonian $\mathcal{H} = -\frac{1}{2} \mathbf{p} \cdot \mathbf{E}$, and $\mathbf{p} = \bar{\boldsymbol{\alpha}} \cdot \mathbf{E}$ is the induced molecular dipole moment. $\mathbf{E}(\tau)$ is the electric field envelope whose peak is centered at time $\tau = 0$. The thermal equilibrium distribution of rotational eigenstates at $t = -\infty$ is described by the zeroeth order density matrix $\boldsymbol{\rho}^{(0)}$, and γ_{kl} is the dephasing frequency between states k and l . The perturbation Hamiltonian \mathcal{H} drives the molecular alignment.

The distinct energy states correspond to distinct possible angular frequencies $\omega_j = E_j/\hbar$. Each eigenstate evolves in time as $| j, m \rangle e^{-i\omega_j t}$. The frequency of rotation

is in the terahertz range. A linear-shaped molecule under zero applied electric field is in a superposition of these states, called a wavepacket:

$$|\psi\rangle = \sum_{j,m} a_{j,m} |j, m\rangle e^{-i(\omega_j t)}. \quad (3.12)$$

Lin et al. found that a short optical pulse had enough bandwidth to non-resonantly excite many rotational eigenstates of CS₂ simultaneously. Though the relative phase of the eigenstates (encoded in the complex amplitude $a_{j,m}$) is random in the field-free case, since the frequency of a rotational eigenstate is related to that of its neighbors by integer multiples of a constant—

$$\Delta\omega_{j,j+1} = \frac{E_{j+1} - E_j}{\hbar} = 2\pi cB(2j + 2) \quad (3.13)$$

—the optical pulse excites a coherent rotational wavepacket whose alignment in time evolves like a superposition of in-phase sinusoids. In the case of first-order perturbative optical excitation, the coherent bandwidth of the wavepacket is limited to either the bandwidth of the incident optical pulse $\Delta\omega_{\text{opt}}$ or the bandwidth of the thermal rotational distribution $\Delta\omega_{\text{rot}}$ —whichever is smaller.

Lin et al.’s experiment on transient birefringence indeed showed picosecond-scale alignment of CS₂ and subsequent de-alignment, followed by intervals of picosecond pulse-like alignment revivals at integer multiples, halves and quarters of the rotational revival period **T**:

$$\mathbf{T} = \frac{1}{2cB}. \quad (3.14)$$

In the case of CS₂, **T** = 152 ps.

Lin’s work opened up the door for chemists like Felker [63] to study Rotational Coherence Spectroscopy (RCS) of large gas-phase molecules with longer revival periods

than CS₂. Hartland et al. [64] measured alignment-induced vibronic fluorescence depletion to map out the revival structure of I₂ gas. They confirmed the revival period for the ground state rotational coherence of I₂ to be $\mathbf{T} = 443$ ps.

For N₂, $\mathbf{T} = 8.3$ ps. The highest rotational state j_{\max} of the thermal rotational distribution is:

$$j_{\max} \sim \frac{3}{4} \left(1 + \left(1 + \frac{8 k_B T}{9 B h c} \right)^{1/2} \right). \quad (3.15)$$

At room temperature, $k_B T / B h c \gg 1$ for N₂, so $j_{\max} \sim 20$. For large j_{\max} , the available bandwidth $\Delta\omega_{\text{rot}} \sim k_B T / \hbar \sim 4 \times 10^{13} \frac{\text{rad}}{\text{s}}$, which is the bandwidth of a ~ 160 fs transform-limited ultrashort pulse. This means that an ultrashort pulse can be expected to coherently excite the majority of the available bandwidth $\Delta\omega_{\text{rot}}$ of atmospheric N₂. In this case, the fast rise time to the peak initial alignment would be ~ 80 fs and the molecular alignment revivals would also have the same rise and fall time.

3.3.2 Measurement of quantum molecular alignment using spectral analysis

The fast rising and falling refractive index transients from molecular alignment due to an ultrashort pulse could impart cross-phase modulation on a weak probe pulse. The fast rising refractive index of molecules swinging into alignment would red-shift a probe pulse, and the fast falling index due to de-aligning molecules would cause a blue-shift. In 1997, Ripoche [65] irradiated a large volume of N₂ gas in a gas cell with a strong 800 nm wavelength pulse with 150 fs duration. They then nearly collinearly propagated a weak version of the same pulse through that volume (the pump/probe angle

was $<0.3^\circ$). They measured the red- or blue-shift of the probe spectrum versus pump/probe delay by computing the center-of-mass of the pump spectrum. Using a propagation model, they back-calculated the molecular alignment necessary to produce such spectral shifts and found the molecular rotational response was few-hundred femtosecond spikes of alignment, interspersed over longer periods of no discernible alignment. This result was identical to what was theoretically predicted by the quantum mechanical model.

One of the important results from Ripoche et al.'s work, and from subsequent work done by the same group [66] was in the comparison of instantaneous and delayed contributions to the nonlinear refractive response of gaseous molecules. They found that the peak refractive index due to the bound electronic response was similar in magnitude to the peak index caused by molecular alignment. They concluded that, for 150 fs duration optical pulses, the nonlinear refractive index had equal contributions from instantaneous and rotational molecular response.

3.4 Simulation of quantum molecular alignment of N₂ and O₂

Using the perturbation method briefly described in the previous section, we computed the quantum molecular alignment of the primary atmospheric constituents N₂ and O₂. The computational method we used is described in greater detail in reference [67].

Shown in Figure 3.1 are calculated plots of the molecular alignment versus time for nitrogen (3.1a and 3.1b) and oxygen (3.1c and 3.1d) gas irradiated by a 100 fs optical pulse whose peak intensity is at $t = 0$. Figures 3.1a and 3.1c highlight the revivals in

molecular alignment many picoseconds after the optical radiation is over. Figures 3.1b and 3.1d show the initial molecular response to the ultrafast pulse. The dashed line indicates $I(t)$ of the 100 fs pulse.

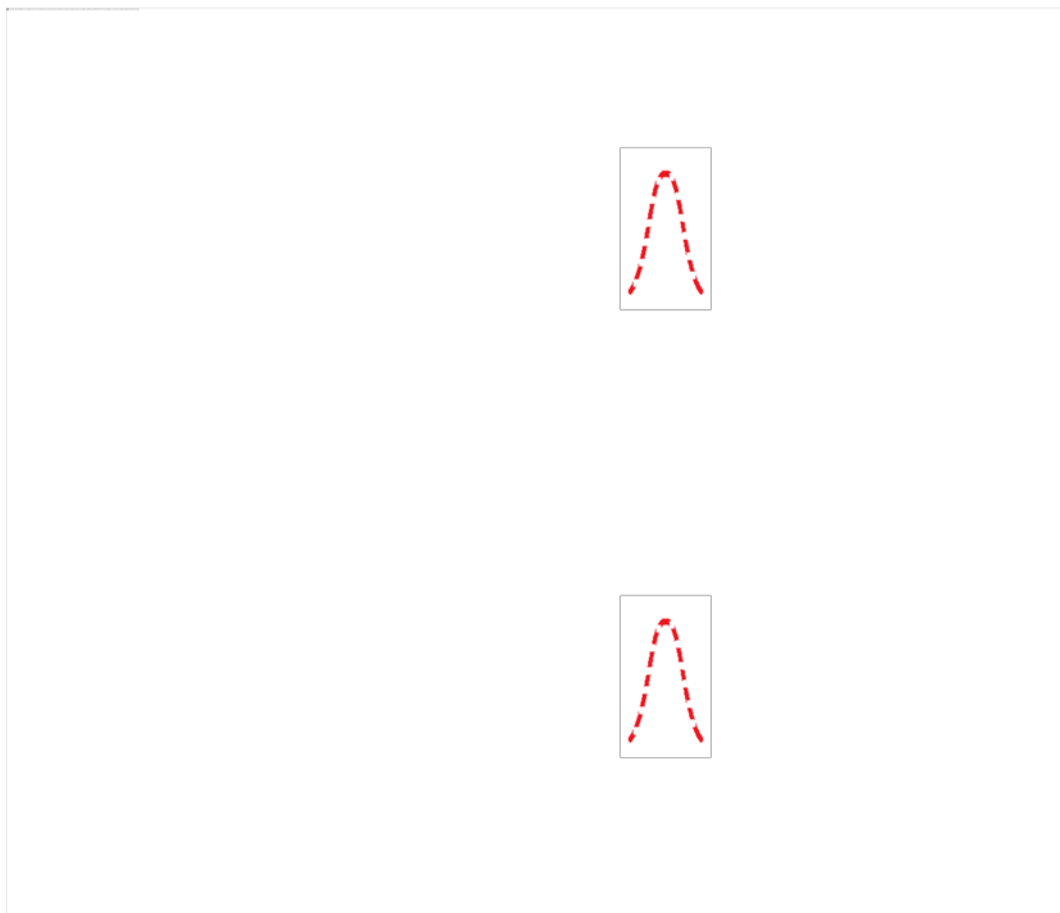


Figure 3.1: Calculated molecular alignment versus time for N_2 (top) and O_2 (bottom) gas due to a 100 fs pulse. The dashed line indicates the intensity of the optical excitation.

One important feature of Figures 3.1b and 3.1d is the very quick alignment of N_2 and O_2 . Within ~ 100 fs, the molecules have reached their peak alignment. This rapid alignment implies that in an experiment, a significant part of the tail of the pump pulse will experience self-focusing due to molecular alignment. The other, even more noticeable feature of the plot is the equally quick de-alignment and apparent dephasing of the molecules until nearly 2, 4, 6 and 8 picoseconds later, where there are similarly fast

pulses of molecular alignment. As explained earlier, molecular alignment revivals occur at integer multiples of $\frac{1}{4}$ of the fundamental rotational period $\mathbf{T} = 8.3$ picoseconds for N_2 and $\mathbf{T} = 11.6$ picoseconds for O_2 .

3.5 Inter-molecular collisions

The calculations of ultrashort-pulse-driven molecular alignment above predict alignment revivals that should continue indefinitely. In an experiment, elastic inter-molecular collisions dephase the rotational wavepacket, causing the amplitude of the alignment revivals to degrade over time. The alignment revival amplitude decreases to half its size in the collisional time $\tau_{\text{coll}} = \nu_{\text{coll}}^{-1}$. Using kinetic theory of gases, the collisional frequency ν_{coll} is calculated from the average molecular speed \bar{v} and the mean free path λ_m (average distance traveled by a molecule between collisions) [68]:

$$\nu_{\text{coll}} = \bar{v} * \lambda_m^{-1} = \sqrt{\frac{8k_B T}{\pi m}} * \sqrt{2} \pi d^2 N, \quad (3.16)$$

where m is the mass of the molecule, d is its diameter, and N is the gas density. N for air is $\sim 2.5 \times 10^{19} \text{ cm}^{-3}$. By approximating the composition of air to be 80% N_2 and 20% O_2 , the diameter of an air molecule is $\sim 0.3 \text{ nm}$ and its molar mass is 28.8 amu. $\bar{v} = 468 \frac{\text{m}}{\text{s}}$, $\lambda_m = 0.102 \mu\text{m}$, $\nu_{\text{coll}} \sim 4.6 * 10^9 \text{ Hz}$, and $\tau_{\text{coll}} \sim 217 \text{ ps}$.

This long collision time implies that many optically induced quantum molecular alignment revivals in atmosphere, which occur every few picoseconds, will be measurable before the coherence of the wavepacket deteriorates.

3.6 Direct space-and-time resolved measurement of delayed rotational response and quantum molecular alignment revivals

3.6.1 Measurement of molecular alignment using Coulomb explosion imaging

In the previous sections, two pump-probe methods to measure quantum molecular alignment were described: measurement of the birefringence of aligned molecules, and measurement of probe spectral modulation induced by XPM from the rotating molecules. Neither of these methods is spatially resolved, and the spectral measurement requires a propagation model to infer, rather than to directly measure alignment. Molecular alignment has been directly measured [69, 70] by Coulomb explosion imaging of a low-density gas in high vacuum chambers ($\sim 10^{-9}$ mbar). Microchannel plates are used to record the angular distribution of molecular fragments. This technique, like the others, does not have spatial resolution. Additionally, the low gas density results in a low signal level, so multi-shot averaging is necessary. All the above mentioned techniques require multiple shots to map out the refractive index transient due to molecular alignment, and their temporal resolution is limited to that of the ultrashort probe pulse, typically $> \sim 45$ fs.

3.6.2 Spectral interferometry

In 2002, Kim, Alexeev and Milchberg developed a single-shot method of probing ultrafast refractive index transients over a range of a few picoseconds with 10-fs time resolution [71]. The technique is called Single-shot Supercontinuum Spectral

Interferometry (SSSI). Spectral interferometry, also known as frequency-domain interferometry, had already been developed by Reynaud et al. in 1989 to measure self-phase modulation of a short pulse in an optical fiber [72] and by Tokunaga et al. in 1992 to measure cross-phase modulation in thin, optically transparent samples in [73]. In these cases, the researchers co-propagated a strong optical pump pulse with a weak probe pulse as the pump pulse applied some nonlinear phase shift to the probe in the interaction material. An identical but unperturbed copy of the probe pulse, called the reference pulse is then spectrally interfered (Eq. 2.12) with the probe. If the phase of the reference pulse is known, the difference between the reference phase and the phase recovered from the interference pattern yields the pump-induced phase modulation. Scanning the pump/probe delay and computing the phase at each delay point gives the full temporal profile of the pump-driven nonlinearity.

Tokunaga et al. [74] later used a linearly chirped probe pulse and found that the temporal evolution of the nonlinear refractive index shift roughly linearly mapped to the spectral axis. This result means that $\Phi(t) \sim \text{const} * \varphi(\omega)$; the induced fringe shift plotted versus frequency is roughly proportional to the phase shift over time. However, inferring the temporal refractive index profile from a linear frequency-to-time mapping is not fully accurate, because the uncertainty principle implies that any single color cannot occur at a single point in time. $\Phi(t)$ is instead computed using Takeda et al.'s Fourier transform technique [58] for spectral interferometry described in section 2.4. Spectral interferometry has since been used widely, for example, in the characterization of ultrashort pulses [57] and the measurement of the temporal profile of ionization fronts with 70 fs resolution [75].

3.6.3 SSSI

Still, spectral interferometry suffered from either poor time resolution or too small of a temporal window until Kim et al. [71] began to use a chirped supercontinuum (SC) pulse as the probe and reference. The continuum was generated by focusing a ~ 100 fs pulse in air and collecting and collimating part of the SC light to be used as a probe and reference. Figure 3.2 below shows a schematic of SSSI from [76]:

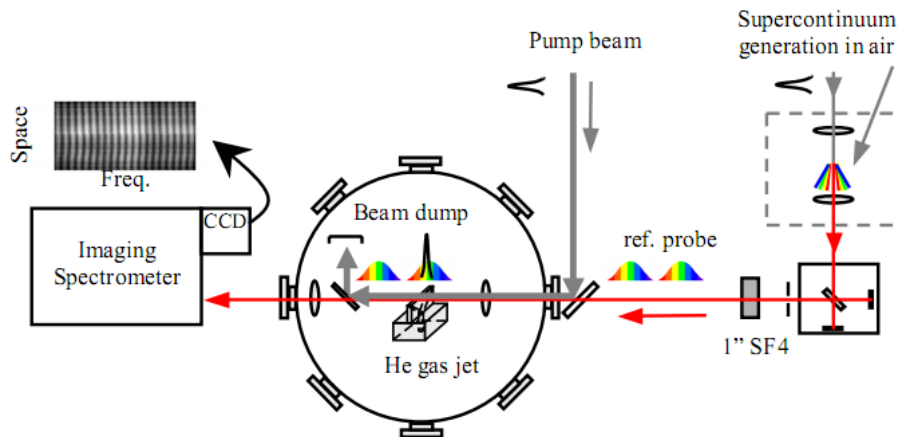


Figure 3.2: SSSI setup used to measure double-step ionization of Helium gas [76].

Once the SC is generated, it is split into two collinear copies, one delayed from the other by a few picoseconds. Then, they are heavily chirped to 2 ps duration in a dispersive medium. In this case the medium is a 1" thick piece of SF₄ glass, but other materials or a grating stretcher are also reasonable choices. The two chirped pulses are then collinearly combined with the pump pulse using a dichroic beamsplitter, with the probe pulse temporally overlapping the pump pulse and the reference pulse occurring 2 ps earlier. The three pulses propagate into the interaction region, where the pump pulse modulates the probe pulse through the nonlinear response. The pump light is filtered

away by a zero-degree 800 nm mirror, and the probe and reference pulses interfere in an imaging spectrometer, where the nonlinear process is time-resolved over the spectral axis. Because the interaction region is imaged onto the spectrometer entrance slit, the nonlinear process is spatially resolved over the axis defined by the slit. Kim et al. used SSSI to spatio-temporally resolve the double-step ionization of helium gas due to a 100 fs pump pulse [76] and to measure the time evolution of the explosion of femtosecond laser-irradiated clustered gases [77]. These nonlinear processes were time-resolved with 10 fs resolution over a 2 ps window. The calibration of the reference phase (dominated by linear chirp from the SF₄) is done by scanning the pump/probe delay in small steps and recording the spectral location of the peak pump-induced phase shift.

3.6.4 Xenon SSSI

More recently, we used an upgraded version of SSSI [78] to resolve the optically-induced alignment of several linear molecular gases, including N₂, O₂ and N₂O, and never-before seen alignment of D₂ and H₂ [67]. Our major improvement to SSSI was using a xenon-filled gas cell for generation of the supercontinuum pulse. Xenon has a lower ionization threshold than air, so broadband supercontinuum can be generated at significantly lower pump energy. As a result, an extremely broad supercontinuum could be generated (~100 nm full width, with a center wavelength near 700 nm) with a 100 fs, 800 nm, 400 μJ pulse, which was easily created by a very stable kilohertz regenerative amplifier. The great stability of the SC spectrum allowed us to do something Kim et al. were not able to do previously: average raw spectral interferograms. Averaging 200 SSSI interferograms reduced the phase noise floor from 0.1 to 0.01 radians. Figure 3.3 is a

schematic of our setup for xenon SSSI for the measurement of alignment of linear gas molecules.

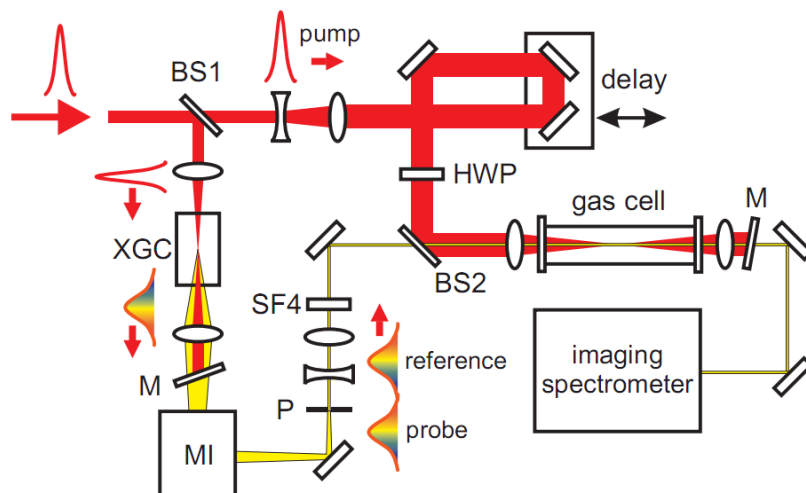


Figure 3.3: Xenon SSSI. BS1: beamsplitter, XGC: xenon gas cell, MI: Michelson interferometer, P: 500 μm pinhole, SF4: 2.5-cm thick SF4 glass as dispersive material, HWP: half waveplate, M: zero degree Ti:Sapphire dielectric mirror, BS2: beamsplitter for combining pump and SC pulses.

This setup is similar to that from Figure 3.2, except that the gas jet is replaced with a 40 cm long cylindrical gas cell, which was filled with various gas species at different pressures. The pump, reference and probe pulses were focused with a 40-cm focal length lens into the gas cell. The distance over which the strong pump pulse interacted with the weak probe was approximately 5.6 mm—twice the Rayleigh length of the pump pulse. The end of the interaction region was imaged with 6.9X magnification onto the entrance slit of the imaging spectrometer.

3.6.5 Measurement of rotational wavepackets of N_2O , N_2 and O_2

Figure 3.4 below is a plot of the raw SSSI interferogram resulting from the nonlinear response of N_2O gas to a 100 fs pulse. The peak of the optical pulse is at $t = 0$, and the phase disturbance on the probe is due to the fast nonlinear response of bound

electrons and the delayed rotational motion of the N_2O molecule. The spectral axis, which from left to right changes from red to blue, also roughly corresponds to time moving from 1 ps before the disturbance to 1 ps afterwards. The phase disturbance is much longer than 100 fs, showing how much the molecular alignment affects the total initial nonlinear response. Additionally, the spatial dependence in the vertical direction shows us that the pump pulse focal region diameter is much smaller than 250 microns.

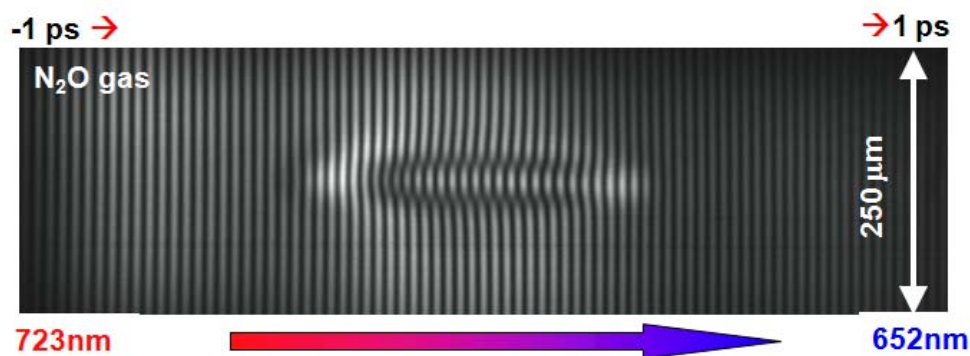


Figure 3.4: Raw SSSI Interferogram showing the initial nonlinear response of N_2O to a 100fs pulse.

SSSI is also ideal for measuring the fast bursts of molecular alignment revivals following the initial nonlinear response of a linear gas molecule to an ultrashort pulse. The probe pulse must be delayed to the time at which the re-alignment occurs, and the reference pulse, which is ~ 2 ps earlier than the probe, should occur at a time when there is certainly no alignment transient.

SSSI can measure the initial response, plus the $\frac{1}{4}$, $\frac{1}{2}$, $\frac{3}{4}$ and full revivals of N_2 alignment in five single measurements. Figures 3.5 and 3.6 show the spatio-temporal molecular alignment transients of N_2 and O_2 gas measured by SSSI, side by side with the alignment predicted by the computational technique described in [67].

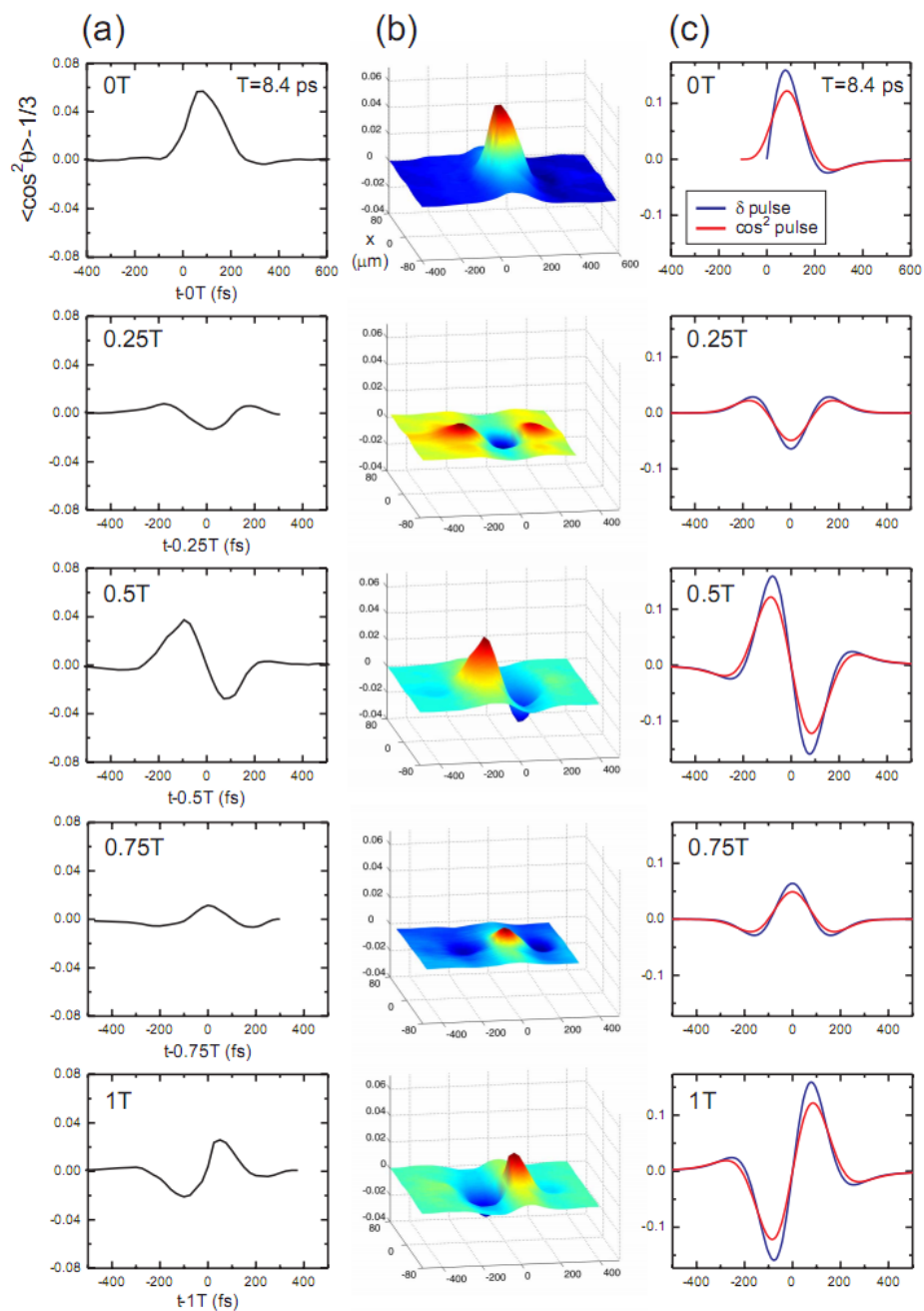


Figure 3.5: a) Axial alignment of N_2 measured by SSSI, b) SSSI space-resolved alignment, and c) theoretically computed molecular alignment for comparison with a).

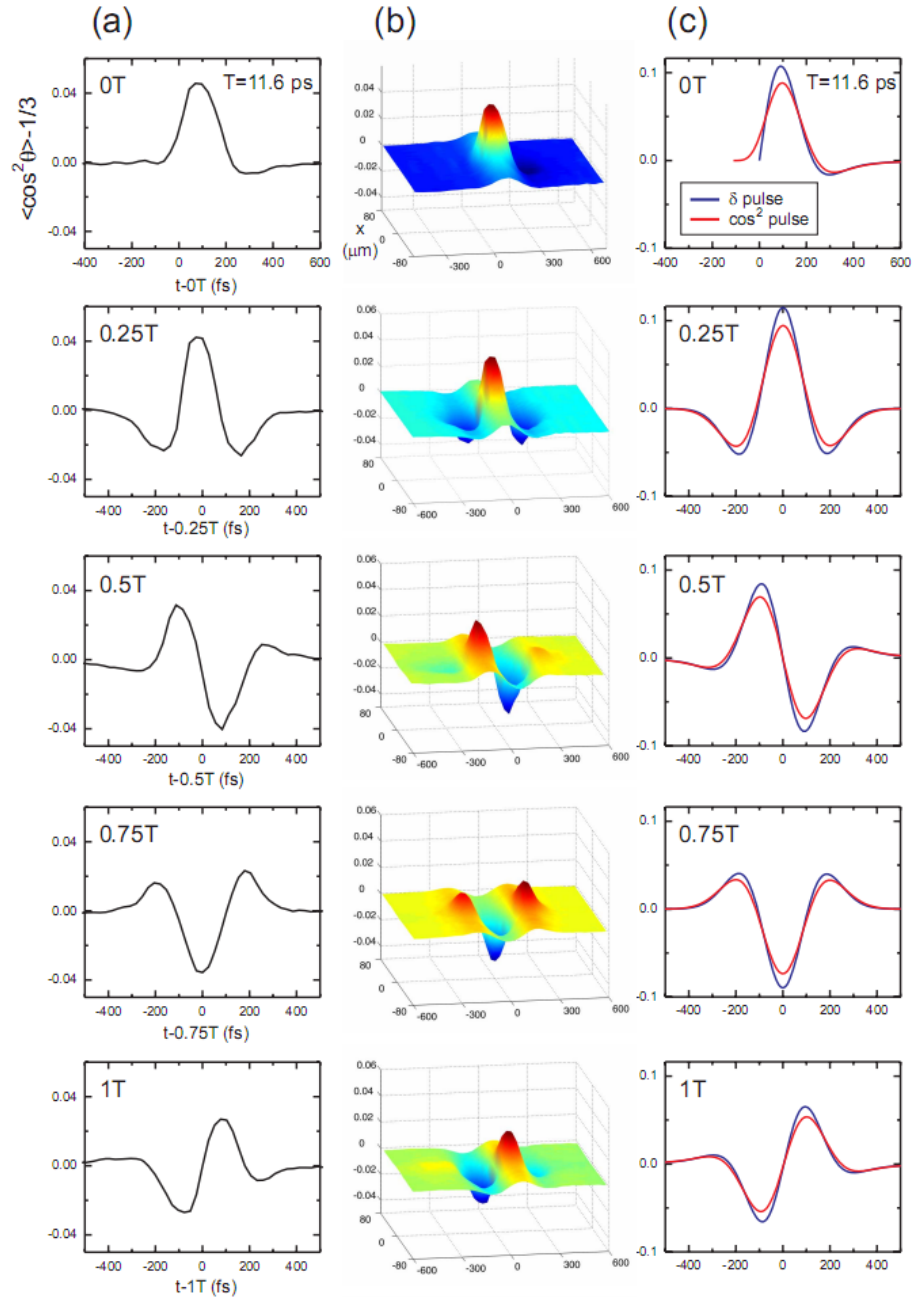


Figure 3.6: a) Axial alignment of O₂ measured by SSSI, b) SSSI space-resolved alignment, and c) theoretically computed molecular alignment for comparison with a).

SSSI faithfully recovers the temporal refractive index transient due to the irradiation of a linear molecule with an ultrashort pulse. The technique does, however, have some limitations with respect to the upper limit of pump intensity that can be used to drive molecular alignment. If the pump pulse is bright enough, it will generate

supercontinuum in the gas cell, which will propagate through the dichroic splitter and interfere with the reference and probe spectra. Also, for high enough pump intensity, the pump pulse will not only drive coherence between constituent states of the wavepacket of the gas molecules, but will also transfer the population among those states. This process results in a quasi-steady molecular alignment immediately after the initial molecular alignment spike, and was observed by Corkum et al. in 2003 [79]. The rotational revivals then appear as AC perturbations on top of the quasi-steady alignment. If the pump pulse is bright enough to drive population transfer and the probe pulse is parked over an alignment revival, both probe and reference pulses will overlap with effectively DC aligned molecules, rendering the fast alignment but missing the semi-permanent alignment.

3.7 Relevance of rotational response of N_2 and O_2 to atmospheric filamentation

Figure 3.7 below shows a more detailed view of the initial response of N_2 gas (circles) to a 100 fs pump pulse, as measured by SSSI. For comparison, the pump envelope (dots) and calculated molecular alignment (line) are shown.

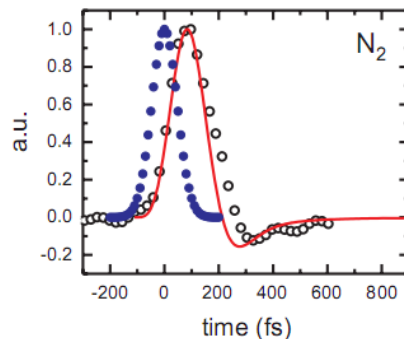


Figure 3.7: Initial response of N_2 gas to a 100 fs pump pulse, as measured by SSSI (circles), intensity envelope of the pump pulse (dots), and calculated molecular alignment (line).

The above figure shows a very different picture of the nonlinear response of N_2 than that measured by Ripoche et al. [65], who found that the nonlinear response of N_2 to a 150fs pulse had equal contributions from the prompt electronic response and the delayed rotational response. Although our SSSI measurement shows the combined effect of the instantaneous Kerr effect and delayed rotational alignment, its shape is almost perfectly replicated by our calculated molecular alignment, which does not include the instantaneous Kerr effect. The fast rotational alignment of N_2 dominates the prompt electronic response.

This observation has deep consequences for the understanding of filamentation of ultrashort pulses in atmosphere. Our SSSI measurement leads us to believe that quantum rotational alignment is the dominant self-focusing effect for pulses ~ 100 fs in atmosphere; the front end of the pulse aligns N_2 and O_2 , and the middle and tail end experience the focusing effects from those quickly aligned molecules. These results led us to conjecture that if we could actively control the state of molecular alignment, we would be able to strongly control filamentation. The following chapter will describe the first experiments we did to control the filamentary process using quantum molecular alignment revivals of N_2 and O_2 in atmosphere.

Chapter 4: Trapping, Enhancement and Destruction of an Optical/plasma Filament in a Quantum Molecular Alignment Wake

4.1 The critical power for self-focusing in air

4.1.1 Derivation of P_{cr}

As mentioned in the previous chapter, the dominance of the quantum rotational alignment wake over the bound instantaneous response of air constituents in the self-focusing a filamenting ultrashort pulse is often overlooked. We will elucidate this issue by discussing the critical power for self-focusing, P_{cr} .

P_{cr} is the power required for nonlinear self-focusing to compensate diffraction. The half-angle of diffraction for a Gaussian beam θ_{diff} is, for propagation distances much greater than the Rayleigh length:

$$\theta_{diff} \sim \frac{2\lambda_0}{\pi d n_0}, \quad (4.1)$$

where d is twice the $1/e$ beam waist and λ_0 is the vacuum wavelength. The convergence half-angle for nonlinear self-focusing θ_{sf} is expressed through the use of Fermat's principle of least time; the optical path length traveled by the center ray l_{center} to the focal spot z_{sf} must equal the path length traveled to the same point by an outer ray that experiences the minimal nonlinear refractive index l_{outer} [1]:

$$l_{center} = z_{sf}(n_0 + n_2(I)) = l_{outer} = \frac{z_{sf}n_0}{\cos(\theta_{sf})} \sim \frac{z_{sf}n_0}{1 - \frac{1}{2}\theta_{sf}^2}, \quad (4.2)$$

where $\cos(\theta_{sf})$ is expanded for small θ_{sf} . Solving Eq. 4.2 for θ_{sf} gives:

$$\theta_{\text{sf}} \sim \sqrt{\frac{2n_2 I}{n_0}}. \quad (4.3)$$

For the condition that self-focusing compensates diffraction, we set Equations 4.1 and 4.3 equal to one another. Assuming that the total power in a beam $P = \frac{I}{\pi d^2/4}$, we get:

$$P_{\text{cr}} \sim \frac{\lambda_0^2}{2\pi n_0 n_2}. \quad (4.4)$$

The above expression only slightly differs from Eq. 1.7, $P_{\text{cr}} = 3.77\lambda_0^2/8\pi n_0 n_2$, which Fibich and Gaeta [8] calculated for a beam with a transversely Gaussian intensity profile. Note that although the maximum instantaneous nonlinear refractive index a pulse can experience depends on its intensity, the resultant focusing power also depends on the magnitude of the refractive index gradient. Since self-focusing due to the instantaneous Kerr nonlinearity is directly proportional to a pulse's intensity and inversely proportional to its spot size, power, and not intensity, is the critical property.

4.1.2 Experimental measurement of P_{cr}

The nonlinear refractive index of air was measured with long pulse, high power lasers as early as 1989 by Shimoji et al. [9] and Pennington et al [80]. By substituting the measured n_2 into Equation 1.4, they predicted $P_{\text{cr}} \sim 1.8$ GW. However, many researchers doing filamentation experiments with ultrashort pulses have since reported critical powers in the range 5-10 GW [6, 7]. This power is significantly higher than predicted, but very few groups took the time to examine the discrepancy. Liu and Chin in 2005 [81] did vary their input power by maintaining a constant pulse energy and varying pulse length from 42 fs to 800 fs by adjusting their chirped pulse amplification compressor.

They focused the pulse in air and inferred P_{cr} from the decrease in focal length as a function of pulse power. In this way, they found that the measured P_{cr} dropped from 10 GW to ~ 5 GW when the pulse length changed from 42 fs to 200 fs FWHM, regardless of chirp. They pointed to Ripoche et al.'s measurement [65] that roughly predicted a doubling of the nonlinear refractive index (and therefore halving of P_{cr}) due to rotational alignment of atmospheric N_2 and O_2 , but did not model or pursue the issue further.

Our direct measurement of the molecular response of N_2 and O_2 [67], discussed in detail in the previous chapter, allowed us to directly measure the time-dependent nonlinear response to a focused 110 fs optical pulse of the two major atmospheric constituents at room temperature and 1 atm pressure. The fact that the calculated molecular alignment almost completely predicted the experimentally-measured total response highlighted the dominance of the rotational versus instantaneous contribution to the refractive index perturbation.

The experimentally measured refractive index bump near $t=0$ (the peak of $I(t)$) for N_2 and O_2 , shown in Figures 3.1b and 3.1d, including both instantaneous Kerr and delayed molecular alignment effects, were used to synthesize the nonlinear response of air (80% N_2 and 20% O_2). The air response curve is pictured below, along with a plot of $I(t)$ for the pump pulse.

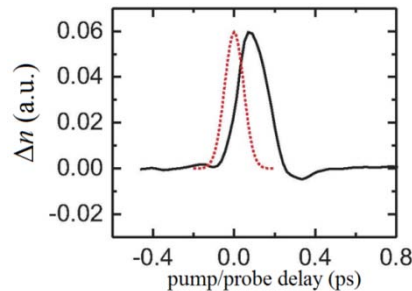


Figure 4.1: Experimental measurement of air refractive index change near $t=0$ (black line), synthesized from SSSI measurement of molecular alignment of N_2 and O_2 , compared with the pump pulse $I(t)$ (red dotted line).

We use our measurement of the total nonlinear response of air in Figure 4.1 to predict P_{cr} for filamenting 100 fs pulses in atmosphere. We approximate n_2 using the refractive index shift at the peak of the laser intensity: $n_2 \approx \frac{\Delta n_{t=0}}{I(t=0)}$. Using this value, we find that $P_{cr} \approx 10$ GW. At the peak molecular alignment, $P_{cr} \approx 4.3$ GW. Both of these values are very close to the P_{cr} that has been experimentally measured by the scientific community for short and long pulses. This fact lends credence to our statement that rotational alignment is the dominant self-focusing nonlinearity for >40 fs pulses. The refractive index response time δt due to molecular orientation alone is [10]:

$$\delta t \sim \frac{2\mathbf{T}}{j_{max}(j_{max} + 1)}. \quad (4.5)$$

For N_2 , $\mathbf{T} = 8.3$ ps is the rotational revival period (Eq. 3.13) and $j_{max} = 20$ is the highest rotational state (Eq. 3.14), giving $\delta t \sim 40$ fs. This means that unless a pulse is shorter than ~ 40 fs, the rotational response of air is the dominant nonlinearity.

4.2 Filament enhancement experimental concept

The periodic revivals of aligned N_2 and O_2 were nearly as large in magnitude as the initial response and travel behind a filamenting pulse at the same group velocity as the pulse. In a very real sense, behind every ultrafast filamenting pulse is a delayed wake of periodically-spaced lenses, each with almost the same self-lensing power as the initial response and the same time duration as a ~ 100 fs FWHM optical pulse. Our idea was to send a *second*, collinear, delayed “probe” filamenting pulse into one of those molecular lenses in the alignment wake of a pump filament, with the thought that the probe would

experience an enhanced focusing effect, leaving behind a longer and/or more axially dense plasma filament.

In order for us to do this experiment, we had to determine the best temporal delay at which to inject the probe pulse. For that, we had to know the full temporal structure of the rotational response of air to the pump filament. Armed with the SSSI alignment data for N_2 and O_2 , we constructed the full space and time response of air to an ultrafast pulse for up to 12 ps after the pulse, in the same way that we synthesized Figure 4.1. Figure 4.2 below shows the result:

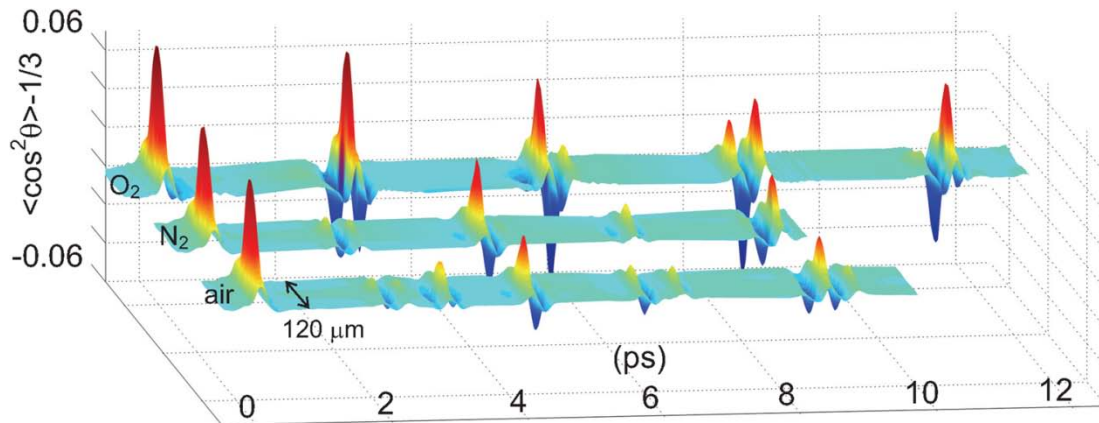


Figure 4.2: Measured alignment of 1 atm N_2 and O_2 at room temperature by a 110fs, 800 nm, $4.1 \times 10^{13} \text{ W/cm}^2$ laser pulse. The effective alignment of air is synthesized from the N_2 and O_2 plots.

One very pronounced feature in the synthesized spatio-temporal alignment response of air is the fast oscillating negative to positive to negative alignment near the full revival of N_2 and the $3/4$ revival of O_2 , near 8.3 ps pump/probe delay. This delay is an ideal one at which to seat our probe pulse; because the alignment peak is comprised of both aligned N_2 and O_2 , the lensing effects on a probe pulse would be greater at this delay than elsewhere.

In order to predict how significantly the pump-induced quantum molecular revival would lens the probe pulse, we estimate the magnitude of the effect using an argument similar to the one made to compute P_{cr} . For a Gaussian beam propagating one Rayleigh length z_0 away from its waist, the difference in phase acquired by the center of the beam and the waist is approximately 1 radian. If on the central axis there were a central refractive index bump Δn , then over the same propagation distance z_0 , the center of the beam would have its phase retarded by $k\Delta n z_0$, where $k = \frac{\omega n_0}{c} = \frac{2\pi}{\lambda}$, the optical wavenumber in air. If the phase retardation induced by the on-axis fractional increase in refractive index negates the natural phase advancement of the center of the beam, it will compete with diffraction and therefore assist self-focusing. So Δn will aid filamentation of the probe pulse if:

$$\Delta n > \sim (kz_0)^{-1}. \quad (4.6)$$

Now we predict the on-axis Δn a probe pulse would see ~ 8.3 ps after a pump filament aligns atmospheric N_2 and O_2 . Using our SSSI measurement of the molecular alignment of air, we found that at that delay, the maximum effective alignment $\langle \cos^2 \theta \rangle_{\text{eff}} - \frac{1}{3} \sim 0.025$. Using Equation 3.6, we find $\text{N}_2(\Delta\alpha = 0.93 \times 10^{-24} \text{ cm}^3)$ and $\text{O}_2(\Delta\alpha = 1.14 \times 10^{-24} \text{ cm}^3)$ [82] with that degree of alignment would give $\Delta n \sim 3 \times 10^{-6}$. We estimate the beam waist $w_0 \sim 100 \mu\text{m}$, and calculate z_0 and find that $(kz_0)^{-1} \sim 3 \times 10^{-6}$.

It is important to keep in mind that w_0 and z_0 for our probe filament will depend on any focusing geometry introduced in a filamentation experiment. We expected to weakly focus our pump and probe filaments to encourage quick filamentation along our small laboratory space (several meters of atmospheric propagation), so we needed to

make sure that diffraction due to our focal geometry will not overcome the molecular focusing effect. The f-number $f_{\#} = f/\text{NA}$, where f is the focal length and NA is the diameter of the beam. In the limit of long focal length, $f_{\#}$ can be put in terms of k and z_0 using the relation:

$$f_{\#} = \frac{kw_0}{4} = \frac{1}{2} \sqrt{\frac{z_0 k}{2}}. \quad (4.7)$$

Using Equation 4.2, the condition for lensing of the probe filamenting pulse due to the index perturbation of molecular pre-alignment in Equation 4.1 becomes:

$$f_{\#} > \sim \frac{1}{2} \sqrt{\frac{1}{2\Delta n}} \sim 200. \quad (4.8)$$

Therefore, we needed to be careful to launch our filamenting pulses with $f_{\#} > 200$.

One more important thing to note is that in the experimental implementation of the above concept, the probe and pump filamenting pulses will be perpendicularly polarized. This is necessary so that the probe may be separated by a polarizing beamsplitter and analyzed independently from the pump. We define the pump polarization as \hat{z} , the probe is polarized in \hat{x} , the propagation direction is \hat{y} , θ is the angle between the molecular axis and \hat{z} , and φ is the angle between the projection of the molecular axis on the x - y plane and \hat{x} . The alignment with respect to \hat{z} is $\langle \cos^2 \theta \rangle_t$, and the alignment with respect to \hat{x} is $\langle \sin^2 \theta \rangle_t \langle \cos^2 \varphi \rangle_t$. Because the aligning pulse is polarized in \hat{z} , the molecular alignment has no φ dependence, and $\langle \cos^2 \varphi \rangle_t = \langle \sin^2 \varphi \rangle_t = 1/2$. Additionally, $\langle \sin^2 \theta \rangle_t = 1 - \langle \cos^2 \theta \rangle_t$. As a result, the pump-induced molecular alignment in the polarization direction of the probe pulse is $(1 - \langle \cos^2 \theta \rangle_t)/2$. Pump-induced molecular alignment viewed by a perpendicularly polarized

probe pulse is half the magnitude and opposite in sign of the alignment it would see if its polarization were parallel to the pump.

4.3 Experimental setup

There are two major steps involved in the implementation of the experimental concept described in the previous section. The first is the generation of collinear pump and probe filamenting pulses. The second is the separation of the probe filament light from the pump and a diagnostic to measure the effect of pump-aligned molecules on the probe filament. Figure 4.3 shows the experimental setup.

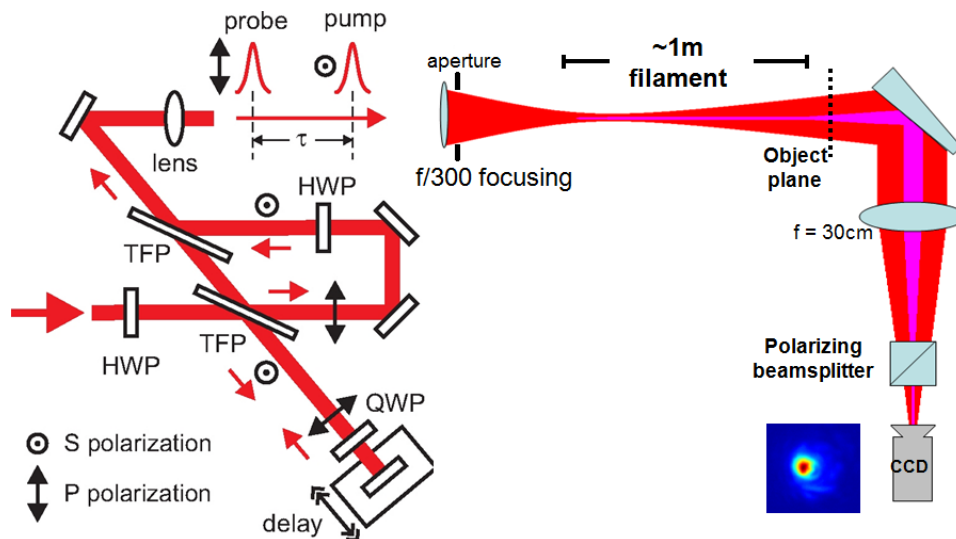


Figure 4.3: Dual-polarization interferometer (DPI) and probe filament end mode imaging setup.

We developed the dual-polarization interferometer (DPI) to split the amplified ultrashort pulse that exits from our compressor into the pump and probe filaments. The pulse initially enters the DPI through a half-wave plate and encounters the first of two thin-film polarizers (TFPs). The vertically-polarized part of the input pulse reflects off the first TFP through a quarter-wave plate and onto a retro-reflecting mirror on a delay

rail driven by a Newport CMA-25CCCL stepper motor actuator. The double pass through the quarter-wave plate rotates the polarization 90° , so when it encounters the first TFP again, it passes through it, and through a second TFP. On the other hand, the horizontally-polarized part of the input pulse transmits through the first TFP, reflects off two 45° mirrors and then through another half-wave plate, to get 90° polarization rotation. The now vertically-polarized second pulse encounters the second TFP and reflects off it on a path collinear with the first pulse.

The first half-wave plate allows us to arbitrarily split the input energy between the two pulses, and the quarter-wave plate and the second half-wave plate make it straightforward to tune the energy of the pump and probe independently of each other. Also, the DPI transmits nearly 100% of the energy of the input pulse to the experiment, while typical Mach-Zender and Michelson interferometers always dump 50% of the input energy.

Once the vertically polarized pump and horizontally polarized probe pulses collinearly leave the TFP, they enter a 3 meter focal length lens immediately followed by a hard adjustable aperture set to roughly 1 cm diameter. This gives the focal geometry $f_{\#} \sim 300$, which sufficiently fulfills the condition in Equation 4.8. An advantage of using a hard aperture in the beam prior to filamentation is that it generates a far-field diffraction pattern that is radially symmetric with a hot spot in the center, promoting on-axis filamentation. Without the hard aperture, the location of the filament may not necessarily be in the center of the beam, and may not be that stable. In order to verify that the hard aperture would not drastically change the plasma filament, we used WAKE, a 2-D simulation code developed by Mora and Antonsen [83], to simulate filamentary

propagation of two 6 mJ, 65 fs pulses launched with the above experimental geometry, one with a Gaussian transverse profile and one with a flat-top profile. In Figure 4.4, we plot the density and radius of the filaments.

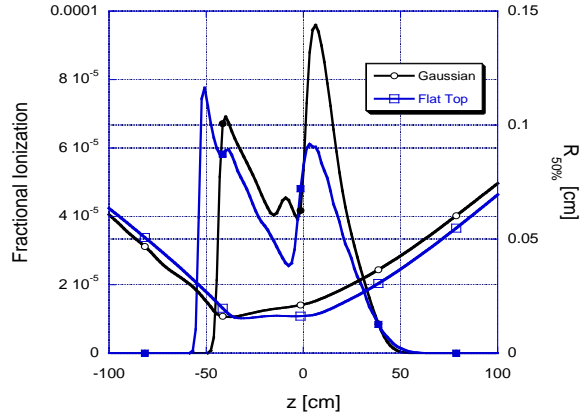


Figure 4.4: 2D WAKE simulation results showing plasma density (solid markers) and radius (hollow markers) of two 65 fs, 6 mJ pulses launched with $f_{\#} \sim 300$ and filamenting in atmosphere. Black-Gaussian transverse profile, blue-flat top profile.

We see that the hard aperture does not significantly change the filament plasma density or diameter, but the flat-top pulse collapses ~ 10 cm earlier than the Gaussian pulse.

At the exit of the 3 meter focusing lens, the pump and probe pulses were 130 fs FWHM intensity, measured by the GRENOUILLE described in Section 2.3. The pulses typically begin to filament 2.5 to 3 meters after passing through the 3 m lens. The plasma filaments are ~ 1 m long. The length of the plasma filament was not measured in this experiment, and the fluorescence of the filament was only visible to the naked eye for ~ 20 cm. However, the experiment which will be described in the following chapter confirms the length of the plasma for the parameters in this chapter.

Once the filaments end, the pump and probe pulses defocus for 1.5 meters and enter a single-lens beam mode imaging system. The first optics in the imaging system are two glass wedges which attenuate the pump and probe pulses. After reflecting off

both wedges, the light passes through a 30 cm focal length lens that images the filamenting pulse onto a digital camera. Just before the camera are a few neutral density (ND) filters to further attenuate the light, and a broadband polarizing cube beamsplitter to split off the vertically polarized pump pulse and allow only the probe filament to be imaged on the camera. The camera is positioned 39.5 cm after the imaging lens, so that the object plane is 1.25 m before the lens. The probe pulse is therefore imaged roughly 1.5 meters after it has stopped filamenting, with a magnification factor $M=0.32$. In order to measure the probe pulse spectrum, the digital camera is replaced with an Oceanoptics USB4000 fiber spectrometer with wavelength range $\sim 700\text{-}900$ nm.

In a typical run of the experiment, the pump and probe pulses will be carefully aligned across the room through pre-set apertures. Then, the probe beam delay line is set so that the pump/probe delay τ is in the region of initial molecular alignment ($\tau \approx 0$) or near the full quantum rotational revival of N_2 ($\tau \approx 8.3$ ps). The stepper motor then scans the probe in small steps—typically 5 microns per step—for an effective time delay step size of 33 fs. At each delay step, thirty CCD images of the probe filament are taken, as well as 100 consecutive spectra. Later, the images and the spectra are averaged.

4.4 Results and Discussion

4.4.1 Probe filament enhancement and destruction near $\tau \approx 0$

We saw the large effect of molecular alignment on the probe pulse both at pump/probe delay near $\tau \approx 0$ and $\tau \approx 8.3$ ps. First, we show the probe filament profile near $\tau \approx 0$, in Figure 4.5.

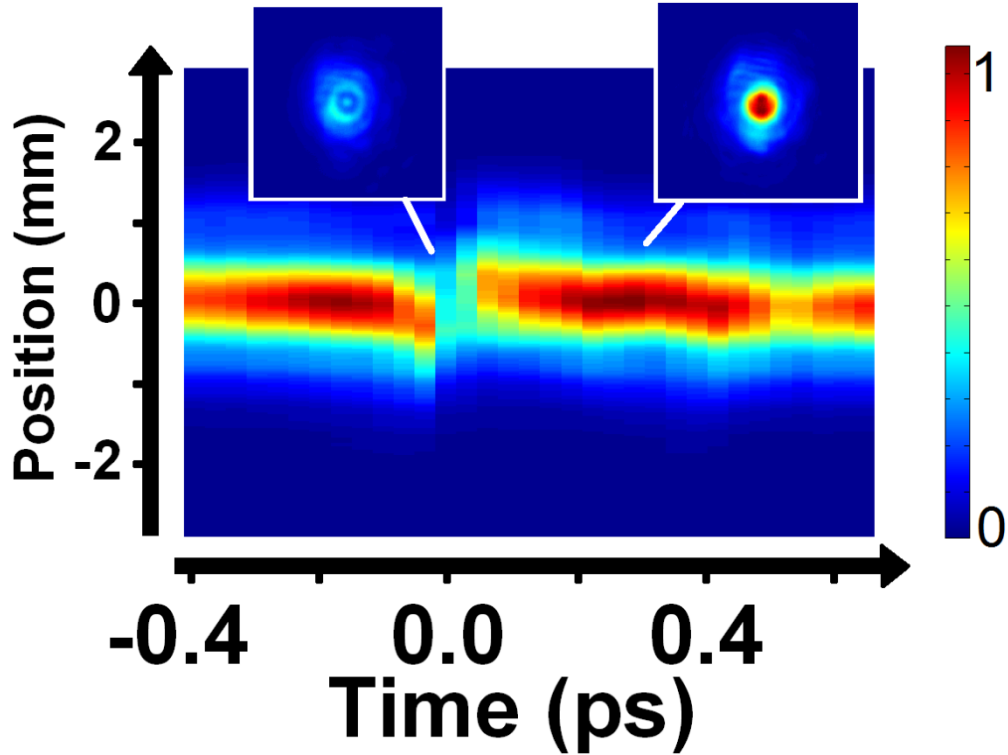


Figure 4.5: 1-D slices of the probe filament image v. pump/probe delay near $\tau \approx 0$.

Rather than show each 2-D image of the probe pulse for every pump/probe delay we used, we display the data by taking a 1-D line-out of the center of the probe pulse image and plotting it versus delay. The line-out is the average of a 10-pixel strip in the center of the 2-D image. The colormap is linear. 2-D images of the probe filament at certain delays are shown as insets in the plot. This format for displaying the delay-varying probe filament profile will be repeated for the duration of this chapter.

In Figure 4.5, the pump filament is 1.4 mJ ($1.1 P_{cr}$, using $P_{cr} = 10$ GW) and the probe filament is 2 mJ ($1.5 P_{cr}$). Both are 130 fs. Well before $\tau = 0$, the probe image shows a bright spot in the center of the beam, indicating a strong filament. As the delay nears $\tau = 0$, the probe filament intensity rises and then very noticeably at $\tau \sim 50$ fs, the bright center of the filament is abruptly destroyed and smeared over the beam profile (this corresponds to the 2-D image in inset A).

The initial rise and subsequent drop in axial intensity is easily explained. The rise in probe intensity near $\tau = 0$ corresponds to an additional lensing effect from the Kerr effect of the pump pulse. The Kerr effect always has a positive sign, though for a perpendicularly polarized probe, the effect has half the magnitude that it would for a probe pulse with parallel polarization. The later destruction of the probe filament is a result of strongly aligned N_2 and O_2 in the wake of the pump pulse, at a pump/probe delay of ~ 100 fs. Because the pump and probe are perpendicularly polarized, the aligned molecules left by the pump pulse will be seen as anti-aligned by the probe pulse. In this case, the molecular effect will be a drop in the on-axis refractive index, and negative lensing of the probe pulse. The negative lensing effect is so strong that it refracts the probe pulse and does not allow it to continue to filament.

But at even later pump/probe delays, the probe filament comes back (this corresponds to the 2-D image in inset B). This means that the molecular alignment is large and short-lived—roughly 100 fs—and corresponds very closely with the transient response measured by SSSI and shown in Figure 4.1.

Figure 4.6 below shows the same experiment as above, repeated with more energetic pump and probe filaments, but with time duration 330fs. The pump filament is 5.85 mJ ($3.7 P_{cr}$) and the probe filament is 7.25 mJ ($4.6 P_{cr}$). The pump/probe delay was adjusted in 85fs steps. The effect on the probe filament is similar to that from the 130fs case, but the delay range over which the probe filament is destroyed is longer. This is expected because the pump pulse is longer in duration.

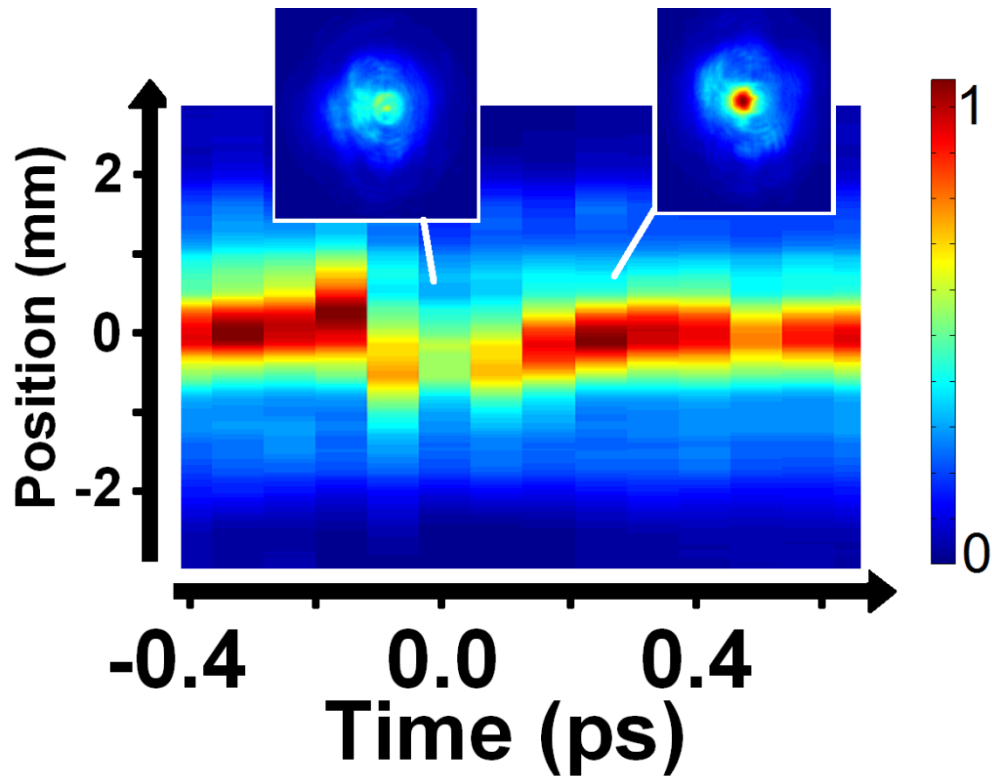


Figure 4.6: 1-D slices of the probe filament image v. pump/probe delay near $\tau \approx 0$ for 330 fs pump and probe pulses.

4.4.2 Probe filament trapping, enhancement and destruction near $\tau \approx 8.3$ ps

In the next experiment, the pump/probe delay is scanned in 33 fs steps near 8.3 ps, near the summed alignment from the full N_2 and $\frac{3}{4} O_2$ molecular revivals. Here, we can decouple the effect of pump-aligned molecules from the instantaneous response. Those responses overlap near $\tau = 0$. The pump and probe filaments are once again 130 fs in duration, and the pump/probe energies are 1.4 mJ/2.5 mJ ($1.1 P_{cr}/1.9 P_{cr}$). Additionally, the pump and probe filaments are misaligned by ~ 0.1 mrad. The resulting probe filament profile as a function of pump/probe delay is pictured in Figure 4.7.

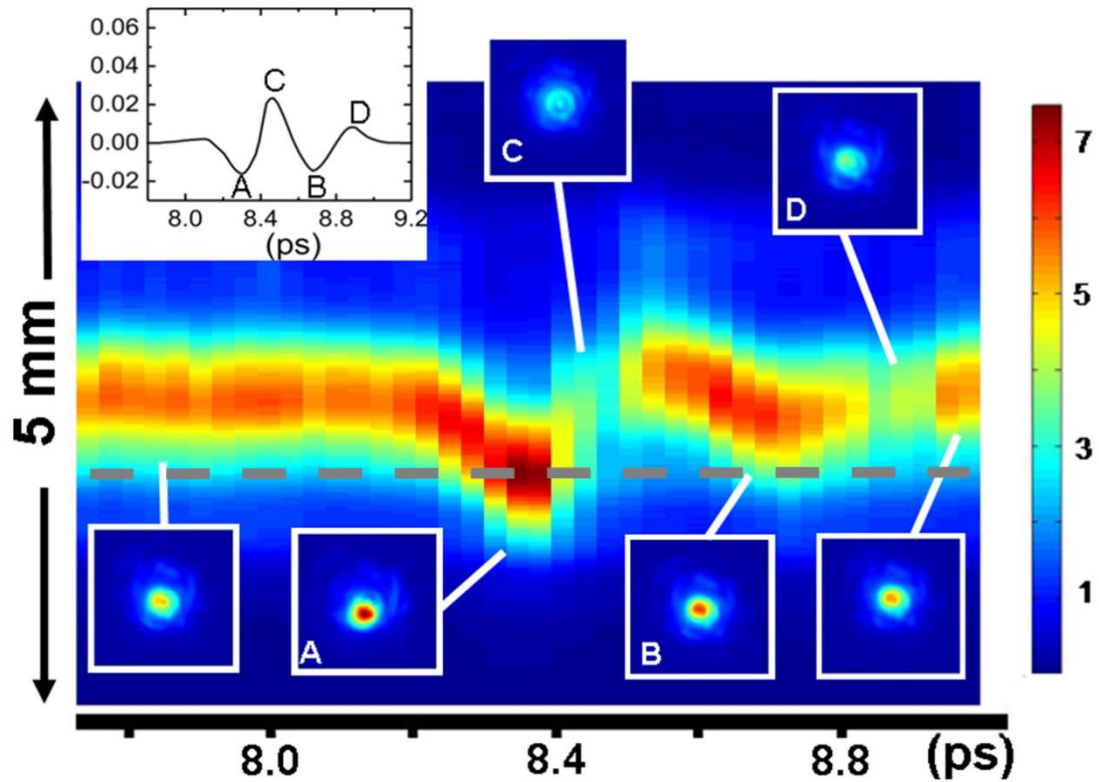


Figure 4.7: 1-D slices of the probe filament image v. pump/probe delay near $\tau \approx 8$ ps for 130fs pump and probe pulses which are misaligned by 1 mrad. Inset in the graph are the air alignment near the same delay, and 2-D images corresponding to selected delays. The dashed gray line indicates the position of the pump filament.

In this figure, the dashed gray line indicates the position of the pump filament. A plot of the air alignment in the same delay range is inset in the picture (the alignment is in the direction of pump polarization, so the alignment the probe witnesses will be of opposite sign). Selected delays in the air alignment are labeled A through D on the inset plot, and 2-D images corresponding to those delays are also inset. The most obvious feature in this plot is the enhancement and steering of the probe filament into the wake of the pump filament at delays in between 8.3 and 8.4 ps. The delay at which this enhancement occurs is labeled A in Figure 4.7, and it is near the point at which the air molecules are maximally aligned. In fact, the intervals over which the probe filament is

enhanced (A and B) or destroyed (C and D) map closely with the focusing and defocusing molecular alignment intervals. At point A, aligned N_2 gives a strong lensing effect. At point B, the less strong lensing effect is from the $\frac{3}{4}$ revival of O_2 alignment. O_2 has a larger polarizability than N_2 , but one quarter the atmospheric concentration, so its contribution to the refractive index is smaller. At point C, a filament extinction is due to perpendicularly-aligned N_2 and O_2 , because the molecular alignment waveforms constructively add at this delay. From the probe filament profile, it is clear that the lensing effect of the aligned molecules is so strong that it can drag the probe into or out of the wake of the pump, in addition to enhancing or decreasing the probe filament on-axis intensity.

The steering effect of the pump-aligned molecules is clear. We now calculate how far away a probe filament must be from a region of pump-aligned N_2 and still be trapped by their lensing effect. Trapping will occur when $k\Delta nL > \sim 1$, where Δn is the off-axis refractive index perturbation due to molecular alignment, averaged over effective interaction length $L \sim 2$ m, which is roughly the length of the pump filament. These parameters give a minimum $\Delta n \sim 6 \times 10^{-8}$ off-axis, which is approximately 0.2% of the peak on-axis Δn . Since the FWHM diameter of a filament is typically $100\mu\text{m}$, Δn of molecular alignment should fall to 0.2% of its maximum value at $r \sim 200\mu\text{m}$ (given a Gaussian intensity distribution). In our experiment, the pump and probe filaments are skewed by ~ 0.1 mrad from the exit of the 3m focusing lens and 1cm hard aperture. This means that at the collapse of the filaments (about 2.5 meters later), they would be spatially separated by $\sim 250\mu\text{m}$. This separation would give ample overlap between the

probe pulse and the pump-aligned molecules to cause steering of the probe filament into the wake of the pump.

This experiment was repeated while scanning the pump filament energy from 0.85 mJ-4.65 mJ ($0.7 P_{cr}$ - $3.6 P_{cr}$), while keeping the probe filament energy a constant 4.35mJ ($3.4 P_{cr}$) for all but the case in which the pump energy was highest (probe energy in this case was 3.05 mJ/ $2.4 P_{cr}$). The resulting probe filament profiles versus delay are shown in Figure 4.8.

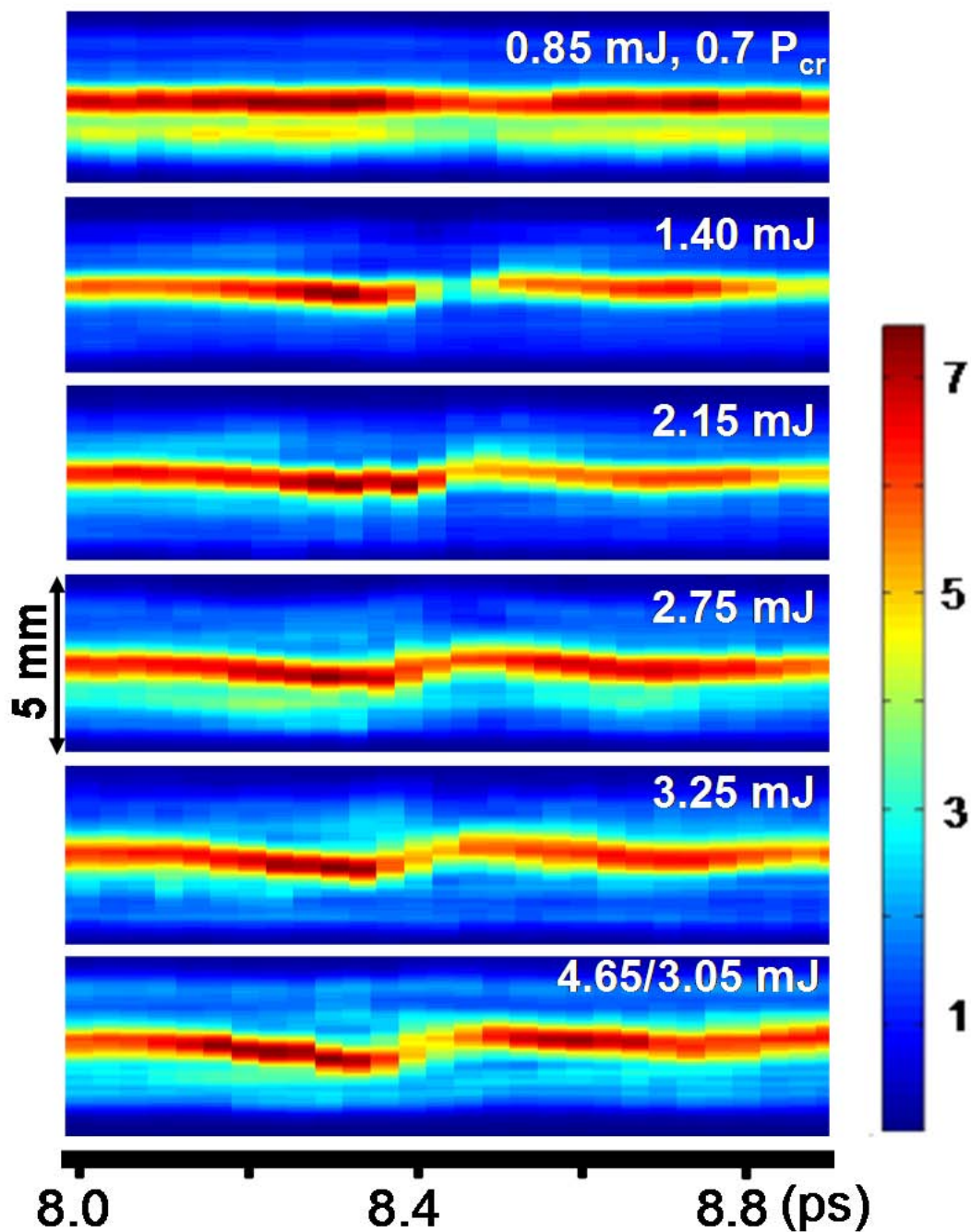


Figure 4.8: 1-D probe filament profiles v. delay for constant probe filament energy and increasing pump filament energy near $\tau \approx 8.3$ ps.

The molecular effects of steering, enhancing, and destroying the probe filament are not as evident for the lowest pump energy. Because the pump power is lower than P_{cr} , it is not filamenting, and only leaves a region of molecular alignment as long as its

Rayleigh range, ~ 10 cm. Though the axial intensity is high enough to significantly align atmospheric molecules, the interaction length L is too low to significantly lens the probe filament. At higher pump powers, the molecular effects of probe filament axial intensification and steering robustly increase, and then saturate after the pump power is increased past $2.3P_{cr}$. The persistence of molecular alignment in the face of strong pump filamentation is worth discussing.

In a strong pump filament, the axial plasma density will be high enough that plasma defocusing will compete with the focusing effects from the Kerr effect, molecular alignment, and any pre-filamentation focusing apparatus. For our 130 fs pulses, the dominant focusing effects are from the 3 m focal length lens ($f_{\#lens} \sim 300$) and molecular alignment ($f_{\#mol} \sim 200$). $f_{\#tot}^{-1} = f_{\#lens}^{-1} + f_{\#mol}^{-1}$, giving $f_{\#tot} \sim 120$. For filament stabilization, there must be enough plasma-induced defocusing to counteract this, so:

$$-f_{\#plasma} = \frac{1}{2} \sqrt{\frac{1}{2\Delta n_{plasma}}} \sim 120. \quad (4.9)$$

$\Delta n_{plasma} \sim N_e / 2N_{cr}$, where N_e is the plasma density and $N_{cr} = 1.7 \times 10^{21} \text{cm}^{-3}$, the critical plasma density for 800 nm wavelength light. Using Equation 4.9, we estimate the axial plasma density to be $N_e \sim 10^{16} \text{cm}^{-3}$. This value is less than 0.001 the density of atmosphere at room temperature and atmospheric pressure, so only $\sim 0.1\%$ of atmospheric constituents need to be ionized for the plasma to arrest self-focusing, leaving the vast majority of molecules unionized. In this way, plasma-induced defocusing clamps the maximum plasma density and axial optical intensity, resulting in the persistence of molecular alignment in the wake of a filament.

We also repeated the experiment from Figure 4.7 with collinear (not misaligned) pump and probe filaments with pump energy 3.6 mJ($2.8 P_{cr}$) and probe energy 4.6 mJ($3.6 P_{cr}$). The 1-D profile of the probe beam versus delay is pictured in Figure 4.9.

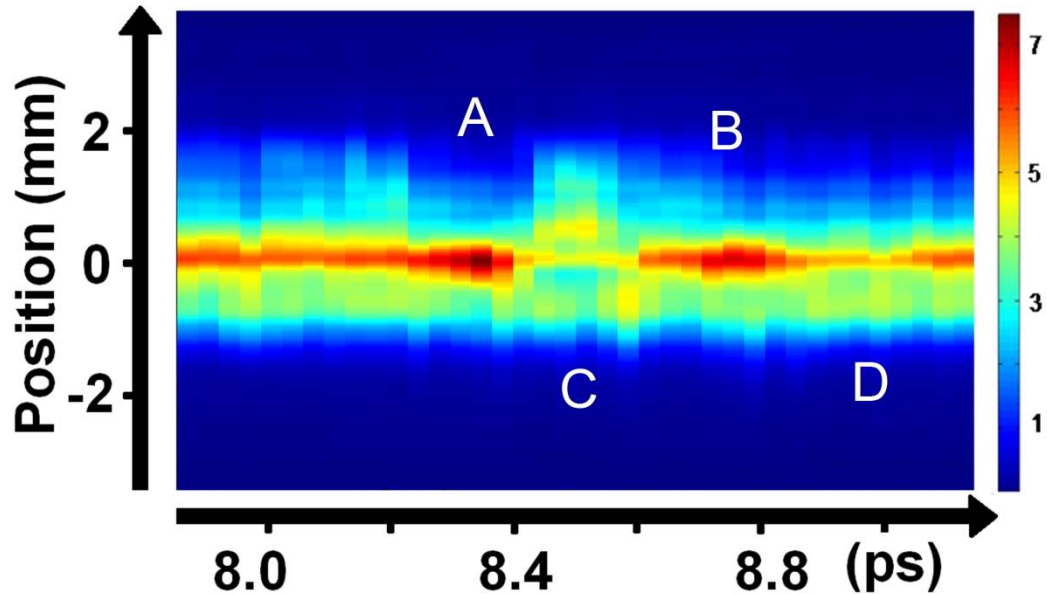


Figure 4.9: 1-D slices of the probe filament image v. pump/probe delay near $\tau \approx 8$ ps for 130 fs, collinear pump and probe pulses.

The behavior of the halo of light that surrounds the high-intensity filament, often called the “reservoir” [7], is important to filamentary propagation. Liu et al [84] placed a 300-micron pinhole 2.75 meters after the beginning of a plasma filament. They found that the plasma recombination radiation, which was 4.5 m in length without the pinhole, abruptly stopped a few centimeters after the pinhole when it was in place, even though the high intensity core of the filament was allowed to pass through. Simulations [18] and experiments like the one above have shown that the high intensity light at the core of the filamenting pulse, which leaves the core due to defocusing and losses due to ionization, gets replenished (hence the name “reservoir”) by the surrounding light continually self-focusing towards the center.

The results depicted in Figure 4.9 show that the brightening of the core of the probe filament at pump/probe delay corresponding to position A on the plot comes at the expense of the reservoir, whose intensity drops at the same delay. Conversely, when the filament core is destroyed by anti-aligned N₂ and O₂ at position C, the light seems to have been expelled back into the reservoir, whose intensity rises at the same delay. This result is particularly compelling, because it shows that by controlling the alignment of atmospheric N₂ and O₂, we are able to exercise control over the probe filament nonlinearity at its high-intensity core and also in the weaker parts of the beam.

4.4.3 Measurement of spectral broadening

One characteristic of filamentation is broadening of the filamenting pulse spectrum and white light generation in the pulse propagation direction. With our measurement of the spectral content of the probe filament as a function of pump/probe delay, we showed that when a probe filament is trapped in a quantum molecular wake, the white light in the filament is also enhanced.

The white light enhancement of a trapped filament is easy to see with the naked eye. Figure 4.10 shows three pictures of the pump and probe filaments incident on an index card just before the filament imaging system. We took the pictures with a Canon Powershot A4 digital camera. The pump and probe filaments are $2.3 P_{cr}$ and $2.5 P_{cr}$, respectively, and are again misaligned by ~ 0.1 mrad. The figure shows pump and probe filaments at a pump/probe delay τ (i) not specific to any molecular revival, (ii) ~ 8.35 ps, where probe trapping due to focusing of aligned N₂ occurs, and (iii) ~ 8.5 ps, where anti-aligned N₂ and O₂ deflect the probe away from the pump.

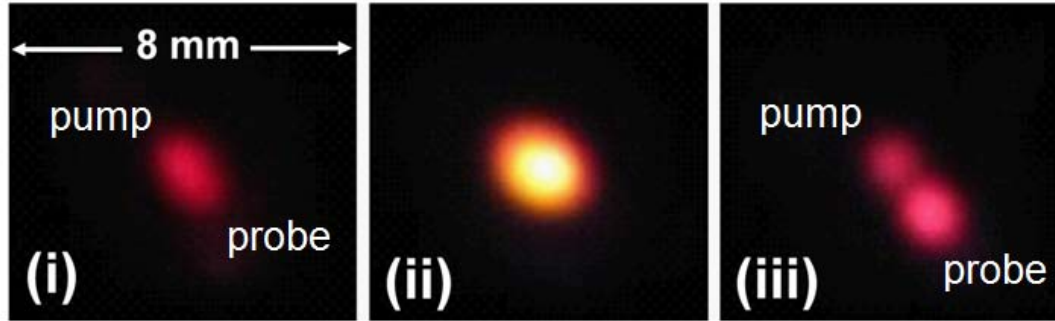


Figure 4.10: digital camera image of pump and probe filaments incident on an index card at three different delays near 8.3 ps. (i) at non-specific τ , where there is no alignment, (ii) is at $\tau \sim 8.35$ ps, where aligned N_2 steers the probe filament into the pump path, and (iii) is at $\tau \sim 8.5$ ps, where anti-aligned N_2 and O_2 deflect the probe from the pump path.

The CCD chip in the digital camera is sensitive to both visible and infrared radiation.

When the probe filament encounters aligned molecules at the full revival of N_2 , it clearly gets dragged in to the pump filament wake and either is so intense on the index card, or creates so much white light, that it saturates many of the detector pixels. This observation suggests higher probe filament intensity, a longer probe filament, or both.

We see an even more detailed dependence of the probe spectrum on pump/probe delay in our fiber spectrometer measurement of the probe filament. This dependence is shown in Figure 4.11.

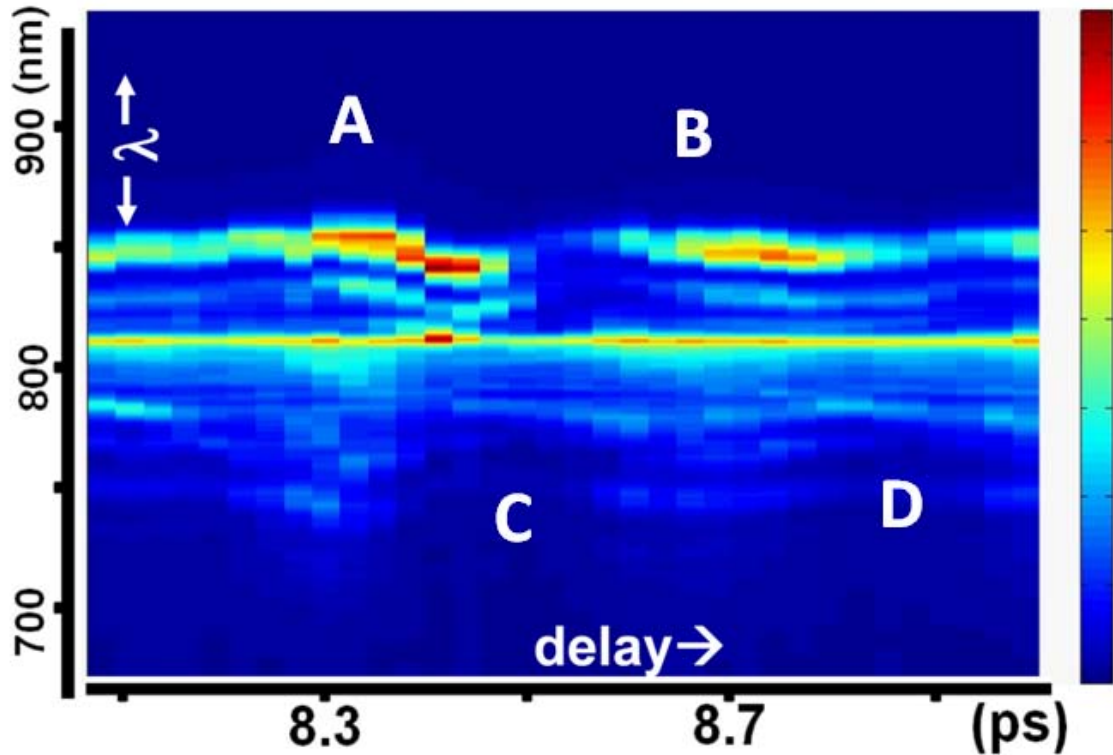


Figure 4.11: Probe filament spectrum as a function of delay (33 fs steps) through the air alignment revival near $\tau=8.3$ ps.

Previous studies have documented the spectrum and phase of weak pulses that probe rotational wakes in gas cells [65, 67, 82, 85], but this is the first measurement of the spectrum of a high power filamenting pulse probing such wakes in the atmosphere. At delays long before or after the molecular wake near $\tau = 8.3$ ps, the probe spectrum is very broad, corresponding to measurements made by many other groups.

Major noticeable effects of molecular alignment are the general broadening of the probe spectrum when it encounters aligned N_2 or O_2 and the narrowing of the probe spectrum when it encounters anti-aligned molecules. The narrowing of the spectrum (for example, at points labeled C and D on Figure 4.11) can be explained by the destruction of the filament due to the defocusing effect of the anti-aligned molecules. If the filament is arrested, the light simply propagates at lower intensity and experiences fewer nonlinear

effects, such as broadening due to self-phase modulation from bound electrons, rotational effects, and plasma generation.

The broadening of the probe spectrum near delays labeled A and B in Figure 4.11 can be qualitatively described as follows. At both points, the large blue wings of the spectrum can be attributed to molecular focusing leading to extra ionization. Ionization induced self-phase modulation typically causes a blue-shifted spectrum— $\Delta\omega_{lin} > 0$ —since the emergence of plasma causes a temporal drop in the refractive index, retarding the phase (and accelerating the phase velocity) of later parts of the pulse. The temporal structure of the quickly changing molecular alignment can also describe how some of the finer spectral features change versus pump/probe delay. Because the changing molecular alignment generates a time-varying refractive index shift, it will impart time-varying phase modulation to the probe pulse in the form of linear and quadratic frequency shifts:

$$\Delta\omega_{lin} \sim -\frac{\partial\varphi}{\partial t} \text{ and } \Delta\omega_{quad} \sim -(t - t_0) \left[\frac{\partial^2\varphi}{\partial t^2} \right]_{t=t_0}, \text{ where } t_0 \text{ is a point at the peak of}$$

molecular alignment such as A or B. At such delays, the probe pulse will experience both $\Delta\omega_{lin}$ and $\Delta\omega_{quad}$. If the probe filament co-propagates with the molecular revival at a time delay during which the pulse duration is at inflection between peaks, it will experience either positive or negative $\Delta\omega_{lin}$. So when the probe filament is exactly at a time delay t_0 like at positions A and B, it experiences $\frac{\partial^2\varphi}{\partial t^2} > 0$, which explains the blue-shift for $t < t_0$ followed by the red-shift for $t > t_0$.

4.5 Conclusions and future experiments

The experiments and analyses in this chapter clearly show that air molecules can be pre-aligned in order to affect the long-range propagation of a high intensity probe

filament. The alignment wake can control the intensity of the probe filament, as well as steer its position and modulate its spectrum. The molecular wake is robust enough to produce these effects at a wide range of pump and probe powers.

Although we have reason to believe that the focusing effect of pump-aligned N₂ and O₂ in the atmosphere causes more intense and/or longer probe filamentation, it is worth noting that without a diagnostic of the actual plasma density in the probe filament, we cannot directly prove this point. We also note that the time delays over which we see the highest probe filament intensity and greatest spectral broadening do not coincide, nor do they perfectly correspond to peak molecular alignment from the probe pulse as measured by SSSI. In fact, the probe filament with the most enhanced axial intensity happened a few tens of femtoseconds later than the peak N₂ alignment predicted by SSSI.

One explanation for the discrepancy is that the strongly filamenting probe pulse re-aligns the pump-aligned N₂ and O₂. This phenomenon is not described by our simulations or SSSI measurements, because those assume or involve a very weak, non-perturbative probe pulse. To get a real idea of the true alignment the probe filament sees, we must simulate molecular alignment driven by two intense optical pulses.

Another factor we do not take into account with our analysis is that phase modulation and trapping due to aligned molecules will alter the temporal structure of the probe pulse in ways that may favor or discourage filamentation. Simply monitoring the filament profile at one point and measuring its spectrum is not enough to test this idea. We would need to measure the full electric field envelope $E(t)$ of the probe pulse to draw further conclusions about the physical processes at work.

The next chapter will show the results of successful efforts to resolve the spectral phase and envelope of the filamenting probe pulse, and the plasma density of the probe filament.

Chapter 5: Coherently excited quantum wake-induced pulse shaping and extension of femtosecond air filaments

5.1 Introduction

In this chapter, it is shown that the molecular quantum wake can temporally and spatially shape a filamenting probe pulse while significantly extending the nonlinear propagation distance. The wake does so by disrupting the usual balance between nonlinear focusing and plasma defocusing responsible for extended filament propagation. In a single pulse filament, the radially confined high intensity region (typically $<100\ \mu\text{m}$ in diameter) is not really akin to the intensity confinement in a glass or plasma optical fiber [86, 87], where there is no transverse energy exchange with zones outside the confinement region. In a typical single-pulse filament, however, the high intensity region is quasi-stably sustained by simultaneous incoming and outgoing energy exchange with a wider co-propagating ‘reservoir’ whose transverse extent is roughly defined by the spatial envelope of the original beam [18]. We show here that by applying an intense probe pulse field coherently to the co-propagating rotational wake induced by the pump pulse, the wake is strongly shaped and enhanced so as to self-consistently support an enhanced filament, in which quantum molecular lensing dominates both Kerr focusing and plasma defocusing. Remarkably, the wake shaping and filament extension is sensitive to pump-probe delay on a 10 fs timescale.

5.2 Interferometric optical plasma density measurement

Our experiment measures both the detailed electron density profile produced in the probe pulse-enhanced filament and the envelope and phase of the probe pulse exiting the filament. The density profile measurement uses our recent interferometric scheme [14] and the probe pulse electric field is measured using self-referencing spectral interferometry (SPIDER, [57]). Figure 5.1 shows the experimental setup.

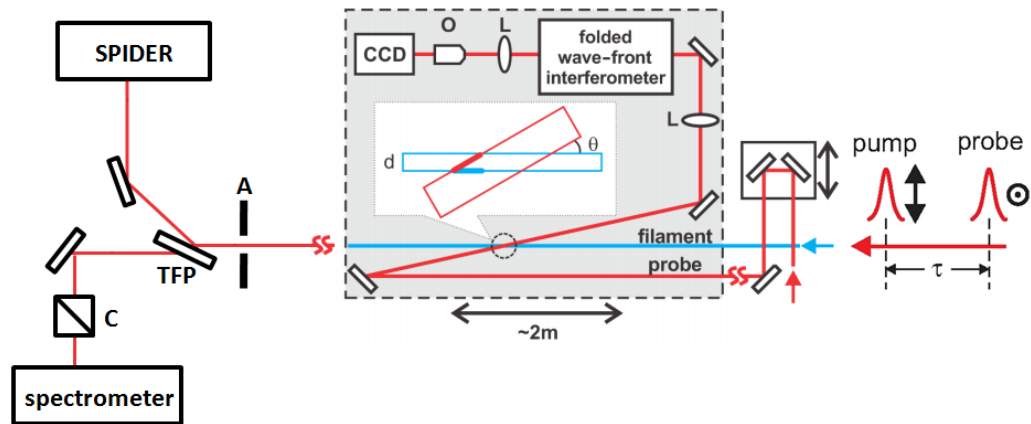


Figure 5.1: Filamenting pulse diagnostic experiment. The plasma density is measured by an optical interferometry setup on a sled (shaded gray region). L indicates a lens and O is a microscope objective. The filamenting probe pulse is selected by an aperture A and TFP before being sent into SPIDER. Residual probe light is separated from the pump using a cube polarizer C and sent into a broadband fiber spectrometer.

Orthogonally polarized, collinear pulses (pump and probe) are produced from the main pulse, with one arm delayed by a computer controlled stepper motor [10]. The pulses pass through a 3.1 m focal length lens, immediately followed by a 5.5 mm diameter aperture. The orthogonal polarization allows later separation of the probe pulse for SPIDER measurements. For the electron density diagnostic, a probe beam split from the main beam counterpropagates across the filament axis at 0.75° and enters a folded wavefront imaging interferometer mounted on a carriage with 2 m travel along the filament axis [14]. The small crossing angle enhances the sensitivity to the low electron density (typically $<10^{17} \text{ cm}^{-3}$) of filaments, with the price paid a reduced axial resolution

of ~ 5 mm, which is of little concern for our meter-scale filaments. Our technique allows measurement of plasma density as low as $\sim 5 \times 10^{14} \text{ cm}^{-3}$, with a transverse resolution of $5 \mu\text{m}$. Radial density profiles, averaged from ~ 100 shots, were measured every 1 cm along the filament, and were extracted with standard techniques [58]. For all measurements, the pump energy and pulsewidth were $\epsilon_{\text{pump}} = 1.5 \text{ mJ}$ and $\tau = 80 \text{ fs}$, which easily formed extended single filaments as expected at $\sim 2 P_{\text{cr}}$, where the critical power for self-focusing is $P_{\text{cr}} \sim 10 \text{ GW}$ at this pulsewidth [10]. The probe pulse energy ϵ_{probe} was varied in the range 1.0-2.5 mJ with pulsewidth 90 fs. All parameters were measured after the lens. Single filament propagation with pump plus probe was verified by examination of electron density profiles as well as the white light spot in the filament far field.

The effect of delaying the injection of a 1.85 mJ probe pulse into the filament formed by the pump is shown in the electron density measurements of Figures 5.2(a) and (b), showing the peak on-axis electron density at each position.

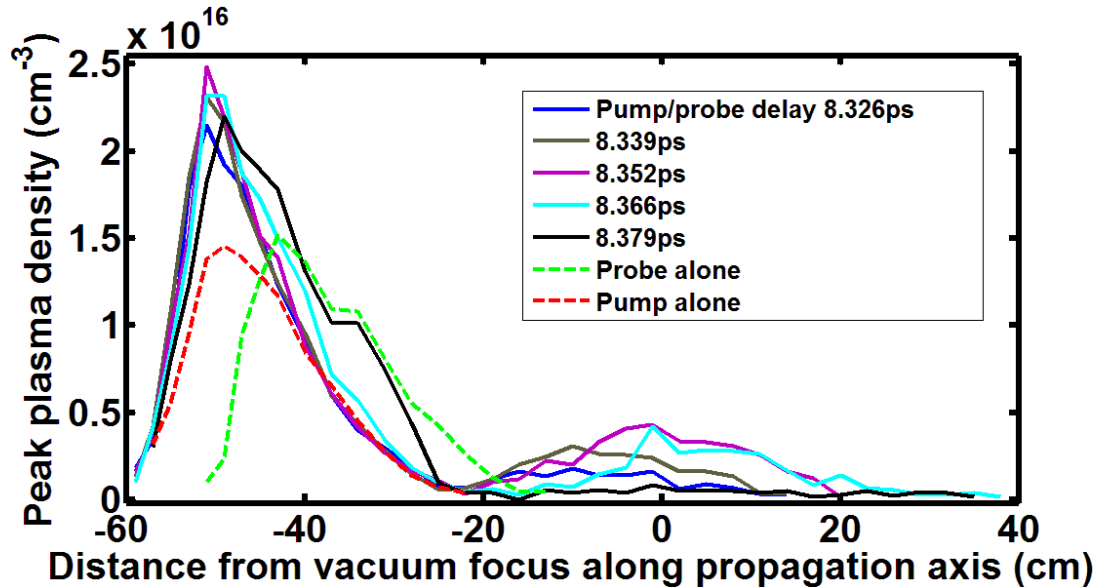


Figure 5.2(a): Peak on-axis electron density of the plasma filament for pump/probe delays from 8.326 ps-8.379 ps. Plasma density of pump and probe filaments alone are shown with dashed lines.

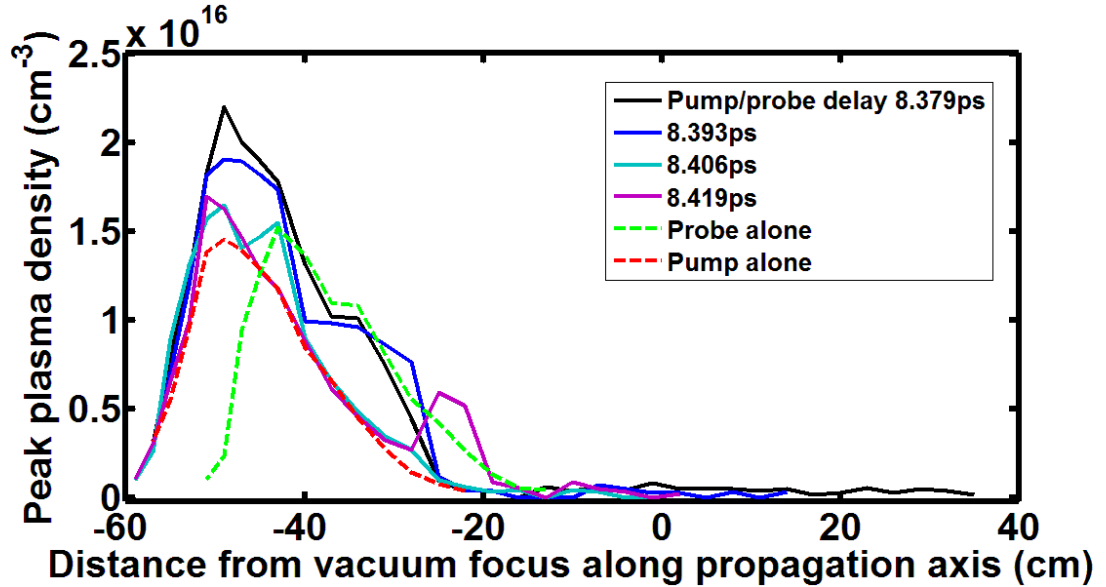


Figure 5.2(b): Peak on-axis electron density of the plasma filament for pump/probe delays from 8.379 ps-8.419 ps. Plasma density of pump and probe filaments alone are shown with dashed lines.

The range of delays chosen is near the full rotational revival of N_2 ($T_{N_2} = 8.3$ ps) and the $3/4$ revival of O_2 ($3/4 T_{O_2} = 8.7$ ps), which have a sum effect on the air refractive index [10]. With the pump alone, filament formation and plasma generation occurs well before the vacuum focus ($z=0$ on the axial scale), with a peak density $\sim 1.5 \times 10^{16} \text{ cm}^{-3}$ and axial extent ~ 25 cm. The probe-alone filament, with similar shape, is displaced forward by ~ 10 cm owing to the slightly lower peak power of the probe pulse. The general form of the pump plus probe filaments is a $\sim 70\%$ enhanced first peak, followed by a long electron density recurrence (peak $\sim 0.5 \times 10^{16} \text{ cm}^{-3}$) with axial extent up to $z = 40$ cm. The filament length is approximately tripled at the optimum probe delays of 8.37 to 8.38 ps. There are several notable aspects of this plot. First, the extended sections at each delay all begin at $z \sim -23$ cm, where the first peak reaches a minimum. Second, the filament extension profile shows a remarkably fine sensitivity to probe delay on a ~ 10 fs timescale. After a delay of $\tau = 8.38$ ps, the electron density in the extended part of the filament abruptly

drops to close to our threshold sensitivity level. Figure 5.3 shows the sequence of electron density profiles for delays $\tau=8.38$ ps and greater where, except for $\tau=8.38$ ps, there is no density enhancement above the pump or probe alone.

The effect of probe energy near the onsets of the first peak ($z = -54$ cm) and the second peak ($z=-9$ cm) are shown in Figures 5.3(a) and (b) below. In these plots, it is evident that the plasma density is enhanced at pump/probe delays near $\tau=8.37$. However, in this energy scan experiment, since the density was not measured at more axial positions, it is not clear that whether the overall peak density increases with increasing probe pulse energy, or if it shifts to a different axial location.

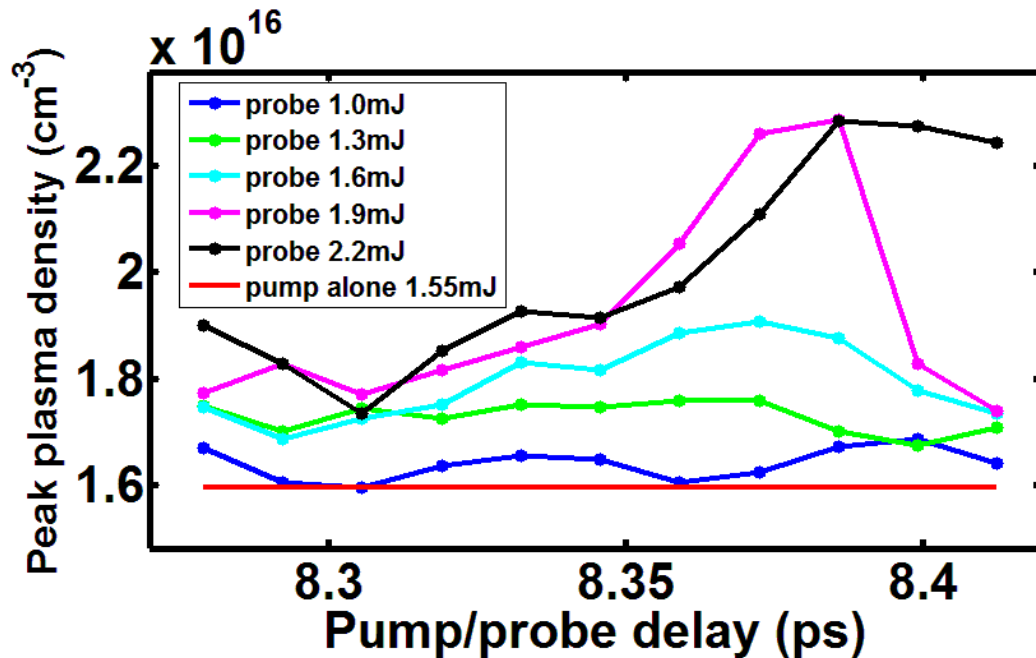


Figure 5.3(a): Peak on-axis electron density of the plasma filament v. pump/probe delay 54 cm before vacuum focus for a range of probe pulse energies. The pump plasma present in absence of the probe is indicated in red.

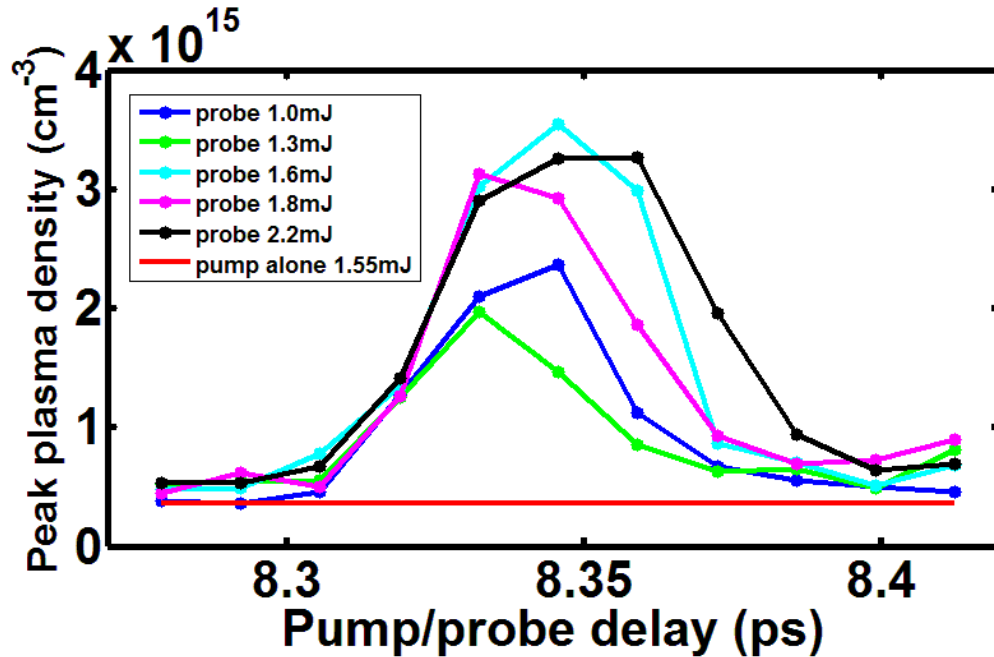


Figure 5.3(b): Peak on-axis electron density of the plasma filament v. pump/probe delay 9cm before vacuum focus for a range of probe pulse energies. The pump plasma present in absence of the probe is indicated in red.

5.3 SPIDER measurement of probe electric field

The effect on an intense probe pulse's envelope and phase from propagation in the pump-induced molecular wake was measured by SPIDER. The goal was to extract this information from the central high intensity filament where the rotational wake is concentrated. The pump and probe were orthogonally polarized (see Fig. 1), allowing the probe to be filtered off by reflection from a broadband thin film polarizer. It was verified that the polarizer did not distort the pulse's spectrum or phase by comparing probe-only filament SPIDER traces with those using reflection from a fused silica flat. The beam was passed through a 1.3 mm diameter aperture centered on the central supercontinuum spot 2 m after the end of the filament (taken as the location beyond which the electron density was below the measurement threshold). It then propagated another 3.28 m to the

nonlinear crystal in the SPIDER. It was found that extracted pulse envelope and phase converged for apertures with diameter d where $1.0 < d < 1.7$ mm; above 2 mm, SPIDER results were aperture-dependent owing to beam nonuniformities and interference effects. For $d \leq 1.0$ mm, not enough signal made it into the spectrometer to accurately resolve the interference pattern. This is illustrated in Figure 5.4, where we display SPIDER interferograms (2-D spectra in the right hand column) and corresponding retrieved $I(t)$ (left hand column) for a singly filamenting, 1.6 mJ pulse passing through circular apertures of increasing diameter (inset).

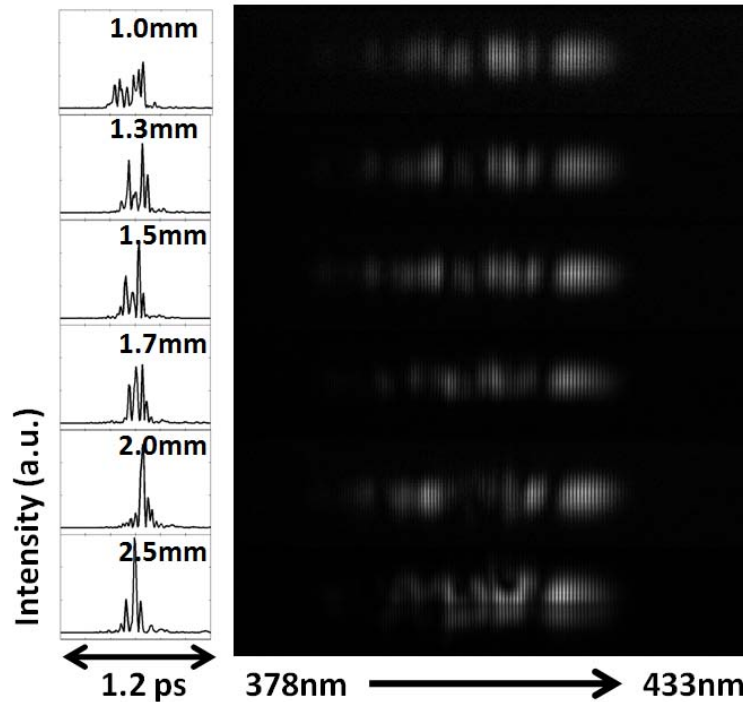


Figure 5.4: Raw SPIDER interferograms (2D spectra in the right hand column) and corresponding retrieved $I(t)$ (left hand column) for a singly filamenting, 1.6 mJ pulse passing through circular apertures of increasing diameter (inset).

The probe field in the spectral domain, $|\tilde{E}(\omega)|e^{i\varphi(\omega)}$, was determined as follows. For each pump-probe time delay, 200 SPIDER spectral interferograms (200 laser shots) were taken. The spectral phase was extracted from each interferogram (see Section 2.4.1) and then averaged over the number of shots to yield $\varphi(\omega)$, while the spectral amplitude

$|\tilde{E}(\omega)|$ was taken from an auxiliary spectrometer. The time dependent field $|\tilde{E}(t)|e^{i\phi(t)}$ is simply the Fourier transform of $|\tilde{E}(\omega)|e^{i\phi(\omega)}$. Note that $\phi(\omega)$ was corrected for the air group velocity dispersion of $\beta = 22 \text{ fs}^2/\text{m}$ [16] experienced in propagation from the end of the filament to the SPIDER. The correction amounts to less than 10 rad in the spectral wings of the pulse.

Figure 5.5 shows intensity vs. time plots, $I(t) \propto |\tilde{E}(t)|^2$, for a sequence of pump-probe delays near 8 ps. Here, the probe energy is 2.5 mJ.

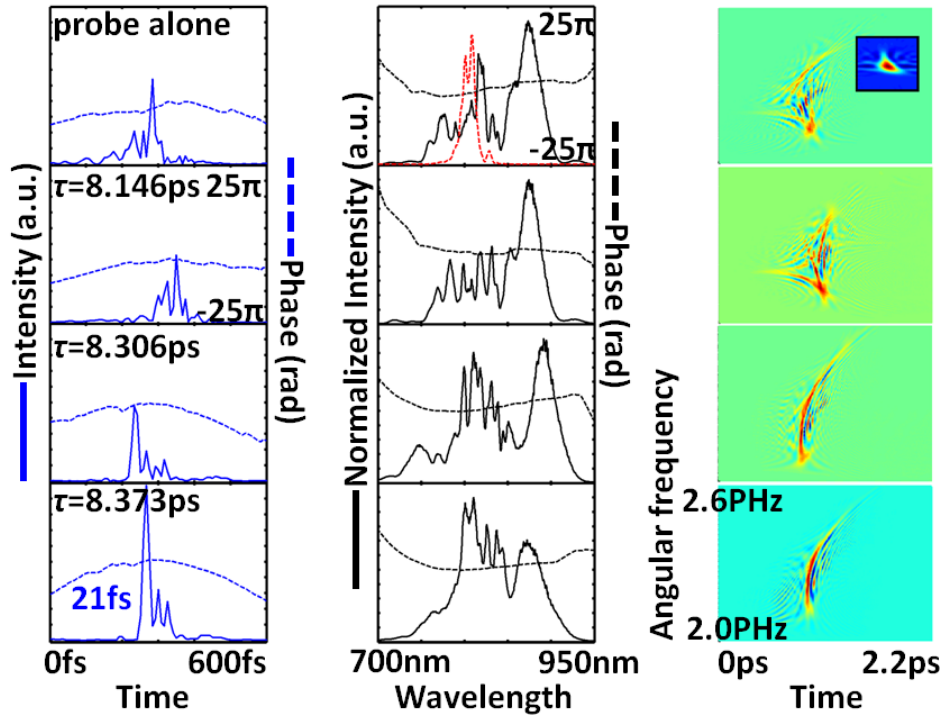


Figure 5.5: First column: measured $I(t)$ and $\Phi(t)$ for a 2.5 mJ probe pulse for selected pump/probe delays. Second column: corresponding $I(\lambda)$ and $\phi(\lambda)$, with the pre-filamentation spectrum in dashed red lines. Third column: corresponding Wigner plots, with the pre-filamentation Wigner plot inset at the top right.

Note that the probe alone pulse breaks up into multiple spikes, as is consistent with both filamentary self-focusing of different time slices in the pulse [18] and interference of spectral components nonlinearly generated from self-phase modulation.

With the pump on, and the probe delayed by 8.146 ps (about ~ 150 fs before the onset of the revival), the pulse is qualitatively similar, showing multiple spikes, but then as delay increases, the pulse ‘cleans up’, developing a dominant leading spike followed by a much smaller wing as seen by 8.373 ps. The time-dependent phase $\Phi(t)$ is superimposed as a dashed line. Figures 5.6(a-c) show the evolution of $I(t)$, $I(\omega)$ and the Wigner diagram at finer intervals, all corresponding to delays *within* the air revival.

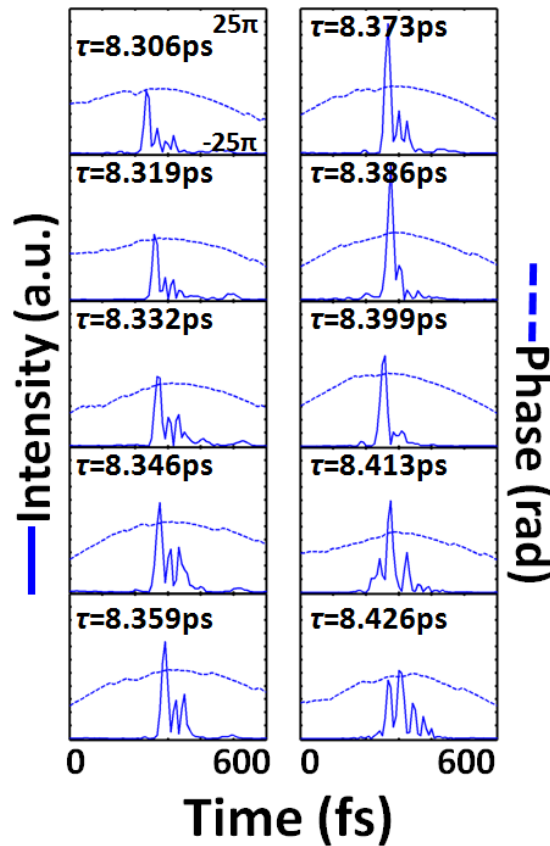


Figure 5.6(a): Measured $I(t)$ and $\Phi(t)$ for a 2.5 mJ probe pulse finely spaced pump/probe delays within the air revival between 8.306 ps and 8.426 ps.

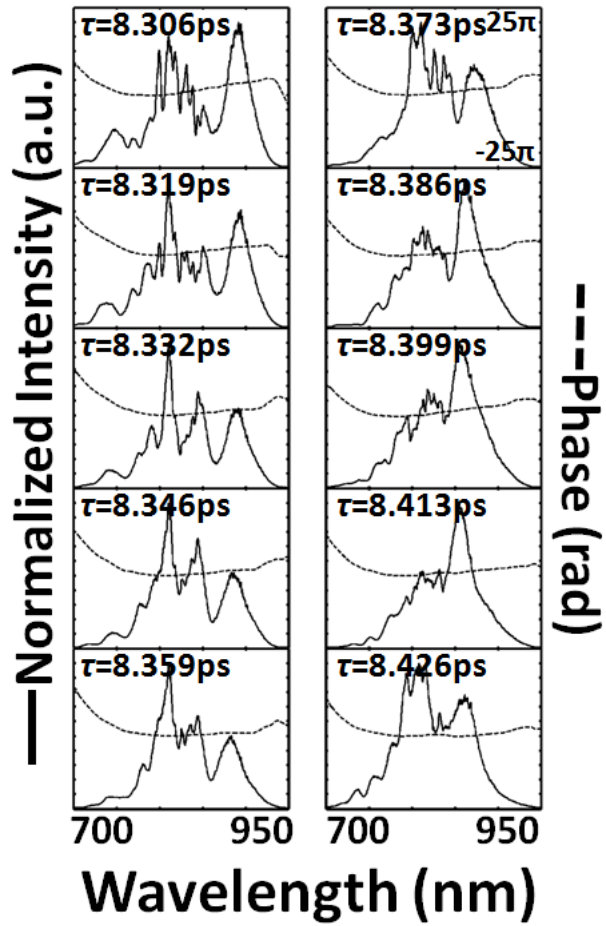


Figure 5.6(b): Measured $I(\lambda)$ and $\phi(\lambda)$ for a 2.5 mJ probe pulse finely spaced pump/probe delays within the air revival between 8.306 ps and 8.426 ps.

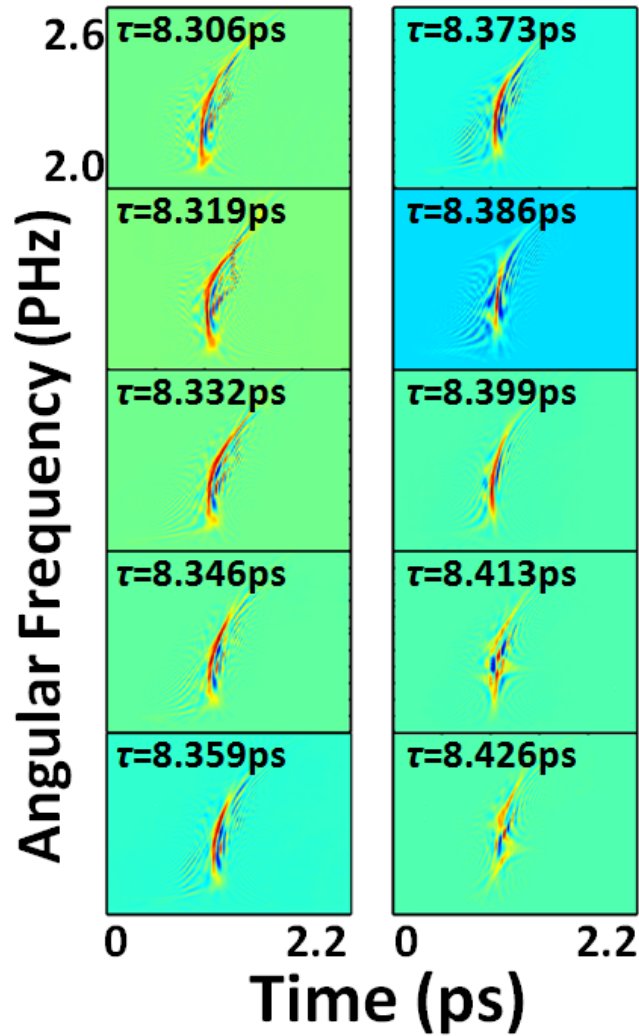


Figure 5.6(c): Measured Wigner diagrams for a 2.5 mJ probe pulse finely spaced pump/probe delays within the air revival between 8.306 ps and 8.426 ps.

Note that $I(t)$ for $8.359 \text{ ps} < \tau < 8.399 \text{ ps}$, a 40fs interval, shows an especially dominant spike, with reduced temporal wings. Beyond this interval, the pulse begins to break up again and in fact, the extended filament disappears. Figure 5.5 additionally shows the spectral amplitudes and phases corresponding to displayed $I(t)$, where the spectra corresponding to the above interval are more compact and less modulated. Figure 5.5 also shows Wigner plots of the extracted fields, a useful representation explicitly displaying any chirps present [88]. These plots, in the right column, also show an

interesting trend. The probe alone and $\tau = 8.146$ ps cases show significant modulations in both the frequency and time directions, consistent with the pulse splitting and interference mentioned earlier. As the interval 8.359 ps $< \tau < 8.399$ ps is approached, as seen in Fig. 5.6(c), the Wigner traces become smoothly arching, with a strong red to blue shift from the front to the back of the pulse. Beyond this interval, the Wigner plots again develop modulations in time and frequency. Two other probe energies were used, 1.0 mJ and 1.6 mJ, with similar results (see Figs. 5.7, 5.8, and 5.9(a-c)), where it is seen that the pulse cleaning and narrowing effect is stronger with higher probe energy.

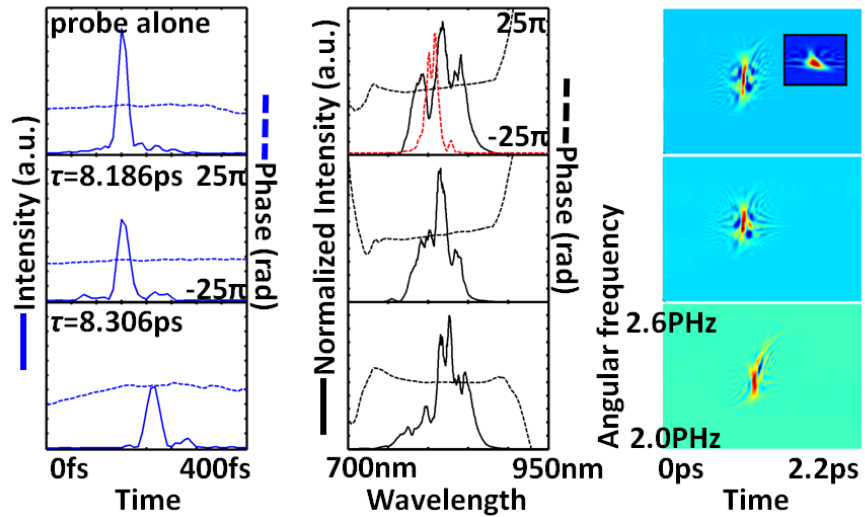


Figure 5.7: First column: measured $I(t)$ and $\Phi(t)$ for a 1.0 mJ probe pulse for selected pump/probe delays. Second column: corresponding $I(\lambda)$ and $\varphi(\lambda)$, with the pre-filamentation spectrum in dashed red lines. Third column: corresponding Wigner plots, with the pre-filamentation Wigner plot inset at the top right.

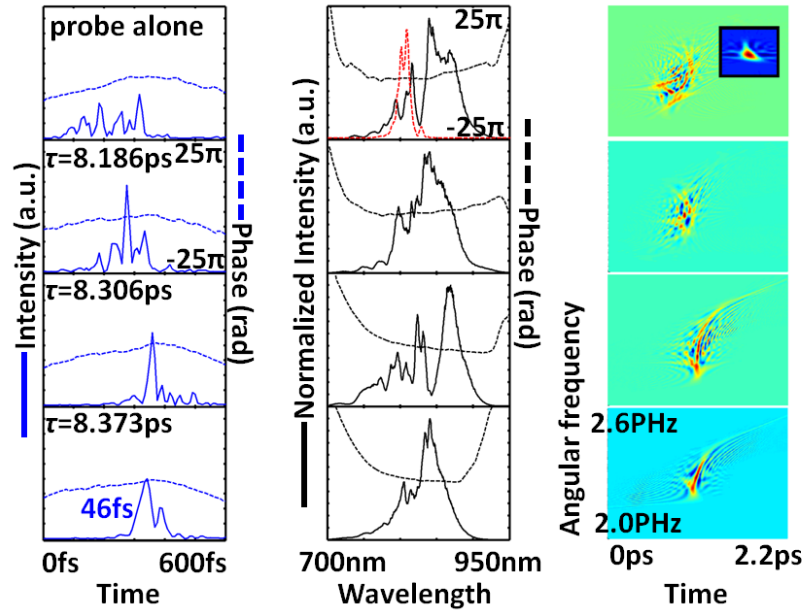


Figure 5.8: First column: measured $I(t)$ and $\Phi(t)$ for a 1.6 mJ probe pulse for selected pump/probe delays. Second column: corresponding $I(\lambda)$ and $\phi(\lambda)$, with the pre-filamentation spectrum in dashed red lines. Third column: corresponding Wigner plots, with the pre-filamentation Wigner plot inset at the top right.

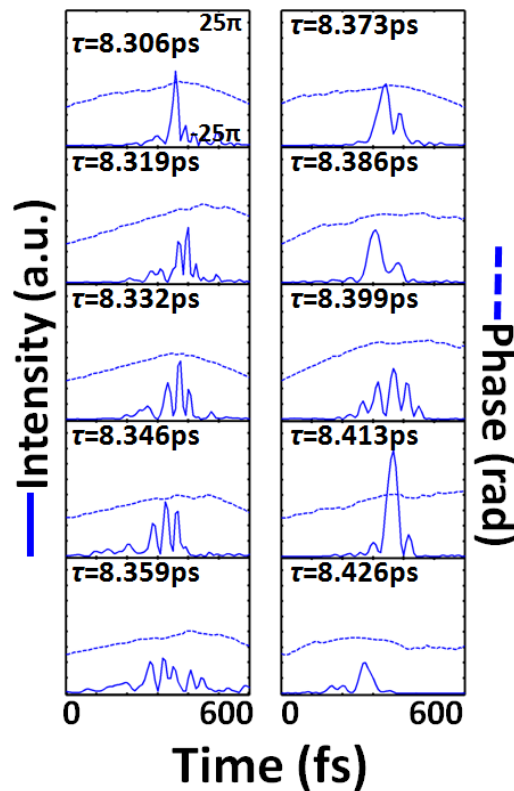


Figure 5.9(a): Measured $I(t)$ and $\Phi(t)$ for a 1.6 mJ probe pulse finely spaced pump/probe delays within the air revival between 8.306 ps and 8.426 ps.

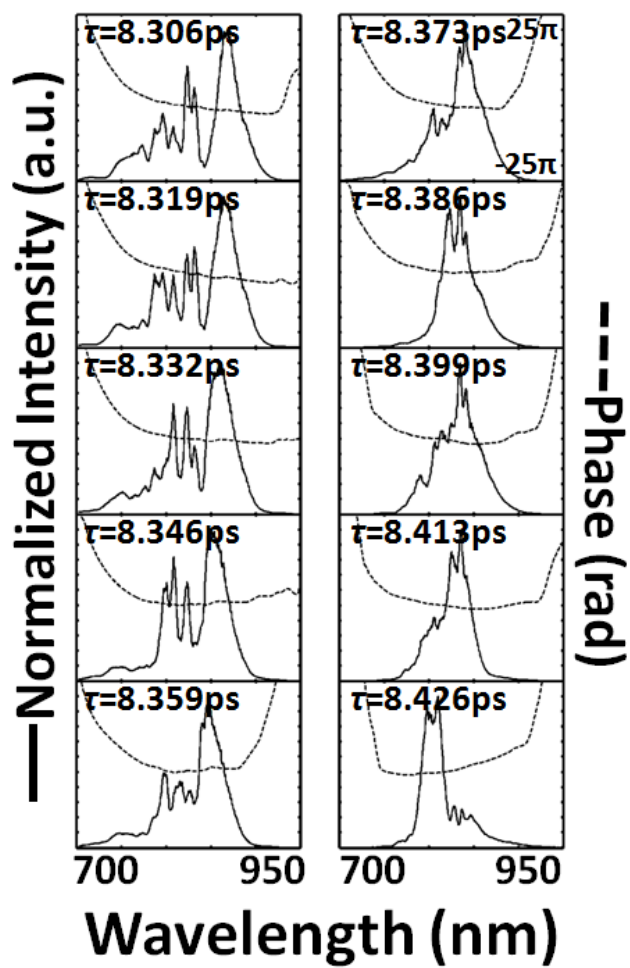


Figure 5.9(b): Measured $I(\lambda)$ and $\varphi(\lambda)$ for a 1.6 mJ probe pulse finely spaced pump/probe delays within the air revival between 8.306 ps and 8.426 ps.

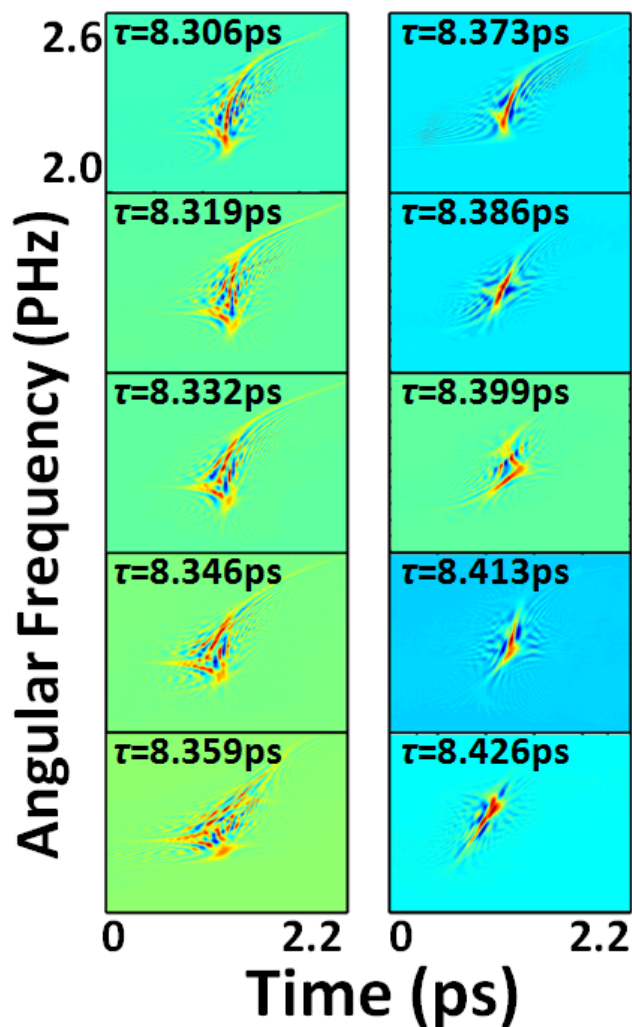


Figure 5.9(c): Measured Wigner diagrams for a 1.6 mJ probe pulse finely spaced pump/probe delays within the air revival between 8.306 ps and 8.426 ps.

5.4 Discussion and analysis

Reexamination of the pump-probe delays corresponding to the axially extended filaments of Fig. 5.2 reveals they are highly correlated with the unusual trend in pulse evolution shown in Figs. 5.5-5.9. That is, the interval $8.359 \text{ ps} < \tau < 8.399 \text{ ps}$ over which the pulse shortens and suppresses its wings corresponds to the delay range of significant lengthening of the filament axial profile. As seen on Fig. 5.2, these profile changes are sensitive, remarkably, to $\sim 10 \text{ fs}$ changes in pump-probe delay

The explanation for this sensitivity of pump-probe delay to pulse shaping and filament enhancement lies in the coherent two-pulse excitation of molecular wavepackets in air. The coherent interaction is modeled using a non-perturbative density matrix code [to be published]. For high intensities, this is an improvement over the perturbative model presented in Chapter 3 and ref [67].

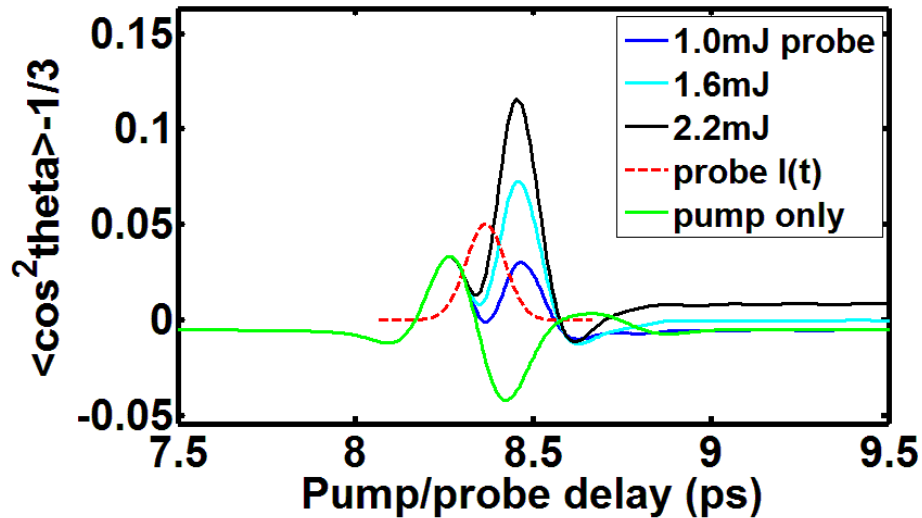


Figure 5.10: Air molecular alignment (proportional to Δn) due to a pump pulse at $t = 0$ and probe pulse at delay $\tau = 8.366$ ps for several probe pulse energies. The probe pulse envelope is shown with a dashed red line, and the alignment due to only the pump pulse is in green.

Figure 5.10 shows the result on the Δn (proportional to effective air molecular alignment $\langle \cos^2 \theta \rangle - 1/3$) experienced by the probe (red curve) when it is at delay $\tau = 8.366$ ps (pump pulse peak intensity 5×10^{13} W/cm², probe energy variable and shown on plot). The pulse envelopes are modeled as cosine-squared to ensure they go to zero at finite times. The pump alone curve is green and shows a leading positive Δn followed by a negative excursion. As the probe intensity increases, it is seen that the negative excursion is reversed with the response forming a well followed by an increasingly large peak.

Figure 5.11(i) shows the air molecular alignment due to a sequence of two perpendicularly polarized pulses delayed by $\tau = 8.373$ ps, each with peak intensity 5×10^{13} W/cm². Figure 5.11(ii) shows air alignment due to two pulses synthesized from the sum of the individual response of one pulse at $\tau = 0$ and the other perpendicularly polarized pulse at $\tau = 8.373$ ps.

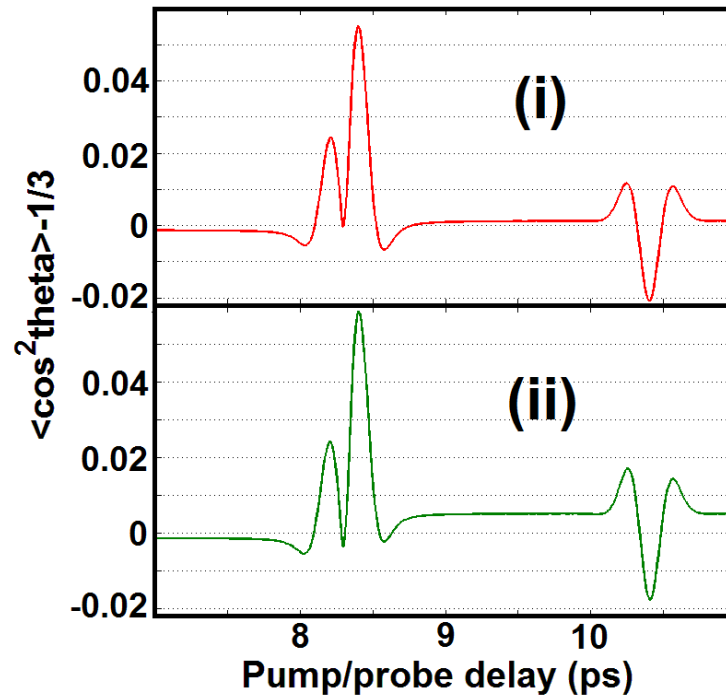


Figure 5.11: (i-red) Air molecular alignment due to a sequence of two perpendicularly polarized pulses delayed by $\tau = 8.373$ ps, each with peak intensity 5×10^{13} W/cm². (ii-green) Air alignment due to two pulses synthesized from the sum of the individual response of one pulse at $\tau = 0$ and the other perpendicularly polarized pulse at $\tau = 8.373$ ps.

In the two-pulse plot, as opposed to the plot synthesized using the individual pulse responses, the dip in alignment near 8.3 ps is not as deep, and the following alignment peak is not as high. There is a high level of DC molecular alignment evident in the summed plot that does not exist in the two-pulse plot. These results are a direct

demonstration of the *coherent* interaction between the probe and the pump-prepared molecular ensemble.

Figures 5.10 and 5.11 refer to rotations only, but in a filament, both the Kerr (instantaneous) response and plasma generation affect the refractive index. We can estimate the effect of these contributions as follows. From our work described in ref [14] we found that propagation simulations fit the measured electron density profiles best if the Kerr response was $\sim 15\%$ of the peak response owing to molecular alignment. Also, from Fig. 5.2, our measurement of the electron density gives bounds on a maximum index shift due to plasma generation. The transient responses for all three contributions are shown in Fig. 5.12, for $\tau = 8.366$ ps, where we use the fact that the electronic Kerr effect follows the pulse envelope, and that plasma generation occurs by multiphoton ionization [7], following an I^8 power law for oxygen ionization with 800 nm photons. It is immediately evident that the molecular response dominates, especially promoted by the coherent probe interaction.

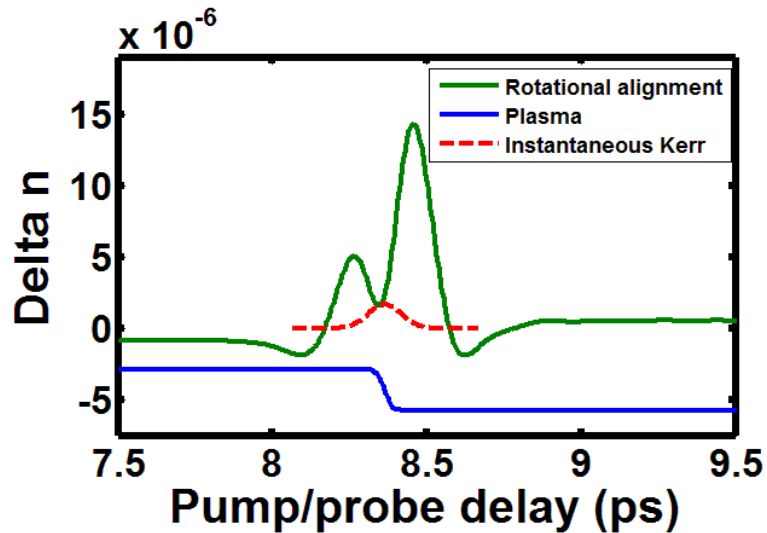


Figure 5.12: Rotational (green), Kerr (dashed red) and plasma (blue) contributions to Δn in air due to a 1.5 mJ pump pulse at $t=0$ and 1.9 mJ probe pulse at delay $\tau = 8.366$ ps for several probe pulse energies.

Figure 5.13 shows a sequence of total (rotation + Kerr + plasma) index shifts Δn for variable pump-probe delay.

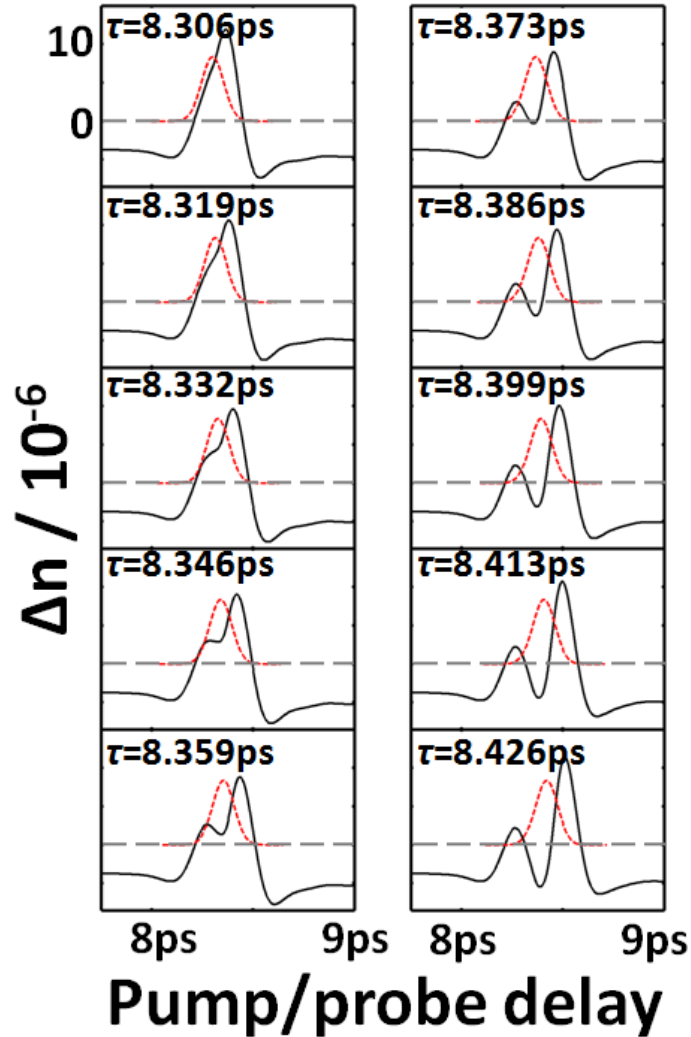


Figure 5.13: Total Δn in air due to a 1.5 mJ pump pulse at $t=0$ and 1.9 mJ probe pulse at a sequence of pump/probe delays (inset). Δn is synthesized from simulations of the contribution from rotational alignment, electronic Kerr effect, and plasma generation.

Note in particular $8.346 \text{ ps} < \tau < 8.373 \text{ ps}$, a span of $\sim 30 \text{ fs}$, where a temporal well with positive curvature exists in Δn such that the well bottom is positive. Such a structure can temporally trap and clean/compress a pulse: the portion of the pulse in the early time (falling) part of the well blue shifts, but then falls back due to normal dispersion of the background air, while the rear portions red shift and move forward. The net result is

soliton-like propagation where self-phase modulation is balanced by the local well structure dispersion. Preliminary 1-D calculations show that the negative GVD afforded by the temporal region of positive curvature of Δn in the simulation in Figure 5.13 is of the correct sign but an order of magnitude larger than what is required to compensate for normal air dispersion of a pulse with bandwidth $\Delta\omega \sim 10^{15} \frac{\text{rad}}{\text{s}}$ —roughly our probe filament bandwidth.

A similar compressive effect has been recently observed in plasma wave generation by ultrashort multi-terawatt pulses [89]; the laser pulse rides in the first bucket of the plasma wave, where the index is affected by both electron density and the relativistic electron mass. The result is that the pulse rides in a refractive index well of positive curvature, with a blue shift temporally leading a red shift.

In addition, such a temporal index structure has been previously proposed for pulse cleanup/compression of weak probe pulses injected into rotational revivals [82, 90], where the injection point was the negative region in the green curve of Fig. 5.12, where the curvature of Δn is positive. Finally, we note that in Fig. 5.13, for $\tau > 8.373$, the central part of the well dips below zero, making the well act as a negative lens. This corresponds well to the abrupt disappearance in Fig. 5.2(b) of the extended filament for delays longer than ~ 8.39 ps: at those longer delays, the negative molecular lens assists the plasma in defocusing the probe.

The correspondence of these heuristic simulations (note that no spatial dependence or propagation is considered), to the fine delay sensitivity in pulse envelope and phase shaping and in the filament extension, is not exact, but still compelling. The slight deviations from predicted and measured filament may be attributed to the low

dimensionality and lack of self-consistency in the simulations and also the difficulty in measuring an exact pump/probe delay during an experiment (error is typically +/- 5 fs).

That being said, the correspondence can be understood as follows. First, for the full range $8.25 \text{ ps} < \tau < 8.38 \text{ ps}$, a substantial portion of the probe pulse time envelope experiences $\Delta n > 0$, and thus those portions are focused transversely and can help to extend the filament, albeit with a potentially spiky time evolution which tends to reduce the peak intensity available to generate filament plasma. Only when the τ is within the special 30 fs- (simulation) to 40 fs- (experiment) wide interval does the probe pulse reside within a Δn well with positive curvature in time. And only in this interval does the pulse intensity rise up sufficiently to maintain the filament multiphoton ionization process. Hence the 10 fs delay sensitivity to both filament extent and peak electron density.

Admittedly, this discussion is speculative and a self-consistent propagation simulation is needed to refine or revise the insight into the physical processes at work. At the time of this writing, such a simulation is taking place using a modified version of the code employed in [14] and has been repeatedly delayed owing to numerical issues with the code.

Another intriguing mechanism for the measured plasma density enhancement, besides molecular lensing and temporal compression, is a possible gain in probe energy from pump-and-probe-aligned molecules at the molecular revival. The motivation for this idea comes from considering the 1D wave equation for the electric field in the slowly varying envelope approximation [14], neglecting dispersion, $\frac{\partial E}{\partial z} = -\frac{4\pi}{c} \frac{\partial P}{\partial T}$, where z is the coordinate in the propagation direction and $T = t - z/c$ is a time coordinate local to the

pulse. Here P is the medium polarization and can be written as

$$P(T) = E(T) \int_{-\infty}^T R(s) |E(s)|^2 ds = \chi E, \text{ where } E \text{ is the electric field, } R \text{ is a response}$$

function, and χ is an effective susceptibility. The propagation equation can be

manipulated to give $\frac{\partial |E|^2}{\partial z} = -\frac{4\pi}{c} \frac{\partial \chi |E|^2}{\partial T}$, whereupon $\int \frac{\partial |E|^2}{\partial z} dz$ is proportional to an energy

loss/gain. So the loss/gain should be non-negligible when the pump probe delay coincides

with a rotational revival, since in those regions $\frac{\partial \chi}{\partial T}$ is non-negligible, as seen from our

prior data and simulations.

To measure probe energy gain/loss in our experiment, we split the probe pulse from the pump pulse 2 meters after filamentation and measured the entire probe beam incident on an optical power meter, as we scanned the pump/probe delay over $8.18 \text{ ps} < \tau < 8.49 \text{ ps}$. In absence of a pump filament, the probe filament measured 1.5 mJ at the power meter, which had a 12 mm input diameter. There was no pump/probe delay over the interval that resulted in an increase in probe energy, but there were several delays near $\tau < 8.43 \text{ ps}$ in which a ~30% energy loss was recorded. Refraction of the probe due to anti-aligned pump molecules did not explain the loss, because when the input aperture of the power meter was closed to 11 mm or 10 mm, the total energy was unchanged. The results of the measurement are shown in Figure 5.14.

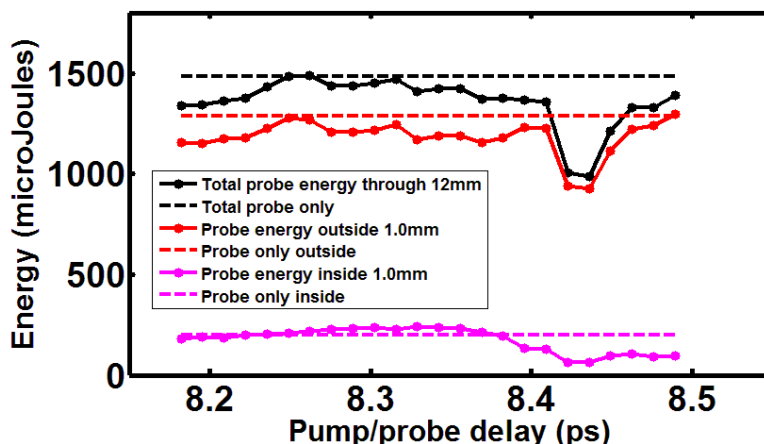


Figure 5.14: Energy in the probe pulse after filamentation as a function of pump/probe delay. Black line—total probe energy, pink line—probe energy inside 1mm core, red line—probe energy outside 1mm core. Dashed lines indicate probe energy in absence of the pump pulse.

The above experiment was also performed with the input aperture of the power meter set to 1.0 mm, in order to measure the fraction of energy inside and outside the core of the filament. The fraction of energy in the core increases slightly over $8.27\text{ps} < \tau < 8.38\text{ps}$, but at the expense of light in the reservoir.

Although we did not measure probe energy gain, the dramatic loss in energy at pump/probe delays $8.4\text{ps} < \tau < 8.5\text{ps}$ lends credence to the idea that gain/loss of probe energy due to coherent molecular rotational excitation may play a role in extension and enhancement of the probe filament plasma density.

5.5 Conclusion

The experiments and discussion in this chapter show that because molecular alignment of N_2 and O_2 in air is the dominant self-focusing nonlinearity in atmospheric filamentation of ultrashort pulses >40 fs in duration, manipulating the nonlinearity using an ultrashort filamenting pump pulse results in enhanced axial plasma density and length

left by a probe filamenting pulse. Our results also strongly suggest that the fast molecular alignment transient, at certain pump/probe delays, causes temporal compression of the probe pulse. The combined processes of spatial and temporal confinement due to the rotational alignment transient result in filament density enhancement and extension.

Filamentation of ultrashort pulses in atmosphere is a remarkable effect with a wide variety of applications. The experiments and analysis presented in this dissertation significantly contribute to our knowledge of the physical processes at work during filamentation, and will hopefully lead to future breakthroughs in the understanding and application of the phenomenon.

References

- [1] R. W. Boyd, *Nonlinear Optics, Second Edition* (Academic Press, 2003).
- [2] P. Lallemand and N. Bloembergen, Self-Focusing of Laser Beams and Stimulated Raman Gain in Liquids, *Physical Review Letters* **15**, 1010 (1965).
- [3] R. R. Alfano and S. L. Shapiro, Observation of Self-phase Modulation and Small-scale Filaments in Crystals and Glasses, *Physical Review Letters* **24**, 592 (1970).
- [4] D. Strickland and G. Mourou, Compression of amplified chirped optical pulses, *Optics Communications* **56**, 219 (1985).
- [5] D. E. Spence, P. N. Kean, and W. Sibbett, 60-fsec pulse generation from a self-mode-locked Ti:sapphire laser, *Optics L* **16**, 42 (1991).
- [6] A. Braun, G. Korn, X. Liu, D. Du, J. Squier, and G. Mourou, Self-channeling of high-peak-power femtosecond laser pulses in air, *Optics Letters* **20**, 73 (1995).
- [7] A. Couairon and A. Mysyrowicz, Femtosecond filamentation in transparent media, *Physics Reports* **441**, 47 (2007).
- [8] G. Fibich and A. L. Gaeta, Critical power for self-focusing in bulk media and in hollow waveguides, *Optics Letters* **25**, 335 (2000).
- [9] Y. Shimoji, A. T. Fay, R. S. F. Chang, and N. Djeu, Direct measurement of the nonlinear refractive index of air, *Journal of the Optical Society of America B* **6**, 1994 (1989).
- [10] S. Varma, Y.-H. Chen, and H. M. Milchberg, Trapping and Destruction of Long-Range High-Intensity Optical Filaments by Molecular Quantum Wakes in Air, *Physical Review Letters* **101**, 205001 (2008).
- [11] J. D. Jackson, *Classical Electrodynamics, Third Edition* (John Wiley & Sons, 2003).
- [12] L. V. Keldysh, Ionization in the field of a strong electromagnetic wave, *Soviet Physics JETP* **20**, 1307 (1965).
- [13] A. Couairon, S. Tzortzakis, L. Berge, M. Franco, B. Prade, and A. Mysyrowicz, Infrared femtosecond light filaments in air: simulations and experiments, *Journal of the Optical Society of America B* **19**, 1117 (2002).
- [14] Y.-H. Chen, S. Varma, T. M. Antonsen, and H. M. Milchberg, Direct Measurement of the Electron Density of Extended Femtosecond Laser Pulse-Induced Filaments, *Physical Review Letters* **105**, 215005 (2010).
- [15] S. Eisenmann, A. Pukhov, and A. Zigler, Fine Structure of a Laser-Plasma Filament in Air, *Physical Review Letters* **98**, 155002 (2007).

- [16] P. Sprangle, J. R. Penano, and B. Hafizi, Propagation of intense short laser pulses in the atmosphere, *Physical Review E* **66**, 046418 (2002).
- [17] A. Ting, D. F. Gordon, E. Briscoe, J. R. Penano, and P. Sprangle, Direct characterization of self-guided femtosecond laser filaments in air, *Applied Optics* **44**, 1474 (2005).
- [18] M. Mlejnek, E. M. Wright, and J. V. Moloney, Dynamic spatial replenishment of femtosecond pulses propagating in air, *Optics Letters* **23**, 382 (1998).
- [19] A. J. Campillo, S. L. Shapiro, and B. R. Suydam, Relationship of self-focusing to spatial instability modes, *Applied Physics Letters* **24**, 178 (1974).
- [20] G. Fibich, S. Eisenmann, B. Ilan, Y. Erlich, M. Fraenkel, Z. Henis, A. Gaeta, and A. Zigler, Self-focusing distance of very high power laser pulses, *Optics Express* **13**, 5897 (2005).
- [21] M. Rodriguez, R. Bourayou, G. Mejean, J. Kasparian, J. Yu, E. Salmon, A. Scholz, B. dStecklum, J. Eisloffel, U. Laux, A. P. Hatzes, R. Sauerbrey, L. Woste, and J.-P. Wolf, Kilometer-range nonlinear propagation of femtosecond laser pulses, *Physical Review E* **69**, 036607 (2004).
- [22] G. Fibich, S. Eisenmann, B. Ilan, and A. Zigler, Control of multiple filamentation in air, *Optics Letters* **29**, 1772 (2004).
- [23] G. Mechain, A. Couairon, M. Franco, B. Prade, and A. Mysyrowicz, Organizing Multiple Femtosecond Filaments in Air, *Physical Review Letters* **93**, 035003 (2004).
- [24] T. Pfeifer, L. Gallmann, M. J. Abel, D. M. Neumark, and S. R. Leone, Circular phase mask for control and stabilization of single optical filaments, *Optics Letters* **31**, 2326 (2006).
- [25] R. Nuter, S. Skupin, and L. Berge, Chirp-induced dynamics of femtosecond filaments in air, *Optics Letters* **30**, 917 (2005).
- [26] G. Mechain, C. D'Amico, Y.-B. Andre, S. Tzortzakis, M. Franco, B. Prade, A. Mysyrowicz, A. Couairon, E. Salmon, and R. Sauerbrey, Range of plasma filaments created in air by a multi-terawatt femtosecond laser, *Optics Communications* **247**, 171 (2005).
- [27] P. Rairoux, H. Schillinger, S. Niedermeier, M. Rodriguez, F. Ronneberger, B. Stein, D. Waite, C. Wedekind, H. Wille, L. Woste, and C. Ziener, Remote sensing of the atmosphere using ultrashort laser pulses, *Applied Physics B* **71**, 573 (2000).
- [28] J. Kasparian, M. Rodriguez, G. Mejean, J. Yu, E. Salmon, H. Wille, R. Bourayou, S. Frey, Y.-B. Andre, A. Mysyrowicz, R. Sauerbrey, J.-P. Wolf, and L. Woste, White-Light Filaments for Atmospheric Analysis, *Science* **301**, 61 (2003).
- [29] H. L. Xu, W. Liu, and S. L. Chin, Remote time-resolved filament-induced breakdown spectroscopy of biological materials, *Optic* **31**, 1540 (2006).

- [30] S. Tzortzakis, B. Prade, M. Franco, and A. Mysyrowicz, Femtosecond laser-guided electric discharge in air, *Physical Review E* **64**, 057401 (2001).
- [31] M. Rodriguez, R. Sauerbrey, H. Wille, L. Woste, T. Fujii, Y.-B. Andre, A. Mysyrowicz, L. Klingbeil, K. Rethmeier, W. Kalkner, J. Kasparian, E. salmon, J. Yu, and J.-P. Wolf, Triggering and guiding megavolt discharges by use of laser-induced ionized filaments, *Optics Letters* **27**, 772 (2002).
- [32] J. Kasparian, Lightning control by lasers, *Nature Photonics* **3**, 120 (2009).
- [33] C. P. Hauri, W. Kornelis, F. W. Helbing, A. Heinrich, A. Couairon, A. Mysyrowicz, J. Biegert, and U. Keller, Generation of intense, carrier-envelope phase-locked few-cycle laser pulses through filamentation, *Applied Physics B* **79**, 673 (2004).
- [34] G. Stibenz, N. Zhavoronkov, and G. Steinmeyer, Self-compression of millijoule pulses to 7.8 fs duration in a white-light filament, *Optics Letters* **31**, 274 (2006).
- [35] H. R. Lange, A. Chiron, J.-F. Ripoche, A. Mysyrowicz, P. Breger, and P. Agostini, High-Order Harmonic Generation and Quasiphase Matching in Xenon Using Self-Guided Femtosecond Pulses, *Physical Review Letters* **81**, 1611 (1998).
- [36] Y. Tamaki, J. Itatani, Y. Nagata, M. Obara, and K. Midorikawa, Highly Efficient, Phase-Matched High-Harmonic Generation by a Self-Guided Laser Beam, *Physical Review Letters* **82**, 1422 (1999).
- [37] Y. C. Shen, T. Lo, P. F. Taday, B. E. Cole, W. R. Tribe, and M. C. Kemp, Detection and identification of explosives using terahertz pulsed spectroscopic imaging, *Applied Physics Letters* **86**, 241116 (2005).
- [38] R. H. Jacobsen, D. M. Mittleman, and M. C. Nuss, Chemical recognition of gases and gas mixtures with terahertz waves, *Optics Letters* **21**, 2011 (1996).
- [39] K. Y. Kim, J. H. Glowina, A. J. Taylor, and G. Rodriguez, Terahertz emission from ultrafast ionizing air in symmetry-broken laser fields, *Optics Express* **15**, 4577 (2007).
- [40] K. Y. Kim, A. J. Taylor, J. H. Glowina, and G. Rodriguez, Coherent control of terahertz supercontinuum generation in ultrafast laser-gas interactions, *Nature Photonics* **2**, 605 (2008).
- [41] S. Tzortzakis, G. Mechain, G. Patalano, Y.-B. Andre, B. Prade, M. Franco, A. Mysyrowicz, J.-M. Munier, M. gheudin, G. Beaudin, and P. Encrenaz, Coherent subterahertz radiation from femtosecond infrared filaments in air, *Optics Letters* **27**, 1944 (2002).
- [42] C. D'Amico, A. Houard, M. Franco, B. Prade, A. Mysyrowicz, A. Couairon, and V. T. Tikhonchuk, Conical Forward THz Emission from Femtosecond-Laser_Beam Filamentation in Air, *Physical Review Letters* **98**, 235002 (2007).

- [43] A. Houard, Y. Liu, A. Mysyrowicz, and B. Leriche, Calorimetric detection of the conical terahertz radiation from femtosecond laser filaments in air, *Applied Physics Letters* **91**, 241105 (2007).
- [44] K. M. Davis, K. Miura, N. Sugimoto, and K. Hirao, Writing waveguides in glass with a femtosecond laser, *Optics Letters* **21**, 1729 (1996).
- [45] K. Miura, J. Qiu, H. Inouye, and T. Mitsuyu, Photowritten optical waveguides in various glasses with ultrashort pulse laser, *Applied Physics Letters* **71**, 3329 (1997).
- [46] C. B. Schaffer, A. Brodeur, J. F. Garcia, and E. Mazur, Micromachining bulk glass by use of femtosecond laser pulses with nanojoule energy, *Optics Letters* **26**, 93 (2001).
- [47] N. F. Borrelli, C. Smith, D. C. Allan, and T. P. S. III, Densification of fused silica under 193-nm excitation, *Journal of the Optical Society of America B* **14**, 1606 (1997).
- [48] A. Vogel, S. Busch, and U. Parlitz, Shock wave emission and cavitation bubble generation by picosecond and nanosecond optical breakdown in water, *Journal of the Acoustical Society of America* **100**, 148 (1996).
- [49] M. K. Hornstein, T. G. Jones, and A. C. Ting, Optical Bandwidth and Focusing Dynamics Effects on an Underwater Laser Acoustic Source, in *OSA/CLEO/IQEC* (2009).
- [50] Z. W. Wilkes, S. Varma, Y.-H. Chen, H. M. Milchberg, T. G. Jones, and A. Ting, Direct measurements of the nonlinear index of refraction of water at 815 and 407 nm using single-shot supercontinuum spectral interferometry, *Applied Physics Letters* **94**, 211102 (2009).
- [51] T. Juhasz, G. A. Kastis, C. Suarez, Z. Bor, and W. E. Bron, Time-resolved observations of shock waves and cavitation bubbles generated by femtosecond laser pulses in corneal tissue and water, *Lasers in Surgery and Medicine* **19**, 23 (1998).
- [52] A. Vogel and V. Venugopalan, Mechanisms of Pulsed Laser Ablation of Biological Tissues, *Chemical Review* **103**, 577 (2003).
- [53] V. G. Dmitriev, G. G. Gurzadyan, and D. N. Nikogosyan, *Handbook of Nonlinear Optical Crystals* (Springer, 1997).
- [54] J.-C. Diels and W. Rudolph, *Ultrashort Laser Pulse Phenomena: Fundamentals, Techniques, and Applications on a Femtosecond Time Scale* (Academic Press, 2006).
- [55] D. J. Cane and R. Trebino, Single-shot measurement of the intensity and phase of an arbitrary ultrashort pulse by using frequency-resolved optical gating, *Optics Letters* **18**, 823 (1993).
- [56] P. O'Shea, M. Kimmel, X. Gu, and R. Trebino, Highly simplified device for ultrashort-pulse measurement, *Optics Letters* **26**, 932 (2001).
- [57] C. Iaconis and I. A. Walmsley, Spectral phase interferometry for direct electric-field reconstruction of ultrashort optical pulses, *Optics Letters* **23**, 792 (1998).

- [58] M. Takeda, H. Ina, and S. Kobayashi, Fourier-transform method of fringe-pattern analysis for computer-based topography and interferometry, *Journal of the Optical Society of America* **72**, 156 (1982).
- [59] T. M. Shuman, M. E. Anderson, J. Bromage, C. Iaconis, L. Waxer, and I. A. Walmsley, Real-time SPIDER: ultrashort pulse characterization at 20Hz, *Optics Express* **5**, 134 (1999).
- [60] J. H. Osthner, D. A. Romanov, and R. J. Levis, Rovibrational Wave-Packet Dispersion during Femtosecond Laser Filamentation in Air, *Physical Review Letters* **103**, 075005 (2009).
- [61] J. P. Heritage, T. K. Gustafson, and C. H. Lin, Observation of Coherent Transient Birefringence in CS₂ Vapor, *Physical Review Letters* **34**, 1299 (1975).
- [62] C. H. Lin, J. P. Heritage, T. K. Gustafson, R. Y. Chiao, and J. P. McTague, Birefringence arising from the reorientation of the polarizability anisotropy of molecules in collisionless gases, *Physical Review A* **13**, 813 (1976).
- [63] P. M. Felker, Rotational Coherence Spectroscopy: Studies of the Geometries of Large Gas-Phase Species by Picosecond Time-Domain Methods, *Journal of Physical Chemistry* **96**, 7844 (1992).
- [64] G. V. Hartland, L. L. Connell, and P. M. Felker, Theory of rotational coherence spectroscopy as implemented by picosecond fluorescence depletion schemes, *Journal of Chemical Physics* **94**, 7649 (1991).
- [65] J.-F. Ripoche, G. Grillon, B. Prade, M. Franco, E. Nibbering, R. Lange, and A. Mysyrowicz, Determination of the time dependence of n_2 in air, *Optics Communications* **135**, 310 (1997).
- [66] E. Nibbering, G. Grillon, M. A. Franco, B. S. Prade, and A. Mysyrowicz, Determination of the inertial contribution to the nonlinear refractive index of air, N₂, and O₂ by use of unfocused high-intensity femtosecond laser pulses, *Journal of the Optical Society of America B* **14**, 650 (1997).
- [67] Y.-H. Chen, S. Varma, A. York, and H. M. Milchberg, Single-shot, space- and time-resolved measurement of rotational wavepacket revivals in H₂, D₂, N₂, O₂, and N₂O, *Optics Express* **15**, 11341 (2007).
- [68] D. Halliday, R. Resnick, and J. Walker, *Fundamentals of Physics* (John Wiley & Sons, Inc., 1997).
- [69] F. Rosca-Pruna and M. J. J. Vrakking, Experimental Observation of Revival Structures in Picosecond Laser-Induced Alignment of I₂, *Physical Review Letters* **87**, 153902 (2001).
- [70] P. W. Dooley, I. V. Litvinyuk, K. F. Lee, D. M. Rayner, M. Spanner, D. M. Villeneuve, and P. B. Corkum, Direct imaging of rotational wave-packet dynamics of diatomic molecules, *Physical Review A* **68**, 023406 (2003).

- [71] K. Y. Kim, I. Alexeev, and H. M. Milchberg, Single-shot supercontinuum spectral interferometry, *Applied Physics Letters* **81**, 4124 (2002).
- [72] F. Reynaud, F. Salin, and A. Barthelemy, Measurement of phase shifts introduced by nonlinear optical phenomena on subpicosecond pulses, *Optics Letters* **14**, 275 (1989).
- [73] E. Tokunaga, A. Terasaki, and T. Kobayashi, Frequency-domain interferometer for femtosecond time-resolved phase spectroscopy, *Optics Letters* **17**, 1131 (1992).
- [74] E. Tokunaga, A. Terasaki, and T. Kobayashi, Induced phase modulation of chirped continuum pulses studied with a femtosecond frequency-domain interferometer, *Optics Letters* **18**, 370 (1993).
- [75] S. P. LeBlanc, E. W. Gaul, N. H. Matlis, A. Rundquist, and M. C. Downer, Single-shot measurement of temporal phase shifts by frequency-domain holography, *Optics Letters* **25**, 764 (2000).
- [76] K. Y. Kim, I. Alexeev, and H. M. Milchberg, Single-shot measurement of laser-induced double step ionization of helium, *Optics Express* **10**, 1563 (2002).
- [77] K. Y. Kim, I. Alexeev, V. Kumarappan, E. Parra, T. Antonsen, T. Taguchi, A. Gupta, and H. M. Milchberg, Gases of exploding laser-heated cluster nanoplasmas as a nonlinear optical medium, *Physics of Plasmas* **11**, 2882 (2004).
- [78] Y.-H. Chen, S. Varma, I. Alexeev, and H. M. Milchberg, Measurement of transient nonlinear refractive index in gases using xenon supercontinuum single-shot spectral interferometry, *Optics Express* **15**, 7458 (2007).
- [79] I. V. Litvinyuk, K. F. Lee, P. W. Dooley, D. M. Rayner, D. M. Villeneuve, and P. B. Corkum, Alignment-Dependent Strong Field Ionization of Molecules, *Physical Review Letters* **90**, 233003 (2003).
- [80] D. M. Pennington, M. A. Henesian, and R. W. Hellwarth, Nonlinear index of air at 1.053 μ m, *Physical Review A* **39**, 3003 (1989).
- [81] W. Liu and S. L. Chin, Direct measurement of the critical power of femtosecond Ti:sapphire laser pulse in air, *Optics Express* **13**, 5750 (2005).
- [82] R. A. Bartels, T. C. Weinacht, N. Wagner, M. Baertschy, C. H. Greene, M. M. Murnane, and H. C. Kapteyn, Phase Modulation of Ultrashort Light Pulses using Molecular Rotational Wave Packets, *Physical Review Letters* **88**, 013903 (2002).
- [83] P. Mora and J. Thomas M. Antonsen, Kinetic modeling of intense, short laser pulses propagating in tenuous plasmas, *Physics of Plasmas* **4**, 217 (1997).
- [84] W. Liu, J.-F. Gravel, F. Theberge, A. Becker, and S. L. Chin, Background reservoir: its crucial role for long-distance propagation of femtosecond laser pulses in air, *Applied Physics B* **80**, 857 (2005).

- [85] F. Calegari, C. Vozzi, S. Gasilov, E. Benedetti, G. Sansone, M. Nisoli, S. D. Silvestri, and S. Stagira, Rotational Raman Effects in the Wake of Optical Filamentation, *Physical Review Letters* **100**, 123006 (2008).
- [86] G. P. Agrawal, *Fiber-optic Communication Systems, Third Edition* (John Wiley & Sons, 2002).
- [87] C. G. D. III, J. Lynch, and H. M. Milchberg, Development of a plasma waveguide for high-intensity laser pulses, *Physical Review E* **51**, 2368 (1995).
- [88] J. Paye, The Chronocyclic Representation of Ultrashort Light Pulses, *IEEE Journal of Quantum Electronics* **28**, 2262 (1992).
- [89] J. Schreiber, C. Bellei, S. P. D. Mangles, C. Kamperidis, S. Kneip, S. R. Nagel, C. A. J. Palmer, P. P. Rajeev, M. J. V. Streeter, and Z. Najmudin, Complete Temporal Characterization of Asymmetric Pulse Compression in a Laser Wakefield, *Physical Review Letters* **105**, 235003 (2010).
- [90] V. Kalosha, M. Spanner, J. Herrmann, and M. Ivanov, Generation of Single Dispersion Precompensated 1-fs Pulses by Shaped-Pulse Optimized High-order Stimulated Raman Scattering, *Physical Review Letters* **88**, 103901 (2002).